

Calibration of Infrared Photons in Cryogenic Germanium Detectors

by

Muad Mohammad Ghaith

A thesis submitted to the Graduate Program in
Physics, Engineering Physics & Astronomy
in conformity with the requirements for the
Degree of Master of Science

Queen's University

Kingston, Ontario, Canada

April, 2017

Copyright © Muad Mohammad Ghaith, 2017

To my parents, Wajd, Haya, Rashid and Serene.

Abstract

A significant evidence from galaxies and astrophysical observations, suggests that $\sim 85\%$ of the matter in our Universe is invisible matter. The observations of the so-called “dark matter” suggest that it consists of non-relativistic, non-baryonic particles, which seldom interact with baryonic matter, or with each other. Many experiments are searching for dark matter, each of which is based on a particular dark matter candidate. Weakly Interacting Massive Particles (WIMPs) are one of the well-motivated candidates for dark matter. So far, no answers were provided by the Standard Model of particle physics to the dark matter puzzle.

The Super Cryogenic Dark Matter Search experiment (SuperCDMS) is considered one of the pioneer experiments in the direct search for WIMPs. It is based primarily on deploying germanium and silicon detectors at cryogenic temperatures to search for direct WIMP-nucleus elastic scattering interaction through which lattice vibrations are generated and sensed in one of the coldest detectors ever built.

The new phase of SuperCDMS experiment at SNOLAB is aiming to be sensitive to the lower WIMP mass scale. Therefore, a lower background and detector threshold energy is a necessity, and the detectors need to be calibrated and tested for the new proposed sensitivity. The tests include high bias voltages, which are required to increase the gain in signal-to-noise ratio and to allow for the detection of low energy events using the phonon signal. However, the upper limit and polarity for the bias voltage need further studies in order to understand the variation of the detector’s response to high voltage. Therefore, we performed the breakdown measurement (chapter 4) at Queen’s Test Facility.

Moreover, detectors have to be calibrated before being utilized in measuring low energy interactions, and that is what lead to the use of infrared photons. Once we can calibrate and understand the behavior of infrared photons in germanium detectors, they can be utilized in calibrating germanium detectors at the lower energy scale. Therefore, we performed the infrared calibration measurement which represents the bulk of the work in my thesis.

Acknowledgements

I think I would need a few pages to thank all the people who supported me for the last few years, and without the help of each and every one, reaching this end was not possible. So, for every person I had the honor to meet with – Thank You.

At the top of my list comes Wolfgang Rau, my supervisor, a real person that any graduate student would love to work with, and to learn proper scientific procedures from, distinguished by his broad knowledge and good judgment. Thank you for your patience, and for the time you spent explaining real interesting science to me. I am grateful for the invaluable support you gave to me through each step of my graduate studies.

At Queen's University level, I would like to thank all my teachers, and specially in SNO group. Kedar Page, thank you for the introduction you provided during the first few months. Charles (Chuck) Hearn, thank you for all the parts you made to our cryostat, and for the wonderful time we spent at the golf course. Steve Gillen, thank you for the help and guidance with my LEDs. Xiaohe Zhang, thank you for all the time we spent together working on the cryostat, thank you for all the time you spent working on the connection boxes, and soldering tens of connection points. Ryan Underwood, thank you for being a good friend and a great travel companion, and Nicholas Andrews, Hans-Peter Loock for providing us with the optical fiber cable.

At the SuperCDMS collaboration level, thanks to Matt Cherry for fixing the broken wire-bonds in our detector. Matt Fritts for the fruitful time we had at UMN. Anthony Villano, Amy Roberts, Bruno Serfass thank you all for the help in installing MIDAS and for the endless effort

to make it work at QTF. Tarek Saab, thank you for the discussion we had about the high voltage measurement. Lauren Hsu, thank you for the debates we had about the infrared LEDs. Sten Hansen, thank you for fixing our DCRC board. Philippe Di Stefano, thank you for being a great mentor during the particle physics course, and thanks for the time we had together at Soudan. Jeter Hall, Ritoban Thakur thanks for the time we spent together at Soudan.

Finally, this is where the words are not enough, but I have to say thank you. Thanks to my wife, my Soulmate, Serene. Thank you for being by my side on each and every step of the way, and yet, you still sane. It's not an easy task, taking care of our "lovely" three kids and pursuing you graduate studies at the same time. You have done all this perfectly. Thanks to my kids, Wajd for spilling coffee over my notes, but avoiding my phone. Haya, for making my notebook your favorite drawing papers. And Rashid, it's always been a pleasure to change your diapers. Last but not least, thanks to my brothers and sisters and my parents, thank you for teaching me, and for putting your trust in me. My dearest parents, your contentment is all that matters.

Table of Contents

Table of Contents

Abstract.....	i
Acknowledgements	iii
Table of Contents	v
List of Figures	viii
List of Tables.....	xiii
Chapter 1 Introduction	1
1.1 Dark Matter	1
1.2 Evidence of Existence	3
1.2.1 Rotational curve of spiral galaxies.....	3
1.2.2 Gravitational lensing	5
1.2.3 The Bullet Cluster	7
1.3 Candidates for Dark Matter	10
1.3.1 Weakly Interacting Massive Particles (WIMPs).....	10
1.3.2 Axions	12
1.4 The search for WIMPs	15
1.4.1 Direct detection.....	16
1.4.2 Indirect detection	18
Chapter 2 SuperCDMS Experiment	19
2.1 Detectors between the past and the future.....	20
2.2 Queen’s Test Facility	21
2.3 QTF Dilution Refrigerator	22
2.4 Cold Hardware and Readout Electronics.....	26
2.4.1 SuperCDMS Detectors	28

2.4.2 SQUET Cards.....	30
2.4.3 Phonon readout circuit.....	31
2.5 SuperCDMS results	36
Chapter 3 T_c Measurement at QTF	38
3.1 Experimental setup	39
3.2 Experimental method	41
3.3 Comparison of Results	45
3.4 Conclusion	47
Chapter 4 Detector Breakdown-voltage Measurement.....	48
4.1 Experimental setup	49
4.2 HV Technique and results.....	52
4.3 Conclusion	58
Chapter 5 IR Photon Calibration Measurement.....	59
5.1 Charge propagation	59
5.2 Experimental setup.....	62
5.2.1 Multimode fiber optic cable.....	62
5.2.2 Light Emitting Diodes (LEDs).....	65
5.2.3 G16K – hiZIP Detector configuration.....	68
5.2.4 Detector’s electric field configuration.....	70
5.2.4 Calibration source	71
5.3 Experimental Techniques	73
5.3.1 Stability of charge channels.....	75
5.3.2 Relative calibration of phonon channels.....	75
5.4 Processing method and data quality cuts	78
5.4.1 Optimal Filter.....	78
5.4.2 The charge χ^2 cut	80
5.4.2 Phonon pile-up cut	83
5.4.3 Phonon duplicates cut.....	84
5.4.4 Phonon pre-pulse cut.....	85
5.5 Data analysis and results.....	85

5.5.1 1550 n m LED in iZIP e-field configuration	88
5.5.2 1550 n m LED in flat e-field configuration	92
5.5.3 890 n m LED in iZIP e-field configuration	94
5.5.4 890 n m LED in flat e-field configuration	96
5.5.5 940 n m detector's internal LED	98
5.6 Summary of findings	101
Chapter 6 Conclusion and outlook	107
Bibliography	109
Appendices	115
Appendix A	115
A.1 Calculations of Neganov-Luke Amplification for 1550 nm, in straight field	115

List of Figures

Figure 1.1: The rotational curve versus the distance from the center of the galaxy. The proposed dark matter effect is depicted by the dashed line. Image source [5].5

Figure 1.2: Gravitations lensing caused by bending of light while approaching a massive region. Image courtesy (NASA Archive).6

Figure 1.3: Evidence of dark matter in galaxy clusters. The hot gas (in red) and dark matter (in blue). *Panel (a)*: Image using the visible wavelength (optical). *Panel (b)*: Blue blobs show the location of the mass (dark matter). *Panel (c)*: X-ray telescope image show the plasma distribution and shock as a result of a collision. *Panel(d)*: Hot gas and gravity are at different locations, which show the present observable state of the two clusters. Image courtesy: Chandra X-ray Observatory.9

Figure 1.4: *Left panel*: Feynman diagram of axion decay into photons. *Right panel*: conversion into a vacuum. Image source [20].13

Figure 1.5: Exclusion limits for axion mass, as reported from axion search experiments with respect to both upper and lower limits. Image source [17].14

Figure 1.6: Dark matter detection methods, based on the proposed interaction between dark matter and particles from the Standard Model.15

Figure 1.7: A classification of dark matter search experiments based on the type of measured signal.17

Figure 2.1: A cross-section view, showing the different stages of QTF dilution refrigerator. There exists a radiation can at each of 70 K, 4 K and still plate in addition to a vacuum Dewar at room temperature. Image source [35].22

Figure 2.2: The phase separation for the mixture. The x-axis represents the ration of ^3He atoms to the total number of atoms, and the dashed region represents a forbidden region for the mixxture to exist. Image source [37].24

Figure 2.3: The mixing chamber (not to scale) sitting on the base plate. Where the process of phase separation is taking place and ^3He diffuses from concentrated to diluted phase inside the chamber. At temperature close to 0 K, the concentration of ^3He in diluted phase is $\sim 6.6\%$. 25

Figure 2.4: A schematic diagram of the cold hardware from the SuperCDMS experiment at SUL. showing the different thermal stages of the tower supported by carbon tubes to give the necessary thermal isolation and to support the tower structure. Each stack in the SuperCDMS experiment has three iZIP detectors. Image source [40].27

Figure 2.5: A 620 g germanium iZIP, Mercedes-like design detector. Image source [43, 44].	29
Figure 2.6: SuperCDMS SQUET card.	31
Figure 2.7: A schematic drawing (not to scale) for the Superconducting Quasiparticle-trap-assisted Electrothermal-feedback Transition-edge phonon sensor (QET), and the mechanism through which phonons are collected from the crystal. Aluminum fins and TES cover a large surface area on both detector surfaces. In addition, they have low heat capacity; hence, thermalization with the detector occurs very quickly.	32
Figure 2.8: The transition from superconducting to normal state in TES. Image source [50].	34
Figure 2.9: A schematic diagram for the phonon readout circuit. Image source [51].	35
Figure 2.10: Latest results from CDMSlite run II (in red) as reported during the SuperCDMS collaboration meeting in Aug 2016.	37
Figure 3.1: Eight Tc samples glued to a 1 cm thick detector housing (ZBT1-19).	39
Figure 3.2: <i>Left panel:</i> The pi-filter connected between the E-box of the cryostat and the DCRC board. <i>Right panel:</i> The Insertion loss - curve corresponds to the utilized pi-filter. Pi filter insertion plot source [57].	40
Figure 3.3: Screen shots for the detector readout, showing one of the phonon channels changing its state from superconducting to normal. (a) The test signal as it appears on the control readout while the sample is in superconducting state. (b) The amplitude starts to decrease at the beginning of transition. (c) at transition, when the superconducting slope almost disappeared. (d) while the sample is normal, the amplitude becomes too small and almost stops decreasing. Note the change of the scale on y-axis.	41
Figure 3.4: Resistance versus Temperature graph during a 4-wire measurement.	44
Figure 3.5: Comparison between the results from SLAC to that from QTF. <i>Red line</i> represents the data from SLAC with respect to run 61. <i>Black line</i> represents different runs at QTF. Ideally, the slope of the black line should be 1 and y-intercept at 0. <i>Blue line</i> represents the data from run 63 (4-wire measurement) relative to run 61.	45
Figure 4.1: External modification box for the charge channels, (the box was made by Xiaohe Zhang).	49
Figure 4.2: Circuit diagram of the charge readout channel, showing the modifications required for high voltage test (in blue). The bypass for the bias resistor was done for different purpose in older run and has nothing to do with the high voltage measurement. This would have been an issue if something went wrong during this test.	51
Figure 4.3: Energy of phonon channel D calibrated to ^{241}Am source at different positive bias voltages. The error in the above measured quantities is ± 5 keV.	52

Figure 4.4: Total phonon energy versus bias voltage at positive (red) and negative (blue) polarities. Error bars are too small to be seen.....	55
Figure 4.5: Leakage current during the measurement is extremely small, and could not have an effect on the applied voltage. Vertical error bars represent the standard error for the measurement.	55
Figure 4.6: The noise power spectral density in phonon sensor B at negative bias voltages.	56
Figure 4.7: The noise power spectral density in phonon sensor B at positive bias voltages.....	57
Figure 4.8: The noise in the phonon signal as a function of biasvoltage in positve and negative polarities.	58
Figure 5.1: Oblique electron propagation in germanium crystal at the milli-Kelvin temperature, and low electric field. Image from [65].	60
Figure 5.2: Two-dimensional pattern of (a) electrons and (b) holes drifting to a non-illuminated face of the germanium sample. At low electric field (less than 5V/cm), the electrons propagate into four regions corresponding to four minima in the conduction band. Image from [66].....	61
Figure 5.3: The installation of fiber cable at QTF.	64
Figure 5.4: Energy band gap at room temperature for germanium. Image source [68].	65
Figure 5.5: <i>Left panel:</i> Vacuum feedthrough cover to hold the external IR LEDs. <i>Right panel:</i> The cover while mounted at the top of a black rubber to block the ambient visible light radiation from reaching the fiber cable. The LEDs can be swapped mechanically by changing screw location of the top cover.....	67
Figure 5.6: The absorption coefficient dependence on both, temperature and photon's wavelength. Image from [71].	68
Figure 5.7: G16K – wiring diagram. The blue circle represents the position of the ^{241}Am source and the green circle represents the position of the fiber cable relative to the detector surface.....	69
Figure 5.8: The e-field configuration for the iZIP detector. The grounded electrodes are the phonon channels, while the biased are the charge. Image from [43].	70
Figure 5.9: The use of Am-241 source to calibrate the energy scale of the 1550 nm LED at zero bias voltage. The x-axis represents the energy sum of the calibrated phonon channels.	72
Figure 5.10: LED events can be identified (in green) after tuning the LED settings. In this plot, the 1550 nm LED was turned on after ~1k events. The events in red are the 60 keV line from ^{241}Am source.	73
Figure 5.11: A plot showing the phonon partitioning parameter in the x-y plane as defined in equations 5.10 and 5.11. <i>Left panel:</i> The 1550 nm LED events are highlighted in green, and they	

appear to be focused on phonon sensors (B) and (D). <i>Right panel:</i> The 890 nm LED events are highlighted in green.....	74
Figure 5.12: The plot shows the charge calibrated to a gamma source for the electrodes Q_2 and Q_p . Data was taken for ~ 7 min and bias voltage of 24 V. Electrons were collected at side 1 (Q_p) while holes were collected at side 2 (Q_2). No charge degradation was noticed for the gamma events, indicating a stable charge collection efficiency over the time.	75
Figure 5.13: The late integral quantities of phonon channel C vs. phonon channel A.....	76
Figure 5.14: <i>Left panel:</i> Phonon pulses before applying relative calibration to the phonon channels. <i>Right panel:</i> Phonon pulses after evaluating the late integral quantities, and using the calibration factors to plot the pulses.....	77
Figure 5.15: The optimal filter charge χ_2 for Q_2 versus Q_2	81
Figure 5.16: <i>Top panel:</i> An example for a good charge pulse, which survived after applying the charge χ_2 cut. <i>Bottom panel:</i> This plot shows an example for one of the excluded events by the charge χ_2 cut.	82
Figure 5.17: <i>Top panel:</i> This plot shows an event passing the pile-up cut, because the threshold was crossed only one time (“maxdifdifav” represents a counter for the number of times the threshold value is crossed). <i>Bottom panel:</i> This plot shows a rejected pile-up event, where the threshold value was crossed twice.	84
Figure 5.18: <i>Left panel:</i> Q_2 charge channel calibrated to gamma source vs. the sum of the calibrated phonon channels. <i>Right panel:</i> Q_p charge channel vs. the sum of calibrated phonon channels.	89
Figure 5.19: <i>Left panel:</i> Charge channel Q_2 calibrated to a gamma source vs. the sum of calibrated phonon channels. <i>Right panel:</i> Charge channel Q_p calibrated to a gamma source vs. the sum of calibrated phonon channels.	92
Figure 5.20: <i>Left panel:</i> Charge channel Q_2 calibrated to a gamma source vs. the sum of calibrated phonon channels. <i>Right panel:</i> Charge channel Q_p calibrated to a gamma source vs. the sum of calibrated phonon channels.	94
Figure 5.21: <i>Left panel:</i> Charge channel Q_2 calibrated to a gamma source vs. the sum of calibrated phonon channels. <i>Right panel:</i> Charge channel Q_p calibrated to a gamma source vs. the sum of calibrated phonon channels.	96
Figure 5.22: The increase in charge signal indicates the quick saturation of Q_{inner} and Q_{outer} on side 1.	97

Figure 5.23: Calibrated phonon pulses, from the detector’s internal LED. The amplification in the phonon channels occurs as the voltage increase, which confirms the formation of Neganov-Luke phonons.	98
Figure 5.24: Charge pulses for different events. Unusual behavior for the charge channels in figure (a) while operating the detector’s internal LED, compared to regular pulse shape from the gamma source in figure (b) and an external LED in figure (c).	99
Figure 5.25: The events circled in red are the 1550 nm LED events. A clear charge degradation accompanied with a drop in the phonon signal was recorded at different voltages and polarities. While the ²⁴¹ Am events, zoomed area and circled in black, show homogenous distribution in time and no evidence of charge/ phonon degradation.	101
Figure 5.26: The detector is biased at different voltages and different polarities as indicated in the plot. Each colored slice contains a stable gamma event line at 60 keV and a dropping signal from the IR photons. The initial state of the detector can be retrieved by flipping the polarity, which confirms that the drop in the charge/ phonon signal can be referred to the detector rather than the LED itself.	102
Figure 5.27: The energy of the phonon signal at different bias voltages for the 1550 nm (890 nm) LED, in iZIP electric field configuration. The green (yellow) line is the expected phonon signal for the IR photons based on measured charge, while the blue (purple) line is the measured phonon signal. Error bars are too small to be seen.	103
Figure 5.28: Charge collection efficiency variation with bias voltage. The measured (in black) and expected (in red) charge signal, in iZIP electric field configuration for the 1550 nm LED at different voltages. The expected charge signal in this case is based on the measured phonon signal from IR events.	104

List of Tables

Table 1: The data corresponds to SLAC T_c samples from run 65 at QTF.....	43
Table 2: The data corresponds to TAMU T_c samples from run 65 at QTF.	43
Table 3: The table includes the critical temperature measurements done at QTF and SLAC for detector housing (ZB1T-19).....	46
Table 4: The measured and expected values for the charge and total phonon energy using a calibration gamma source ^{241}Am . In the table, each of the measured value represents either the measured charge signal (Q) or the total phonon energy (Psum) based surface and bulk events. The error in the measured values is based on the deviation from the measured average value.	86
Table 5: The measured and expected energy values for the 1550 nm LED in the iZIP electric field configuration. In the 7 th column, B stands for bulk events and S for surface events. The ± 6 V data set is not available.....	90
Table 6: The measured and expected energy values for the 1550 nm LED in a straight electric field configuration.	93
Table 7: The measured and the expected values for the 890 nm LED in the iZIP electric field configuration. In the 7 th column, B stands for bulk events, and S stands for surface events.	95



Chapter 1

Introduction

1.1 Dark Matter

For hundreds of years, scientists were looking up to the sky believing that bright objects are all that made up the Universe. Nowadays, scientists believe that not only illuminated objects are important, but also what hides in the dark as well. Most of the cosmological and astrophysical observations suggest that the majority of the Universe is an invisible matter “Dark Matter.” The proof of the dark matter existence can be concluded from the conceivable interactions between dark and baryonic matter. It is believed that the mysterious dark matter is what binds the stars and galaxies together. More detailed expectations suggest that dark matter works as a skeleton, and the luminous matter is supported by this invisible structure.

One of the well-motivated candidates for dark matter is the Weakly Interacting Massive Particle (WIMP). Other particles such as; Axions and Massive Astrophysical Compact Halo (MACHOs) are also considered to be good dark matter candidates. Another constituent of the Universe found to be the dark energy, which might be responsible for driving galaxies further and further apart. Combined, dark matter and dark energy, make up ~96% of the Universe [1].

Uncovering their secret is a major field of research. If uncovered, then the ultimate fate of the Universe might be revealed.

In the year 1933, the first evidence for Dark Matter existence was found by Fritz Zwicky [2]. His major discovery was the evidence of matter interaction via gravitation, rather than electromagnetic waves. Hence, this matter does not emit light, and that is where the name “dark” came from. The research done by Zwicky using the virial theorem on the Coma cluster, was based on measuring the radial velocities of many galaxies in the Coma cluster, and he was able to show that the velocity dispersion was far too high to be accounted for by the luminous matter in the cluster. In other words, the radial velocity of the galaxies within a cluster is much faster than what the luminous matter can attract. This effect is clearly exposed in galaxies where dark matter is dominant, such as dwarf galaxies [3].

The search for dark matter halted for few decades, before Vera Rubin and Kent Ford at the late 1960s, could present a sound proof, with a much higher accuracy, for the existence of dark matter. Afterward; during the 1980s; different astrophysical observations such as gravitational lensing and cosmic microwave background have also backed up the presence of dark matter.

This chapter aims to cover the facts led to conclude the existence of dark matter and to introduce some of the best dark matter candidates, besides dark matter detection methodologies.

1.2 Evidence of Existence

Dark matter is unlike anything we have encountered on Earth. Billions of these strange particles pass through everything they encounter each second. It is believed that they are so massive in weight, that they have the power to influence the galaxies, how galaxies form, and even how fast they spin. On the other hand, it is also believed that they interact very weakly with regular matter. Dark matter's ghostly presence seems to be everywhere in the Universe, where physicists and astronomers have not directly proven its existence, and although there are many dark matter candidates, however, no definite answer, yet. Since dark matter does not emit, absorb or interact with light, the evidence of its existence can only be concluded indirectly from several observations. In this section, I will be listing some of these observations.

1.2.1 Rotational curve of spiral galaxies

The rotational curve is basically plotting the orbital speed versus the distance from the galactic center. In general, the speed of orbiting objects depends on the gravitational force that holds the orbiting object, and how far the object is from the center (assuming circular motion). Now, if the mass of the system is concentrated at the center of the system, then the speed of orbiting object should be decreasing as the radius increases. This can be represented by:

$$v_{rot}^2 = \frac{GM(R)}{R} \quad (1.1)$$

where the mass is given by $M(R) = \int_0^R 4\pi r^2 \rho(r) dr$. A good example of this would be the speed of planets in our solar system, where further planets from the Sun experience less gravitational force, hence, their orbital speed decreases: $v_{rot}^2 \propto \frac{1}{R}$.

On the other hand, discussing orbital speed in galaxies does not follow the same rationale. So, by examining various galaxies and measuring their orbital speed by Doppler shift measurement, it was noticed that the luminous matter is concentrated more at the center of the galaxy [4]. Moreover, if we consider only the luminous matter in a galaxy, we would expect to have a rotation curve similar to that of the solar system. But, that is not what was actually measured. By measuring the speed of stars using Doppler shift, what was found was that the speed of these orbiting galaxies remains almost invariant, as they get further away from the center, as shown in figure 1.1[5]. For this to be possible, and to have a constant speed even if the distance increases, mass should be present over the entire orbital system, not just at the center of the galaxy. But, recalling that the brightest part of the galaxy is at the center, may lead to the conclusion of the existence of an additional non-luminous matter that has a gravitational effect, and does not interact via electromagnetic force.

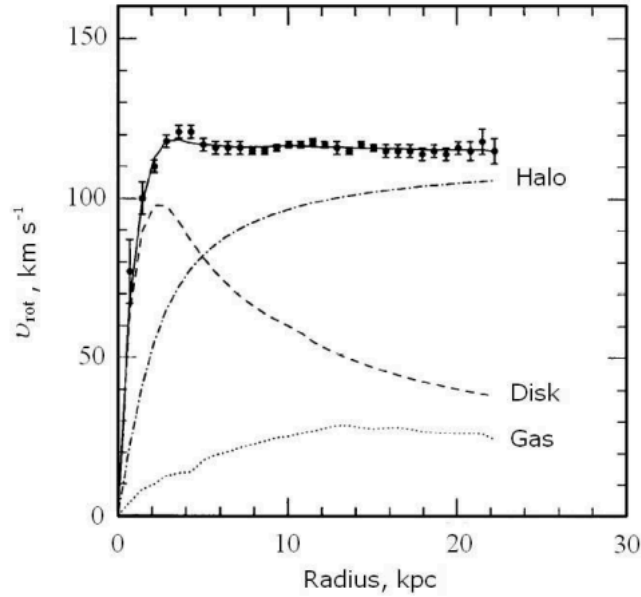


Figure 1.1: The rotational curve versus the distance from the center of the galaxy. The proposed dark matter effect is depicted by the dashed line. Image source [5].

1.2.2 Gravitational lensing

The bending of light rays emitted from distant sources (galaxies) and passing a massive objects or matter can be described through general relativity. Gravitational lensing can be used to measure the distribution and expansion history of matter in the Universe. The method was first discovered by D. Walsh, B. Carswell, and R. Weymann in the year 1979 [6, 7]. Gravitational lensing causes the light to bend when it is closest to the center of the massive lensing object, while the effect decreases as it goes away from the center. Consequently, the gravitational lensing has a focal line rather than a focal point, which is the case in optical lensing. This phenomenon was first quantified by Albert Einstein in the year 1936 [8], when he considered the possibility of having a star in a galaxy producing a gravitational image for a star located far away

beyond, so, if the alignment is perfect, the result would be a ring-like image. Hence, this is referred to in the literature as “Einstein Ring”, as shown in figure 1.2.

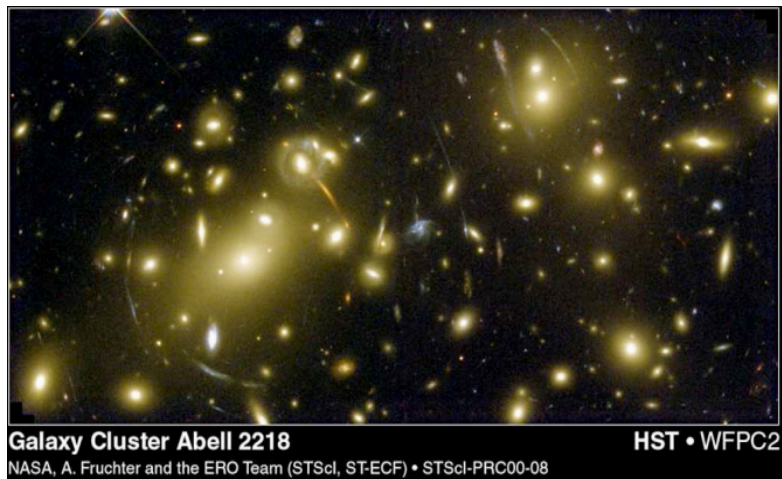


Figure 1.2: Gravitational lensing caused by bending of light while approaching a massive region. Image courtesy (NASA Archive).

1.2.2.1 Classes of gravitational lensing

Lensing by clusters may occur in three regimes:

- Strong lensing: which is characterized by the formation of Einstein Rings, arcs and multiple images that can be seen by the eye.
- Weak lensing: it occurs with distant objects where the deformations of the background galaxies are much smaller and can only be detected by analyzing a large number of sources [9, 10].

- Microlensing: almost no deformation can be seen. However, the amount of received light from the source is changing over time.

By analyzing the pattern of distortions in the image of the background galaxies, it is possible to reconstruct the matter distribution of the lensing object providing a map of the dark matter [11]. So, we can conclude that the bending of light, or lensing observations, has been exposed as an aspect of the nature of dark matter itself; the dark matter behaves like collisionless particles, and not like a diffuse gas at all [6]. So if we are interested in finding how much mass is there in a cluster, or where that mass is located, then measuring the background sources of all light coming from behind the cluster empowers the weak gravitational lensing to show where dark matter is.

1.2.3 The Bullet Cluster

A cluster, in simple words, stands for a group of similar objects. However, in astrophysics, it stands for an enormous group of galaxies. In the context of the cosmological cold dark matter model, the Bullet Cluster represents an example for clusters in collision. This recent result shows the power of combination of different probing methods – X-ray observations of the distribution of hot gas, optical observations, and dark matter distribution mapping by gravitational distortion of images in the background galaxies – on the mass distribution of clusters [6, 12].

The Bullet Cluster in figure 1.3 represents a rare and direct evidence of the existence of dark matter. The Bullet Cluster is composed of two sub-clusters which underwent a collision ~ 100 *Myr* ago and passed through each other. The clusters are moving with a velocity of ~ 4500 *km/s* relative to each other, determined from the gas density jump at the bow shock. While the two sub-clusters are in the path of collision, the hot X-ray emitted from the intra-cluster gas is spatially separated from the sub-galaxies, which behaves like a collisionless particle, while the plasma experiences a thrust pressure and slows down. The calculated relative velocity with the current 0.66 Mpc separation between the two sub-clusters suggest that they were closest to each other 100 – 200 *Myr* ago [13].

X-ray telescopes can be used to derive the distribution of plasma, and optical telescopes can be used to derive the distribution of collisionless galaxies, while the overall mass distribution is calculated through weak gravitational lensing. By comparing these results, it was found that mass distribution does not trace the dominant luminous component “intra-cluster gas,” but the distribution of galaxies, indicating that the cluster mass is dominated by collisionless dark matter.

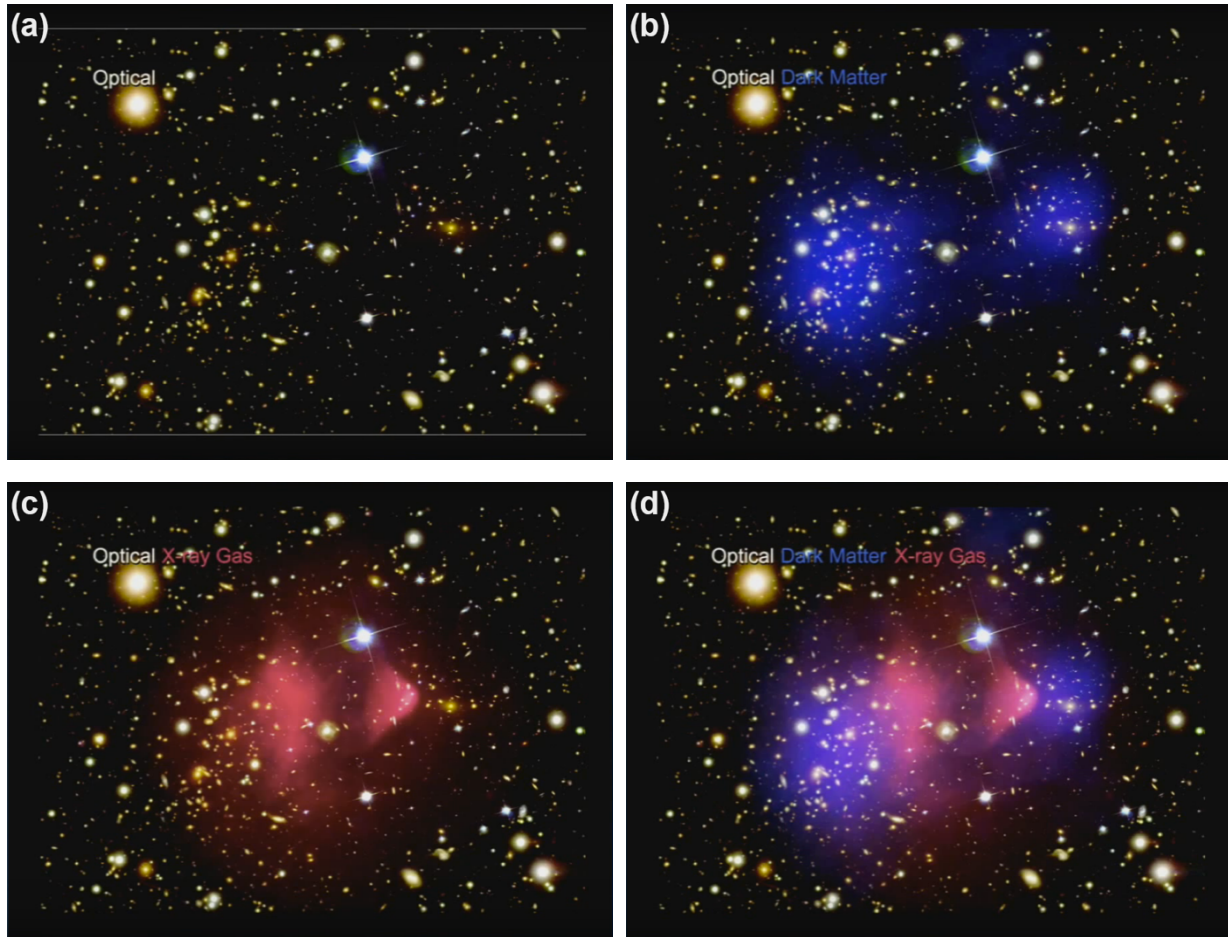


Figure 1.3: Evidence of dark matter in galaxy clusters. The hot gas (in red) and dark matter (in blue). *Panel (a)*: Image using the visible wavelength (optical). *Panel (b)*: Blue blobs show the location of the mass (dark matter). *Panel (c)*: X-ray telescope image show the plasma distribution and shock as a result of a collision. *Panel(d)*: Hot gas and gravity are at different locations, which show the present observable state of the two clusters. Image courtesy: Chandra X-ray Observatory.

1.3 Candidates for Dark Matter

There is no clear answer to the question about what dark matter can be. However, there is a definite answer for what dark matter cannot be. Dark matter candidates are tested using observations from different instruments. There are two leading basic candidates for cold dark matter; non-thermal axions and Weakly Interacting Massive Particles (WIMPs). WIMPs were motivated by the supersymmetric extensions of the Standard Model, as supersymmetry (SUSY) suggests that all known fermions in the SM have a corresponding boson, and all known bosons in the SM have a corresponding fermion particle. However, none of those hypothetical particles have been found yet.

1.3.1 Weakly Interacting Massive Particles (WIMPs)

The WIMP is a generic theoretical sub-atomic particle that has an expected mass which is about 10 to 10,000 times greater than the mass of a proton ($m_\chi \sim GeV - TeV$). It can be classified as one of the Supersymmetric candidates. WIMPs are characterized by their mass and cross-section, they are electrically neutral, and do not interact with light.

It is also expected that WIMPs may have been formed at the early stages of the Universe, and they have a suitable amount of abundance to account for the observed relic density [14]. But, it is a great challenge to detect WIMPs, as the average expected deposited energy is relatively low; in

the order of few keV – few tens of keV . The isolation of radioactive background plays a vital role in the search for WIMPs, due to the low event rate of WIMP interaction with baryonic matter. Hence, it is necessary for experiments searching for direct interaction between WIMPs and baryonic matter to be located underground, in order to improve the signal-to-noise ratio, by reducing the exposure to cosmogenic radiation [15, 16].

1.3.2 Axions

The existence of axion was motivated by the fact that the Standard Model has some flaws. It is perfect of course, in the sense that it can interpret and predict different physical interactions. However, it is expected according to the SM that strong interactions violate Parity and Charge-conjugation, but they do not. Moreover, the axion is also considered to be the lightest supersymmetric particle.

The SM gives predictions and interpretations for a wide variety of physical interactions (electromagnetic, weak, and strong). However, the strong CP problem, which is represented by a lack of CP violation in strong interactions, was the motive for Roberto Peccei and Helen Quinn to look for possible interpretations [17, 18]. So, the axion first emerged in connection to the problem in QCD, where there is an extra term θ in the Lagrangian QCD. The theoretical description of the Lagrangian for strong interactions can be written as:

$$L_\theta = \theta \frac{g^2}{32\pi^2} F_a^{\mu\nu} \tilde{F}_{a\mu\nu} \quad (1.2)$$

where $\tilde{F}_{a\mu\nu}$ is the gluon field strength tensor and $\tilde{F}_{a\mu\nu}$ is the dual tensor. The theorists in particle physics do not provide interpretations to the expected axion mass if they exist. While astrophysicists and cosmologists intensely constrain it. Also, for the axion to be an acceptable cold dark matter candidate, they must have extremely light mass \sim one billionth of the mass of an electron. Although axions have light mass, they are produced with extremely small K.E, and thus, could form cold dark matter, rather than hot dark matter, as would usually be expected of such light particle [18].

If we consider breaking the PQ symmetry, then, the mass of the axion can be related to the spontaneous breaking of symmetry f_a as the following:

$$m_a \propto \frac{1}{f_a} \text{ and } g_{ai} \propto \frac{1}{f_a} \quad (1.3)$$

where f_a is inversely proportional to the mass of the axion m_a , and to the coupling constant g_{ai} between the axion and particle i [19]. It is also expected that axions are able to couple with different particles, such as fermions, gluons, and photons. The proposed interaction is mediated by virtual particles, because photons do not couple with the uncharged axion. However, most of the axion search experiments are based on the axion-photon coupling. The Lagrangian of axion-photon interaction is given by:

$$\mathcal{L}_{a\gamma\gamma} = g_{a\gamma\gamma} a (\vec{E} \cdot \vec{B}) \quad (1.4)$$

where a is defined to be the axion field, \vec{E} and \vec{B} are the electric and magnetic fields of the two propagating photons respectively, as shown in figure 1.4 [20].

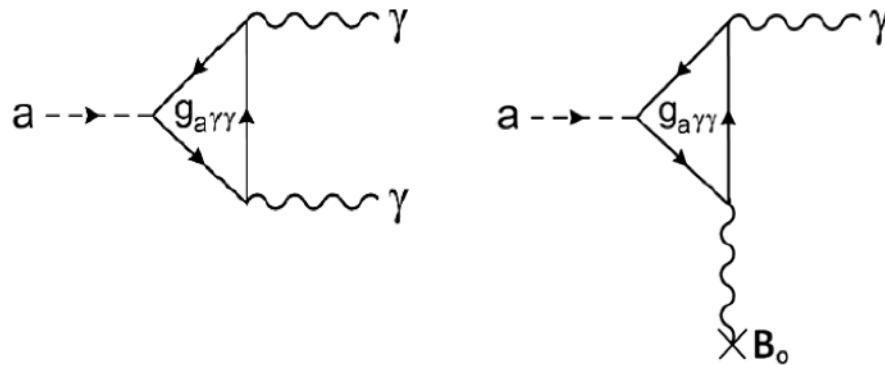


Figure 1.4: *Left panel:* Feynman diagram of axion decay into photons.
Right panel: conversion into a vacuum. Image source [20].

In figure 1.5 the red and blue lines represent lower and upper coupling limits in the search for axion [17]. The axion search experiments, some are shown below, try to improve their sensitivity in order to reach, and fully scan the expected axion mass limited to those coupling limits.

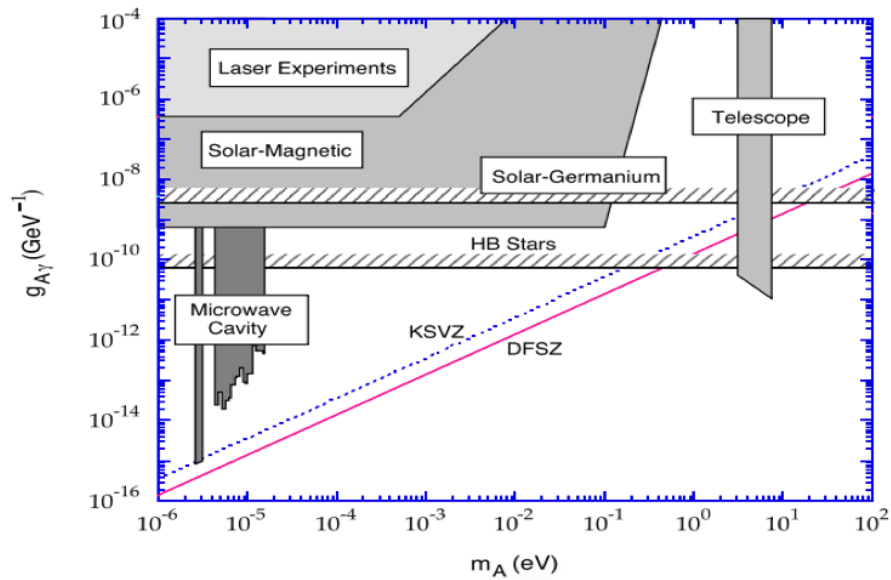


Figure 1.5: Exclusion limits for axion mass, as reported from axion search experiments with respect to both upper and lower limits. Image source [17].

The first model is KSVZ which stands for (Kim-Shifman-Vainshtein-Zakharov) and provides the stronger coupling limit, the second model is DFSZ (Dine-Fischler-Srednicki-Zhitnitskii) which provides the weaker limit [21, 22]. The importance of these models lie in the fact that they are considered to be a solution to the strong CP-problem; in first limit there are one or more new

heavy quarks expected to carry the charge, while in the second limit the SM fermions and Higgs boson may carry the new charge [23].

1.4 The search for WIMPs

WIMPs are assumed to be produced in thermal equilibrium at the early Universe and to interact with SM particles. So, if WIMPs do interact – apart from gravitational interaction – with baryonic matter, then the interaction might be mediated by an unidentified particle (till the moment) [24]. Hence, the experiments aiming to detect WIMPs can be classified, based on their interaction with SM particles into three different categories as depicted in figure 1.6.

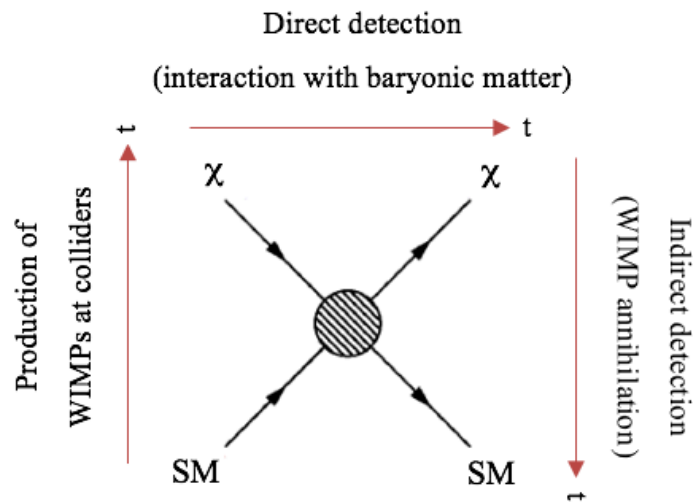


Figure 1.6: Dark matter detection methods, based on the proposed interaction between dark matter and particles from the Standard Model.

1.4.1 Direct detection

The direct detection method searches for collisions between the invisible WIMP particle, and the nuclei of the SM particle. So, it is expected that this method should have the WIMPs scattering, mostly elastically, from another material inside a detector. The detectors can be designed to detect energy depositions inside the detector's material. But, since those hypothetical particles move at relatively low velocities, they have a small momentum, and the deposited energy into the detector will be relatively small. The energy estimate is in the range of few eV for electron recoil, and few keV for nuclear recoil [25] and the expected output signal from terrestrial detectors can be represented as the differential of nuclear recoil rate as a function of recoil energy dR/dE_R [26].

Figure 1.7 depicts the different detection methods which usually combines between two signal types. Having two signal types allows the rejection of large fraction of the background [27] and the ratio between any two quantities depends on the ionization density (dE/dx), which in turn depends on the type of particle interaction in the detector.

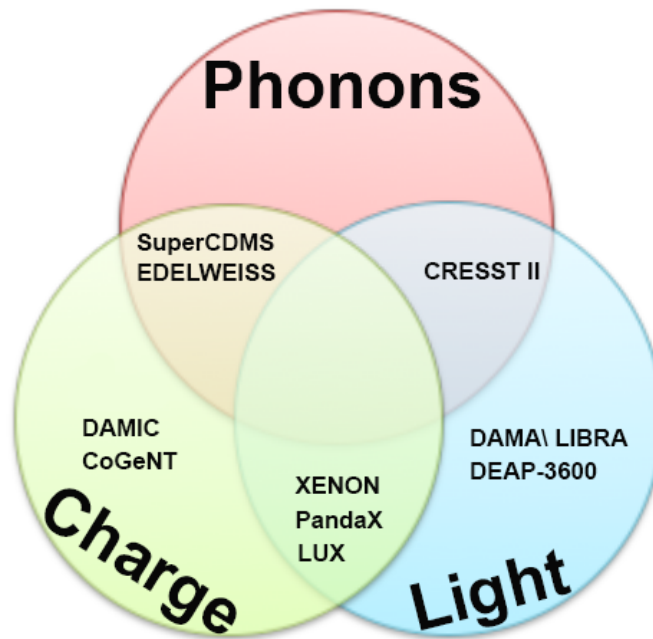


Figure 1.7: A classification of dark matter search experiments based on the type of measured signal.

1.4.2 Indirect detection

The indirect search is based on the idea that dark matter annihilated in the early Universe into different types of particles, and perhaps they are still annihilating today. So, this type of experiments is searching for the annihilation products (such as gamma ray, positrons, and cosmic-ray electrons) of this dark matter particle into a standard model particle. Gamma ray is considered as one of the major annihilation products, due to its propagation ability from the source with substantially no absorption. Hence, gamma ray detection is considered to be a good tool for identifying the source of emission [28].

This type of detection is performed either in space or on the ground surface. Experiments such as Fermi Large Area Telescope (LAT), GAMMA-400 and Alpha Magnetic Spectrometer (AMS-02) are examples of space-based experiments. On the other hand, the Cherenkov Telescope Array (CTA), Major Atmospheric Gamma Imaging Cherenkov (MAGIC), and High Energy Spectroscopic System (H.E.S.S.II) are examples of ground-based experiments [29].

Chapter 2

SuperCDMS Experiment

The Super Cryogenic Dark Matter Search (SuperCDMS) experiment is considered one of the leading particle astrophysics experiments in the direct search for WIMPs, through their interaction with germanium and silicon nuclei in terrestrial detectors. The CDMS experiment initially started in the mid 90's at the Stanford Underground Facility (SUF), located ~ 10.5 *m* below the surface. The experiment reported its results a few years later, setting an upper exclusion limit of WIMP-nucleon cross-sections larger than $\sigma \approx 3 \times 10^{-42} \text{cm}^2$ for WIMP mass $m_\chi \approx 50 \text{ GeV}/c^2$ [30, 31, 32]. The second stage of the experiment, CDMS II, started around the year 2000 at Stanford, then moved to the Soudan Underground Laboratory – Minnesota, U.S.A around the year 2003. The laboratory is an old iron mine, located 689 *m* below the surface, providing approximately 2000 *mwe* effective shielding to cosmic rays [25]. By the year 2005, WIMP-nucleon cross-sections greater than $\sigma \approx 4 \times 10^{-43} \text{cm}^2$ for WIMP mass of $m_\chi \approx 60 \text{ GeV}/c^2$ were excluded [33]. Around the year 2010, CDMS II was operating an array of 30 detectors before turning into SuperCDMS at the Soudan Underground Laboratory (SUL), in which improved detectors of interleaved electrodes, and more mass were employed. The SuperCDMS experiment was recently decommissioned at the end of the year 2015, and part of the latest results are shown in chapter 6.

The high voltage mode of SuperCDMS is the CDMS low ionization threshold experiment (CDMSlite), which utilizes germanium detectors operating at high bias voltage (69 V). CDMSlite have reached $\sim 56\text{ eV}$ threshold energy for electron recoils, and the results were able to exclude a new parameter space for the WIMP-nucleon spin-independent cross-section in the WIMP mass domain of $(1.6 - 5.5)\text{ GeV}/c^2$.

The plan now is to have the new generation of the experiment – SuperCDMS SNOLAB – at Sudbury Neutrino Observatory (SNO) Laboratory – Ontario, Canada by the year 2020 [34]. The SNOLAB is located 2000 m below the surface, which provides 6000 *mwe* effective shielding [25]. This change in experiment location to a deeper site, will overcome the limitation of the SuperCDMS due to cosmogenic radiation. Moreover, the plan for the new location at SNOLAB is to have a greater target mass and an improved detector technology that improves the sensitivity toward low mass WIMPs ($0.3 - 10\text{ GeV}/c^2$). Additionally, the hope is also to build a facility that is capable to reach the solar neutrino floor.

2.1 Detectors between the past and the future

The idea of CDMS experiment is to detect a new type of radiation, that has never been observed before, hoping that the analysis of this radiation would fit the theories behind the existence of dark matter. In order to achieve this, the first generation of the experiment started by utilizing a semiconductor crystal, germanium ($\sim 250\text{ g}$) and silicon ($\sim 100\text{ g}$) as its terrestrial detectors, with each detector being about 7.5 cm in diameter and 1 cm in thickness. The detectors contained four phonon channels on one side and two charge channels on the other side and they were called *Z*-sensitive Ionization Phonon (ZIP) detectors. The full capacity of CDMS

II included the utilization of 19 germanium and 11 silicon ZIP detectors. SuperCDMS had an improved detector technology with a total target mass of ~ 10 kg. The detectors were ~ 620 g in mass, 7.5 cm in diameter, and 2.5 cm thick. The interleaved Z-sensitive Ionization Phonon (iZIP) detectors for SuperCDMS contained four phonon channels interleaved with two charge channels on each surface. In terms of detector improvement for the next experiment at SNOLAB, the plan is to have six phonon channels interleaved with two charge channels on each side. The new iZIP detectors are expected to have a mass of ~ 1.4 kg, and to be 10 cm in diameter and 3.3 cm in thickness. The experiment at SNOLAB will start with about 30 kg target mass and is expected to increase up to ~ 200 kg.

2.2 Queen's Test Facility

The Queen's Test Facility (QTF) is one of the several test facilities within the SuperCDMS collaboration. The dry dilution refrigerator, also referred as "*cryostat*" at QTF, is able to cool the base plate – discussed in the following section – down to 10 mK without having the detectors or the detector holding structure, "the tower", installed inside the cryostat.

QTF is playing an important role in the research and development domains as well as in the preparation for the new experiment at SNOLAB by conducting some important measurements and tests required from the SuperCDMS collaboration. Some of those measurements are discussed in the following chapters (3, 4 and 5). After the decommissioning of the experiment in SUL, we received one of the SuperCDMS towers (T2) containing three iZIP detectors. The presence of these detectors will lead to improve QTF future measurements, since those detectors have a better energy resolution (~ 300 eV) compared to (~ 1 keV) for the detector available in

QTF since 2012. In this chapter, the focus will be on QTF infrastructure, cryostat operation, and the details of the cold hardware and readout electronics.

2.3 QTF Dilution Refrigerator

The QTF cryostat is from Oxford Instruments. It has two main cooling systems – the pulse tube cooler and the dilution refrigerator. A cross-sectional view of the cryostat is shown in figure 2.1 [35].

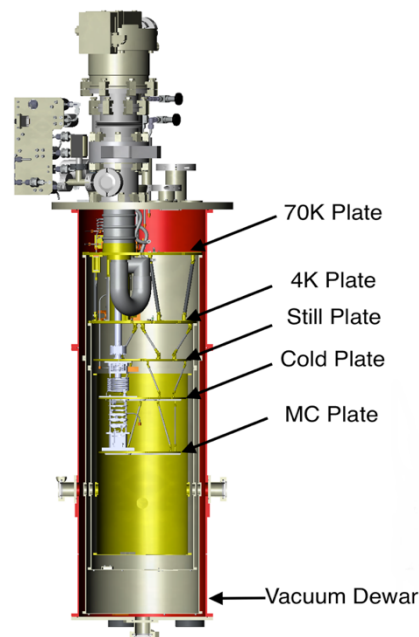


Figure 2.1: A cross-section view, showing the different stages of QTF dilution refrigerator. There exists a radiation can at each of 70 K, 4 K and still plate in addition to a vacuum Dewar at room temperature. Image source [35].

The temperature stages of the cryostat are: 70 K stage, 4 K stage, still plate (~ 800 mK), cold plate (~ 70 mK), and mixing chamber plate (~ 6 mK). The 70 K stage is named after the wet fridge's 70 K stage cooled by liquid nitrogen. However, the actual temperature in QTF is ~ 65 K, and the plate is cooled down using the first stage of the pulse tube (PT) cooler. Basically, the PT cooler (model PT407) has two cooling stages. The first has a cooling power of 22 W at 55 K and the second stage has 0.6 W cooling power at 4.2 K [36].

When the cooling process starts, the PT cooling power is expended to cool down the first two stages (70 K and 4 K), while a cold mixture of $^3\text{He} - ^4\text{He}$ is circulated in a “pre-cool” circuit by a compressor to cool down the lower three stages (still, CP and MC). The cooling process is monitored using thermometers connected to the readout bridge, which is an electronic control unit that is able to log all the data from all gauges and eventually make it available on a special GUI.

The cool-down can either be done step-by-step (manually) or by using a fully automated procedure. In both cases, the pre-cool circuit continues to circulate the $^3\text{He} - ^4\text{He}$ mixture until the temperature of the mixing chamber plate reaches ~ 10 K, then, the mixture will be collected from the pre-cool circuit back into the mixture tank. Once the mixture is collected, a condensation process starts, using a different circulation that includes a compressor, a fore-pump, and a turbo pump. All three pumps work in unison to maintain the circulation and condensation process. The Lambda point of the He mixture is at 867 mK and 67% of ^3He concentration, as shown in figure 2.2, and phase separation occurs below that temperature [37].

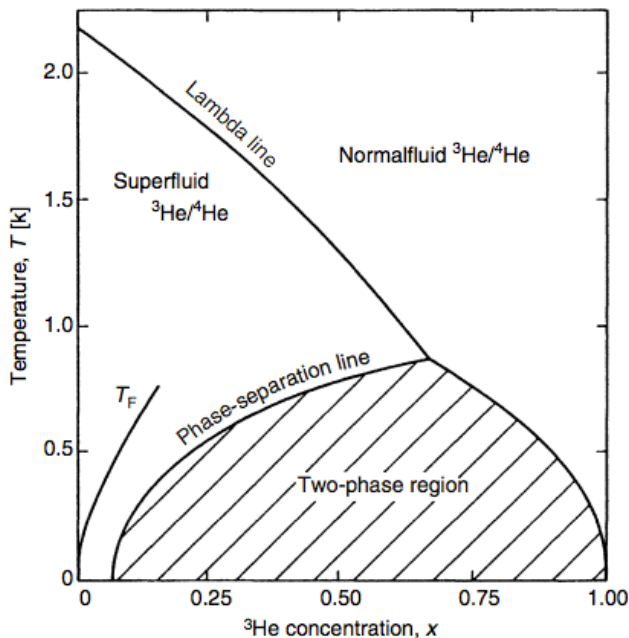


Figure 2.2: The phase separation for the mixture. The x-axis represents the ratio of ^3He atoms to the total number of atoms, and the dashed region represents a forbidden region for the mixture to exist. Image source [37].

So, at lower temperatures, there will be one denser phase rich in ^4He and a less dense phase that is rich in ^3He . Gravity plays an important role here in separating the two phases at the mixing chamber of the cryostat, as depicted in the figure 2.3.

The cooling is accomplished as ^3He diffuses from ^3He concentrated phase to ^3He diluted phase. This diffusion is driven by the difference in the enthalpy between concentrate and dilute phases. Since the density is less for the pure ^3He phase, it means that there is less mass and that the enthalpy for the concentrated phase is much lower than that for diluted phase.

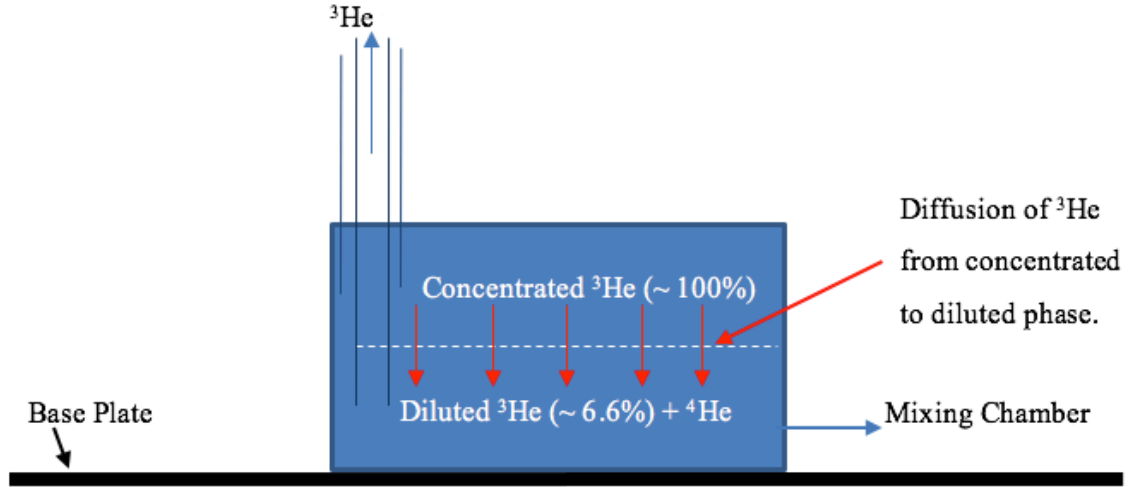


Figure 2.3: The mixing chamber (not to scale) sitting on the base plate. Where the process of phase separation is taking place and ^3He diffuses from concentrated to diluted phase inside the chamber. At temperature close to 0 K, the concentration of ^3He in diluted phase is $\sim 6.6\%$.

The process increases the entropy as ^3He diffuses and heat is taken from the surroundings, which consequently, cools the surrounding down. As long as the phase separation occurs at a low temperature, that will sustain the necessary osmotic difference in pressure between the mixing chamber and the still [38]. The cooling power of the dilution refrigerator can be expressed as:

$$\dot{Q} = \dot{n} \Delta H \quad (2.1)$$

where \dot{Q} is the rate at which heat is absorbed from the surroundings, \dot{n} is the number of diffused helium atoms and ΔH is the change in energy from one phase to the other. Where $\Delta H = T (S_D - S_c)$ is the change in entropy between dilute and concentrate phases.

Eventually, the cryostat is used to cool down the germanium and silicon crystals to the operating temperature ($\sim 45\text{ mK}$), and that is to be able to sense any tiny energy deposition that might result from WIMP interaction [39].

2.4 Cold Hardware and Readout Electronics

The cold hardware and readout electronics mainly consists of all detector wiring, starting from the E-box (evacuated box at the top of the cryostat where wiring ends at a 50-pin connector) at room temperature, down to the detector housing at the milli-Kelvin stage. The stripline is made of shielded copper and kapton flex circuit, and represents the electrical connection between the tower electronics at 4 K and the E-box of the cryostat at room temperature. The striplines are heat sunk at the 70 K and 4 K plates in order to reduce the load on the dilution fridge. The tower shown in figure 2.4 [40], is showing the different thermal stages connected by carbon tubes to give the necessary thermal isolation and mechanical support to the tower structure. Each stack in the SuperCDMS experiment contained three iZIP detector, and some used to be running in high voltage mode as part of the CDMSlite experiment.

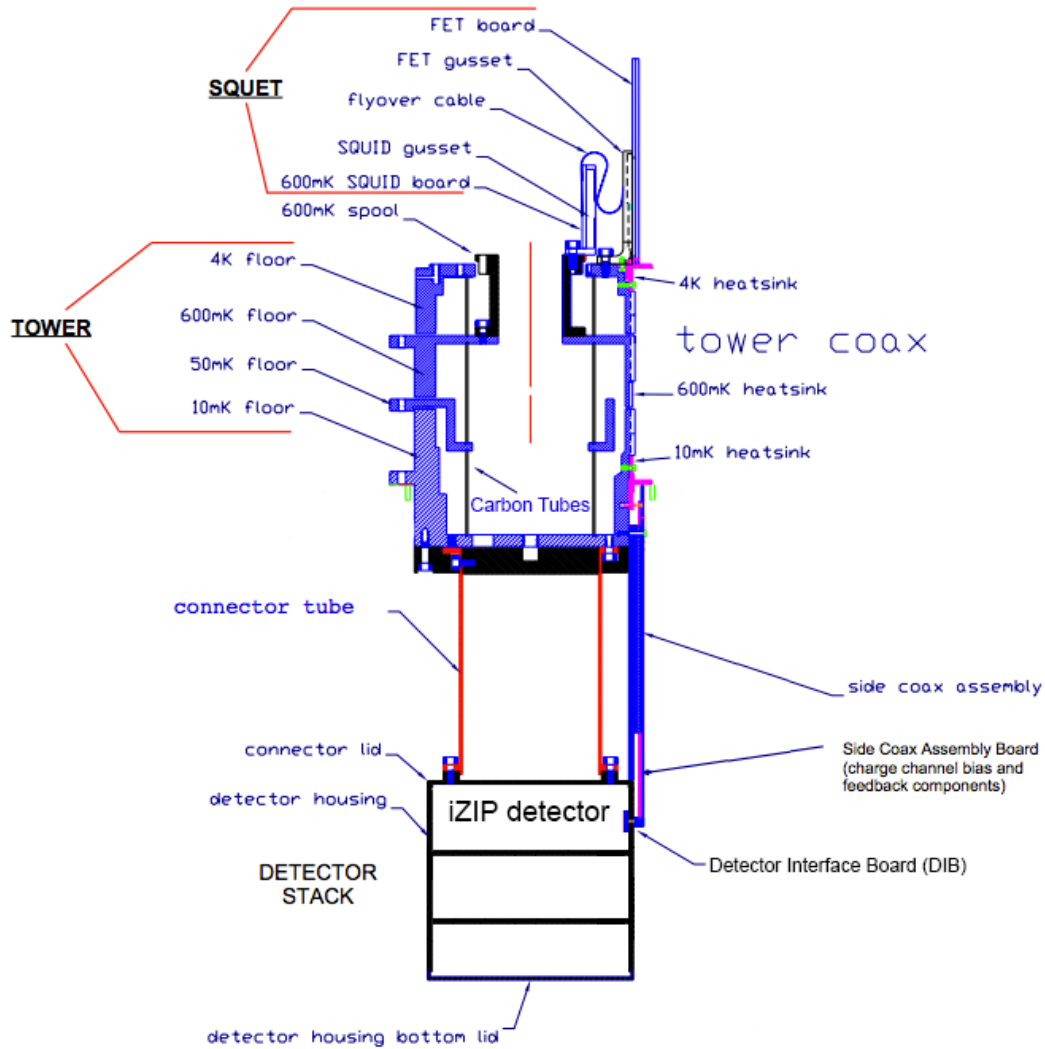


Figure 2.4: A schematic diagram of the cold hardware from the SuperCDMS experiment at SUL, showing the different thermal stages of the tower supported by carbon tubes to give the necessary thermal isolation and to support the tower structure. Each stack in the SuperCDMS experiment has three iZIP detectors. Image source [40].

2.4.1 SuperCDMS Detectors

The SuperCDMS experiment uses ultra-pure semiconductor (germanium and silicon) crystals. The crystals are cylindrical in shape and are held inside the detector housing by kapton clamps to provide the necessary electrical and thermal isolation. The detector is kept at low temperature ~ 45 mK during the course of operation. The phonon and charge signals are carried out of the detector to the side coax through the Detector Interface Board (DIB). The DIB is a cirlex pad attached on the detector housing, shown in figure 2.5, and the side coax is an electronic device with functional elements and dielectric-free coaxial wiring ending up with pins to form a connection between the DIB and the tower face within the tower structure. SuperCDMS detectors contain four near infrared Light Emitting Diodes (LEDs) emitting photons with wavelength 940 nm [41]. Those surface mount LEDs are glued using a conductive epoxy (Ag) on the DIBs, and they were selected because they have a radiation angle of 140° at the cathode surface to ensure the maximum photon spread over the detector [42]. The LEDs are used to bake or flash the detector, that is to neutralize the detector by emitting huge number of photons from the LEDs towards the detector in order to produce electron-hole pair (e^-/h^+) which recombine with the trapped charges and neutralize the detector.

Detector neutralization leads to an improvement of the charge collection efficiency and is necessary in order to free the trapped charges, which gets stuck in the crystal impurities, hence, they have no contribution to the charge signal.

The SuperCDMS detectors were improved a few times during each phase of the experiment. The most recent generation is the iZIP detector shown in figure 2.5, contains four grounded

phonon channels covering equal areas and interleaved with two voltage-biased charge channels (Q_{inner} and Q_{outer}) on each side of the detector [43, 44].

The iZIP detector has the ability to simultaneously measure the athermal phonons and the charge ionization signals due to particle interaction inside the crystal. The total energy (E_{total}) is used

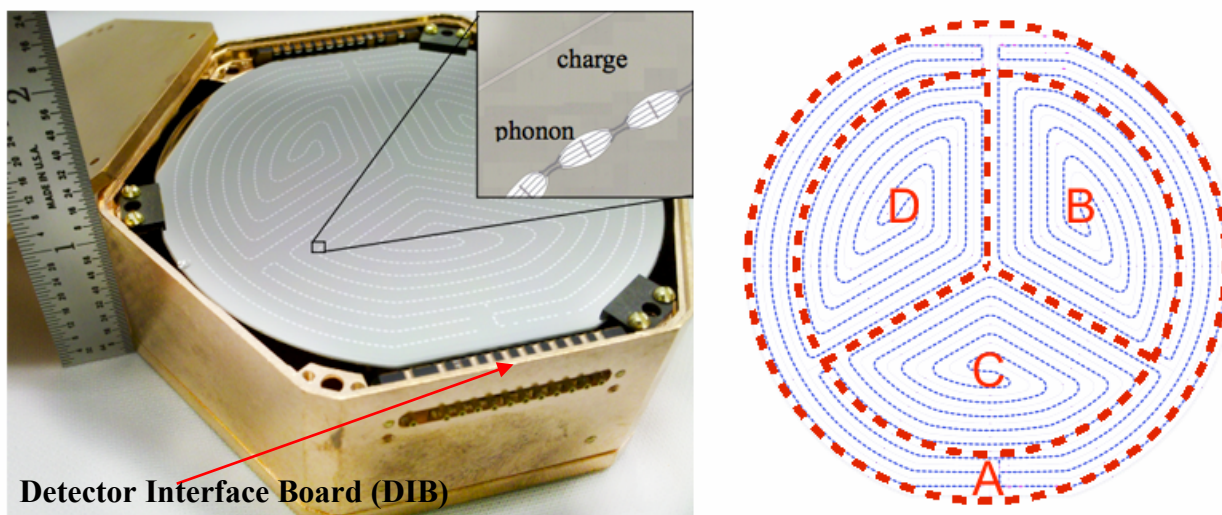


Figure 2.5: A 620 g germanium iZIP, Mercedes-like design detector. Image source [43, 44].

to calculate the recoil energy (E_{recoil}) after considering the simultaneous measurement for the ionization (charge) and the phonon (heat), in addition to the correction from the amplified phonon signal due to the bias voltage. This effect is called Neganov-Luke Amplification and will be discussed in section 4.2. In the case of iZIP detectors, they were biased at $\sim 4 V$ during operation and the ionization yield was evaluated for each individual event [45].

The recoil energy can be expressed as:

$$E_{recoil} = \frac{E_{total}}{(1 + Y_{ionization} \times (\frac{eV_{bias}}{\varepsilon}))} \quad (2.2)$$

where ε is the average energy per e^- / h^+ pair in germanium ($\sim 3 \text{ eV}$ at 50 mK) [46]. And V_{bias} is the detector's bias voltage during operation. And $Y_{ionization}$ is the ionization energy for each recoil energy, which can be expressed as:

$$Y_{ionization} = \frac{E_{ion}}{E_{recoil}} \quad (2.3)$$

2.4.2 SQUET Cards

The SQUET card consists of the following two main elements, the Superconducting Quantum Interference Device (SQUID) board that is heat sunk at the still stage ($\sim 800 \text{ mK}$) and the Field Effect Transistor (FET) board that is that is heat sunk at the 4 K stage and attached directly at the tower by a 16-pin connector. The FET has a role in maximizing the noise performance for the electrodes, and each card has four SQUID arrays which are used to measure the phonon signal (one SQUID per phonon channel). The two boards are attached to each other by a superconducting twisted pair cable, the flyover cable, as shown in figure 2.6. Having the SQUID board at the still temperature allows for the reduction of their internal noise. For further noise reduction, the dilution fridge is shielded prior cooling down, which results in $\sim 20 \%$ of relative noise reduction.

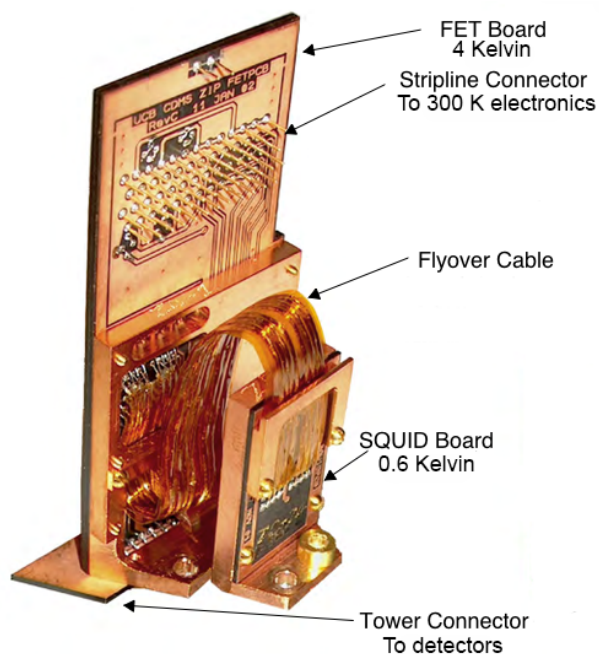


Figure 2.6: SuperCDMS SQUET card.

From figure 2.6, we can see the tower connector at the bottom of the FET board, and that is where the SQUID and FET signals are transferred from the detector (~ 45 mK) through the side coax, then up to the 4 K stage. Having the FET board at the 4 K stage helps in transmitting the output signal within such a short distance, which prevents warming up or having a heat load being put on the dilution refrigerator.

2.4.3 Phonon readout circuit

The phonon collectors are composed of superconducting aluminum fins which remain in the superconducting phase during detector operation (the critical temperature for aluminum: $T_{cAl} = 1.2$ K [47], while operation temperature ~ 45 mK). Each one of the phonon channels has an

identical readout circuit, so there are 4 phonon readout circuits per SQUET card. Once an interaction is taking place inside the crystal, then energy will be dissipated into the germanium or silicon substrate and primary phonons are released, as shown in figure 2.7 [48]. Knowing that aluminum is in superconducting state, the phonons diffused into the aluminum film are used to break the Cooper pairs. If the phonons have enough energy, quasiparticles will gain kinetic energy and will be free to move. Then, their kinetic energy starts to decrease after the motion. Although energy is lost and some quasiparticles are trapped at the quasiparticle trapping zone, as depicted in figure 2.7, they cannot recombine, unless each couple has the same amount of energy and opposite momentum.

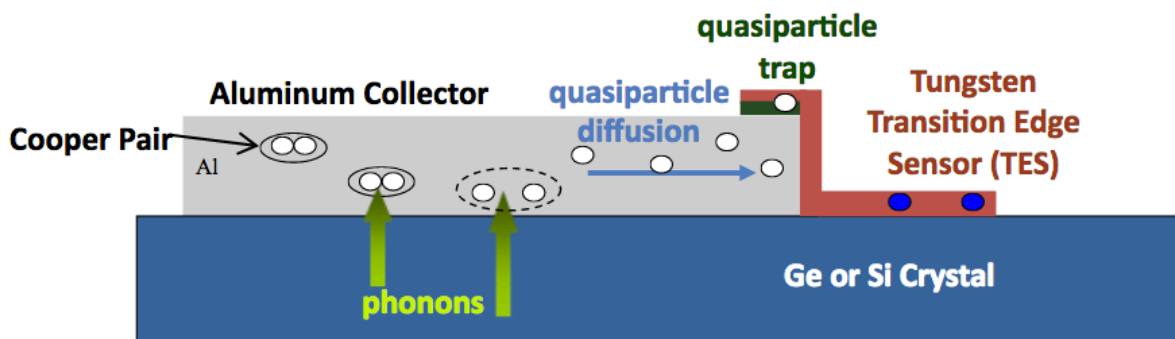


Figure 2.7: A schematic drawing (not to scale) for the Superconducting Quasiparticle-trap-assisted Electrothermal-feedback Transition-edge phonon sensor (QET), and the mechanism through which phonons are collected from the crystal. Aluminum fins and TES cover a large surface area on both detector surfaces. In addition, they have low heat capacity; hence, thermalization with the detector occurs very quickly.

So, most of the electrons will be free and will move around, while those who lost a considerable part of their kinetic energy will be collected at the TES sensor [49]. On the other hand, the tungsten sensor has almost no bandgap because the TES is set at the edge of its transition phase during detector operation. So, any deposited energy will break the Cooper pairs; thereafter which, charges will be collected from the sensor to the readout circuit.

The TES is an array (over 1000 sensor per channel) of thin superconducting tungsten (W) film, coupled to an aluminum fin. It is voltage biased and connected in parallel to a shunt resistor ($R_s \sim 20 \text{ m}\Omega$) with a bias current (I_b) running through it. TES is one of the many sensor types used in cryogenic detectors, which basically converts the phonon energy into electrical signals. It is very practical in cryogenics due to the change in its resistance for any slight change in temperature. Hence, in the case of any event or interaction inside the crystal, energy will be deposited into the crystal, and it will have a direct effect on the TES's temperature. The change in the TES temperature, (ΔT) will yield in a dramatic change in its resistance (ΔR), as shown in figure 2.8, where the critical temperature represents the point at which resistivity drops to zero [50].

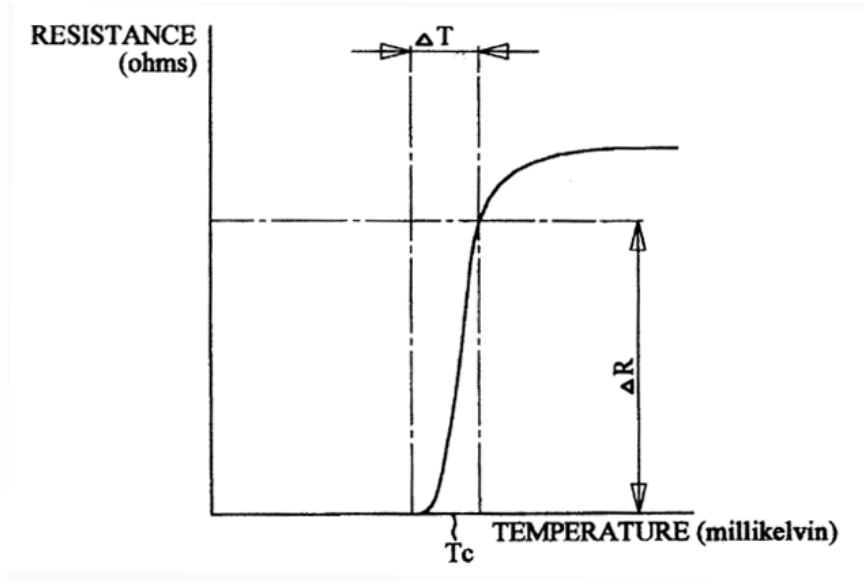


Figure 2.8: The transition from superconducting to normal state in TES.

Image source [50].

If the bias current (I_b) is constant, then, the change in TES resistance will cause a change in the current flowing through the coil (L) shown in figure 2.9. When the current changes, the coil's magnetic field will be changing as will.

The current passing through the TES can be represented by:

$$I_{TES} = I_b \frac{R_s}{R_s + R_{TES}} \quad (2.4)$$

where, R_s represents the shunt resistance. Additionally, the power dissipated in the TES is given by:

$$P_{TES} = I_{TES}^2 R_{TES} \quad (2.5)$$

Knowing that the SQUID array shown in figure. 2.9 [51] is a current-biased array and reacts by changing the voltage, which causes the amplifier to counteract the change by increasing the current in the feedback coil in order to balance the change in the SQUID array voltage.

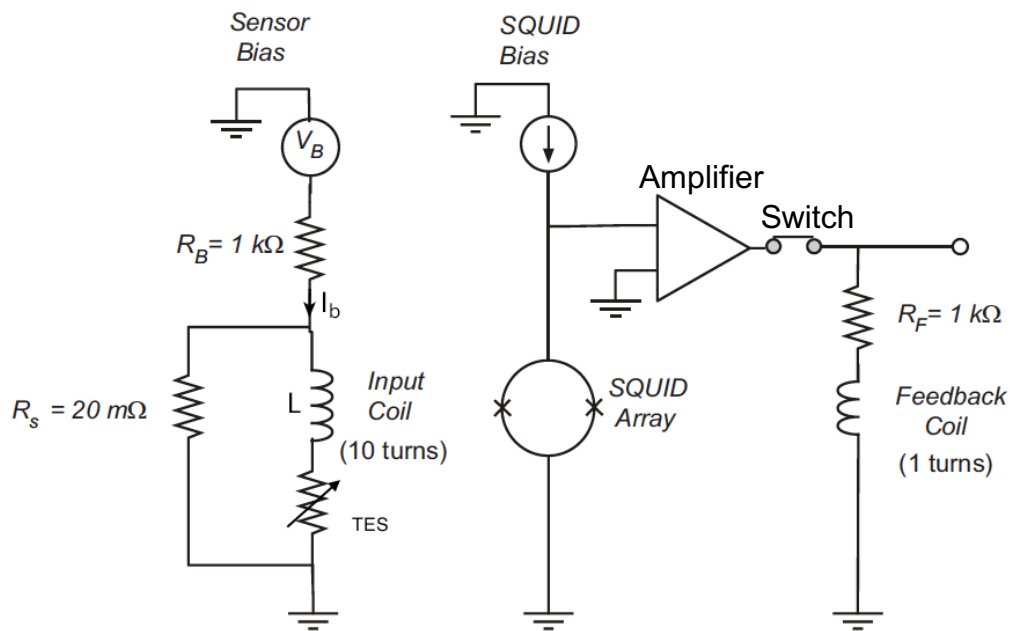


Figure 2.9: A schematic diagram for the phonon readout circuit. Image source [51].

There are 10-times as many turns on the input coils than on the feedback coil, which causes a current gain of 10 times in the feedback circuit. Having the feedback resistor connected on the FET board, in series with the feedback coil, eventually gives the amplifier its output signal.

2.5 SuperCDMS results

The trend in searching for lower WIMP masses is supported by several factors, such as the extra emission of gamma ray from the Galactic center [52] and some indications of WIMP signal close to the detectors' threshold energy. From the published results [53] it is clear that SuperCDMS SNOLAB experiment will be leading other WIMP search experiments at the low WIMP mass region [54], and maybe will be able to detect dark matter particles or to add another slice to the excluded parameter space as shown in figure 2.10.

When reaching the neutrino floor, WIMP search experiments will basically encounter a background that is not possible to be shielded using the current techniques, and we reach to a signal that cannot be distinguished from WIMP signal. Hence, other methods have to be implemented to search for WIMPs or other dark matter candidates once the neutrino floor been reached by the current experiments.

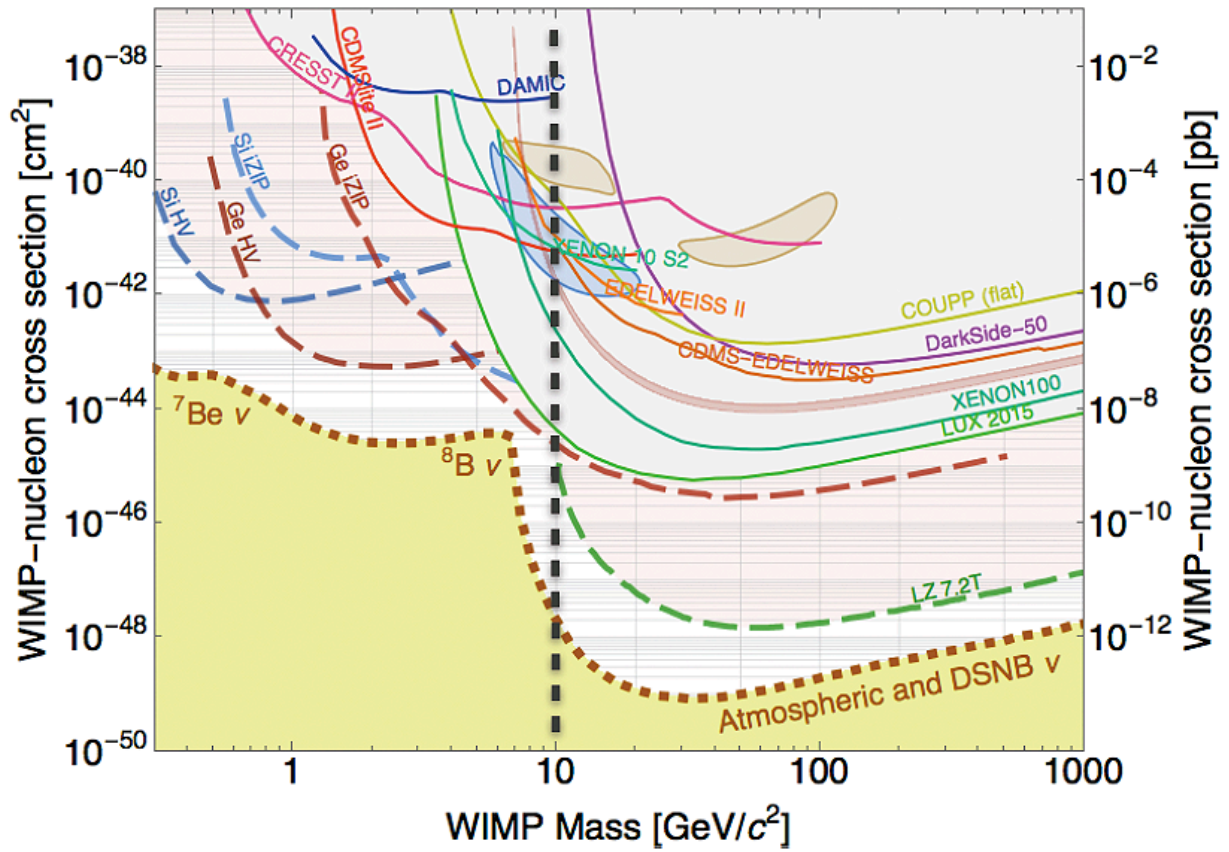


Figure 2.10: Latest results from CDMSlite run II (in red) as reported during the SuperCDMS collaboration meeting in Aug 2016.

Chapter 3

T_c Measurement at QTF

This chapter introduces the experimental setup, procedures, and results of the critical temperature (T_c) measurement done at QTF. The TES was discussed in section 2.4.4, where the change in the TES phase during regular detector operation, was a result of particle interaction which takes place inside the crystal. Hence, thermal energy is deposited into the crystal, and the W sensor changes from superconducting to normal state. However, in this measurement, thermal energy is fed by the mixing chamber heater.

In general, T_c measurement usually aims to confirm the reproducibility and to optimize the detector production as well as to make sure that W samples can be controlled to the desired critical temperature. So, the same measurement was conducted at different test facilities, and results were shared within the SuperCDMS collaboration.

3.1 Experimental setup

Figure 3.1 below shows two different sets of W samples glued on a copper plate inside a regular CDMS detector housing (1 cm thick). The samples labeled (1-4) at the top of figure 3.1 are connected to DIB-1 and they were fabricated at SLAC National Accelerator Laboratory. The second set of samples (5-8) are connected to DIB-2 and they came from Texas A&M University.

The transition temperatures obtained in this measurement were taken using two different types of thermometers; the first is a resistive thermometer (RT) which is permanently mounted at the mixing chamber plate of the cryostat.

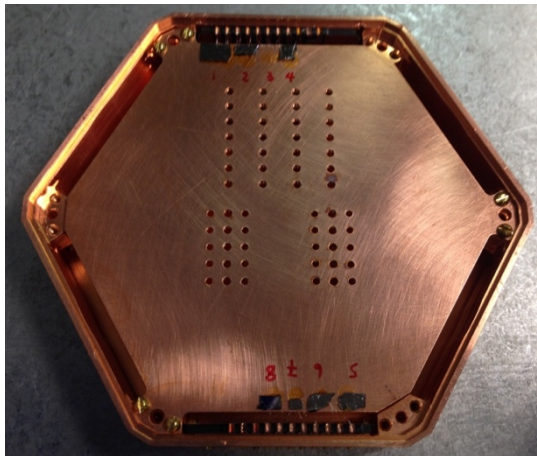


Figure 3.1: Eight Tc samples glued to a 1 cm thick detector housing (ZBT1-19).

The second thermometer is a Magnetic Field Fluctuation Thermometer (MFFT), usually referred to as noise thermometer. It is thermally connected directly to the detector housing, and it is able to measure between 1 *mK* and up to 1 *K* [55]. At the milli-Kelvin temperatures, it is

crucial to consider the self-heating to properly interpret the measurement. Unlike resistive thermometers, the noise thermometer is considered to have the most reliable measurement in this regard.

At cryogenic temperatures, thermal and electrical noise clearly affects the measurement [56]. To have an accurate measurement, we used high performance D-subminiature connector, a pi-filter type with 1000 pF capacitance. The filter shown in figure 3.2 [57], was attached to the E-box at room temperature. The main function of the filter is to attenuate undesired frequencies that could possibly be transmitted from room temperature electronics, such as the Detector Control and Readout Cards (DCRC, which represents the set of electronics at room temperature

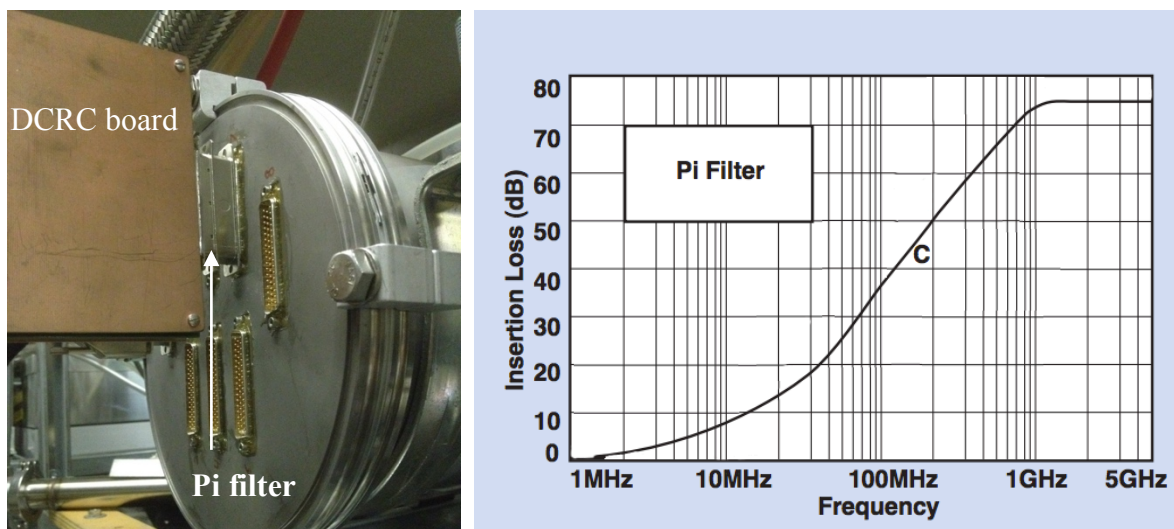


Figure 3.2: *Left panel:* The pi-filter connected between the E-box of the cryostat and the DCRC board. *Right panel:* The Insertion loss - curve corresponds to the utilized pi-filter. Pi filter insertion plot source [57].

used to control and readout phonon and charge channels of the SuperCDMS detector) to the cold electronics inside the cryostat. Hence, we can achieve a more accurate and reliable T_c

measurement. Based on tests done at UMN [58] and at QTF, it was confirmed that noise from room temperature electronics can be suppressed by $\sim 20\%$ using the pi filters.

3.2 Experimental method

The critical temperature measurement was conducted in two methods. The first method started by sending a test signal of 150 mVpp to the QET circuit (as shown in circuit diagram of figure 2.9). The test signal is basically a current, sent either to the feedback or to the QET within

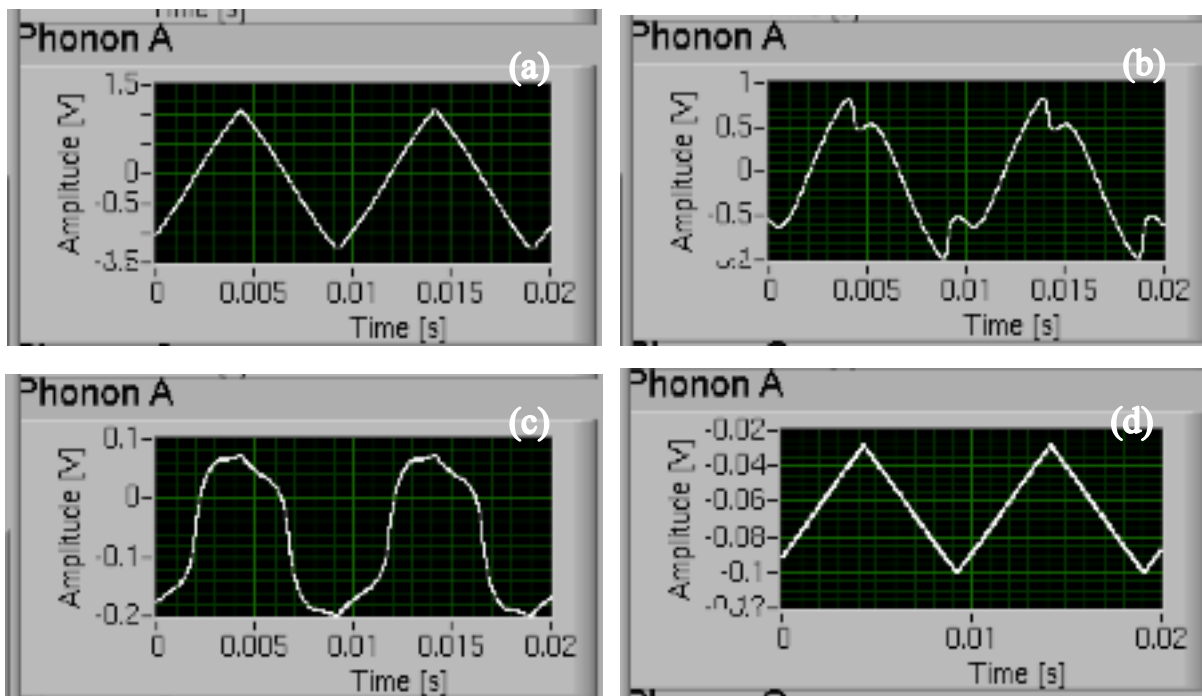


Figure 3.3: Screen shots for the detector readout, showing one of the phonon channels changing its state from superconducting to normal. (a) The test signal as it appears on the control readout while the sample is in superconducting state. (b) The amplitude starts to decrease at the beginning of transition. (c) at transition, when the superconducting slope almost disappeared. (d) while the sample is normal, the amplitude becomes too small and almost stops decreasing. Note the change of the scale on y-axis.

the phonon readout circuit. Once the signal is sent to the QET, the change (increase/ decrease) in

the TES resistance due to the heat flow from the mixing chamber heater, will affect the amplitude of the current in the input coil (will be decreased/ increased) which in turn changes the magnetic flux of the coil. Due to the coupling between input coil and the SQUID, the change in flux will cause a change in the voltage fed through the primary amplifier and finally that will change the current ($I_{feedback}$) flowing through the feedback circuit (figure 2.9 shows the readout circuit in details). The change in ($I_{feedback}$) is observed at the detector readout. Once the sample reaches the normal state, then a very small current will pass through the TES branch of the circuit (due to the large resistance value compared to the shunt resistance). Hence, no more change in the ($I_{feedback}$) current is possible.

Once the amplitude of the output signal starts to change (decrease), that is considered as the beginning of the transition from superconducting to the normal state; so the reading taken at this point was called “NT_start” referring to the noise thermometer reading. Then, at the moment the superconducting slope disappears, this represented the transition temperature, “NT_T_c”. Eventually, when the test signal’s amplitude stops changing, the recorded temperature was called “NT_end”. The recorded data is shown in the Table 1.

Each recorded measurement represents the average of ~10 data points, and the error in the values of this table represents the amplitude of the fluctuation from the mean value of the points.

Table 1: The data corresponds to SLAC T_c samples from run 65 at QTF.

Channel	NT_start [± 1 mK]	NT_T _c [± 1 mK]	NT_end [± 1 mK]
Sample [1]	35.3	37.0	38.1
Sample [2]	42.8	44.2	45.2
Sample [3]	48.3	48.5	48.9
Sample [4]	48.6	50.1	50.6

Table 2: The data corresponds to TAMU T_c samples from run 65 at QTF.

Channel	NT_start [± 1 mK]	NT_T _c [± 1 mK]	NT_end [± 1 mK]
Sample [5]	51.9	54.2	55.9
Sample [6]	55.8	57.3	57.9
Sample [7]	63.4	65.1	67.4
Sample [8]	55.9	56.2	51.7

The second method was conducted using a 4-wire. Then, by plotting the resistance-time curve for each sample, we determined the critical temperature values, then we could cross-check with results from the first method.

Figure 3.4 shows the change in resistance versus temperature for three of the samples fabricated in SLAC. From the plot, we can notice the sudden jump (sharp transition for samples 2 & 4) in resistance once the temperature of the sample exceeds its critical temperature, compared to the relatively wide transition for sample 1.

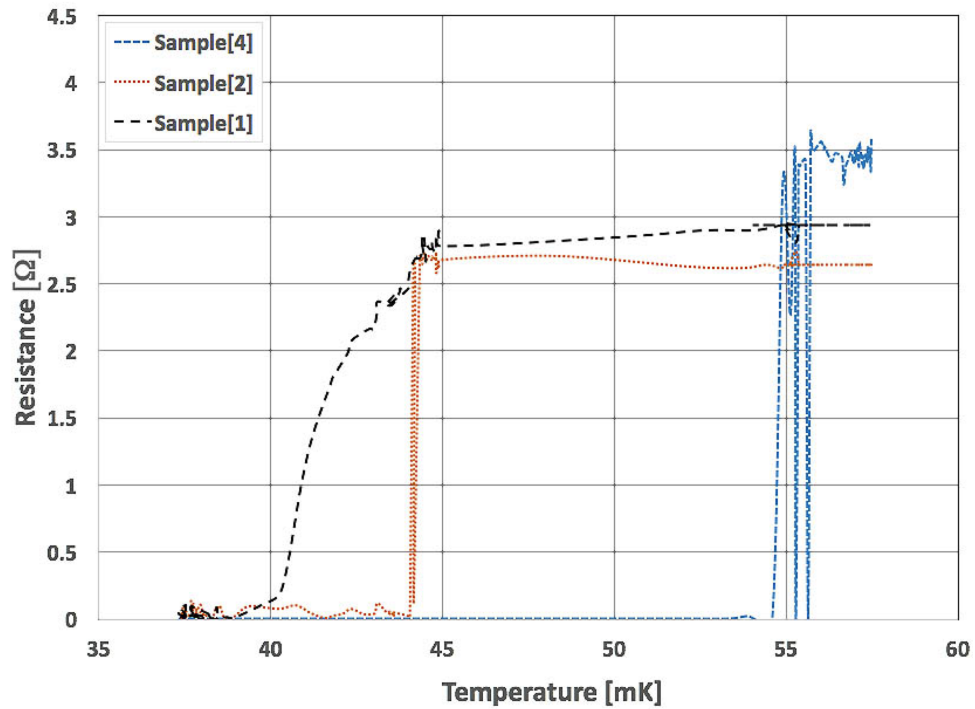


Figure 3.4: Resistance versus Temperature graph during a 4-wire measurement.

The data acquisition system at QTF takes a measurement (resistance and temperature) every few seconds (adjusted by user). To have the exact temperature measurement, an interpolation of the data was performed before being able to have the three samples at the same plot.

3.3 Comparison of Results

In this section, I present the results for the T_c measurement done at QTF and compare that to the results from SLAC. Initially, a T_c measurement was done at SLAC for the samples labeled (1 - 4) using dilution fridge (KO-15). Then a blind measurement was done for the same set of samples at QTF. After sharing the results with SuperCDMS group at SLAC, they confirmed that their measurement was off by ~ 19 mK.

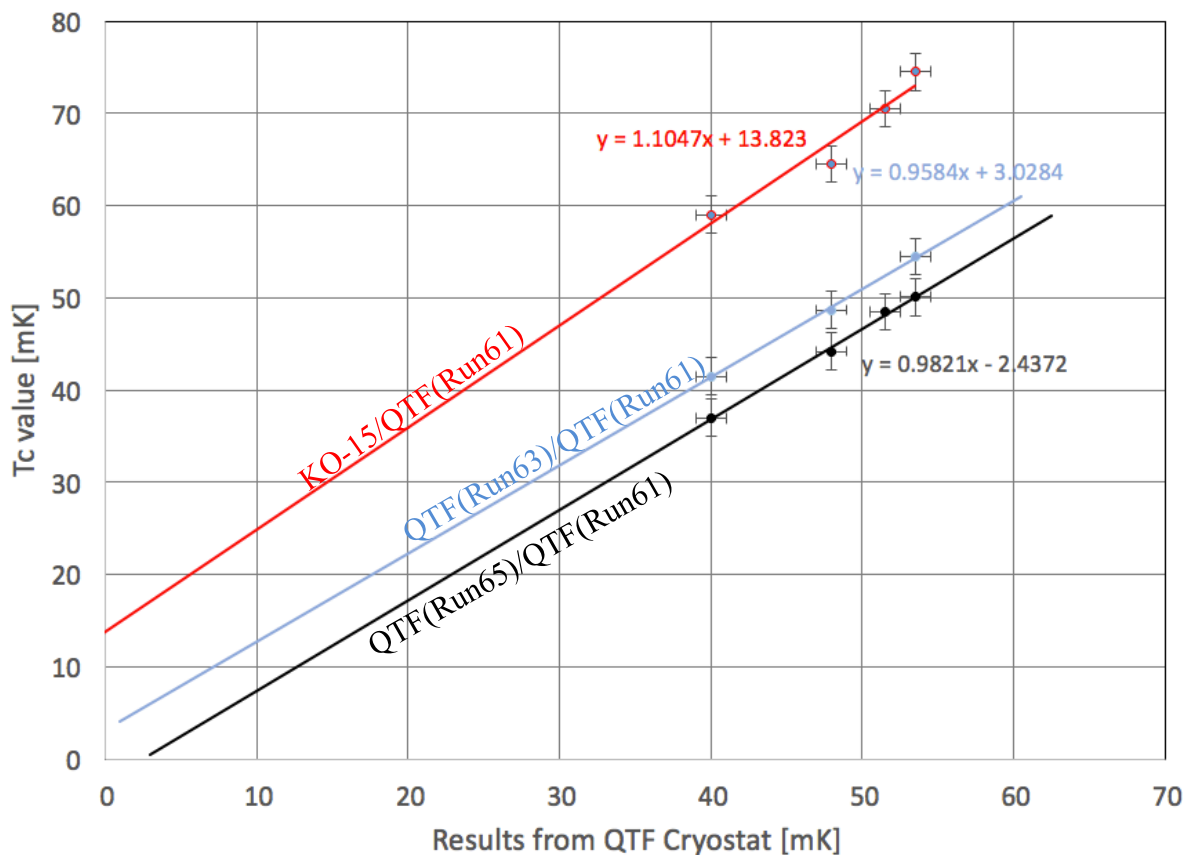


Figure 3.5: Comparison between the results from SLAC to that from QTF. *Red line* represents the data from SLAC with respect to run 61. *Black line* represents different runs at QTF. Ideally, the slope of the black line should be 1 and y-intercept at 0. *Blue line* represents the data from run 63 (4-wire measurement) relative to run 61.

Figure 3.5 summarizes the results from runs 61, 63 and 65 at QTF. Before conducting Run 61, we installed an optical fiber inside our cryostat, and we thought that it might be affecting the measurement, by sending some of the room temperature IR radiation down to the detector housing, which might be heating the fridge. So, from run 65 we had the optical fiber moved out of the detector housing and repeated the measurement from run 61. The uncertainty for the data at QTF is estimated, by taking the maximum deviation from the average of several data points. The temperature measurements in run 61 were performed using the noise thermometer, while run 63 represents the measurements done using the 4-wire measurement method. Run 65 was a repeat for the same technique in run 61. The slope of each fit in figure 3.5, should ideally be equal to 1, while the y-intercept represents the deviation from run 61. The numeric results of all runs in addition to the data from SLAC is shown in Table 3.

Table 3: The table includes the critical temperature measurements done at QTF and SLAC for detector housing (ZB1T-19).

<i>Facility</i> <i>Channel</i>	SLAC (KO-15) [± 2 mK]	QTF(Run61) [± 1 mK]	QTF(Run63) [± 1 mK]	QTF(Run65) [± 1 mK]
Sample [1]	59	40.0	41.5	37
Sample [2]	64.5	48.0	48.7	44.2
Sample [3]	70.5	51.5	N.A.	48.5
Sample [4]	74.5	53.5	54.5	50.1

The data from runs 63 and 65 confirmed our results in run 61, however, there is no obvious reason for the difference in the measurements between run 61 and 65 for the same sample. Then, a further test done to measure the transition temperature for the four samples fabricated at Texas A&M University (TAMU) was also done in run 65 and the results are reported in table 2.

3.4 Conclusion

T_c measurement is one of the fundamental tests in TES-based detectors. It is required to confirm the reproducibility and the optimization of the SuperCDMS detector production process [59]. The T_c measurement was conducted at QTF with two different methods. Although the measurement in run 61 was similar to that in run 65, but the results were off by ~ 3 mK. Moreover, the results we had at QTF were consistent with that from SLAC.

The consistency between the different measurements confirms the reproducibility of the samples under study as well as the consistency between SLAC and QTF experimental tools.

Chapter 4

Detector Breakdown-voltage Measurement

The breakdown voltage of a cryogenic detector in SuperCDMS experiment can be identified once the crystal becomes a partial conductor. Hence, a leakage current will pass through the crystal, and a clear sign of heat may be seen on the crystal's temperature. SuperCDMS detectors have shown inconsistent behavior when biased at high voltage during their operation at different test facilities and at SUL within the SuperCDMS collaboration. For instance, while the SUL was operational, detector T2Z1 used to run at -75 V bias voltage for few months, then it was operated in iZIP mode with $\pm 4\text{ V}$ for some time. Afterward, no more than -25 V was possible. After receiving tower two (T2) at QTF, and attempting to test the same detector one more time, we were able to apply a bias voltage of more than -100 V . This chapter focuses of the tests done at QTF to validate whether the breakdown voltage is test facility dependent or not, to determine whether it is a polarity dependent, and to measure the G16K breakdown voltage, a detector arrived to QTF in the year 2012 after being rejected for SUL due to its low breakdown voltage.

4.1 Experimental setup

To be able to apply a high voltage across our hiZIP detector (G16K), we had to make some modifications to the readout circuit to avoid any possible damage caused by high voltage. Considering the specifications and charge channel layout of the G16K detector (discussed in

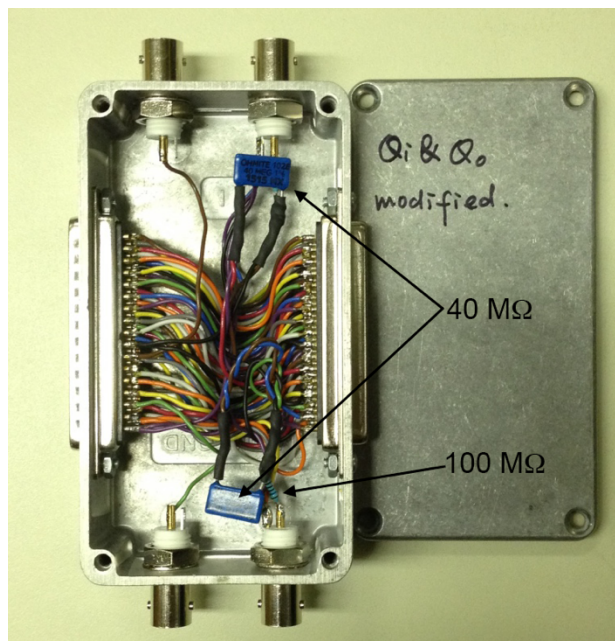


Figure 4.1: External modification box for the charge channels, (the box was modified by Xiaohe Zhang).

details in section 5.2.3 of this thesis in addition to resources [60, 61]). We designed an external connection box, shown in figure 4.1, which can be plugged into the 50-pin connector at cryostat E-box (at room temperature); to protect the charge readout channels on the side coax level from any possible damage while applying high voltage.

The rationale behind the addition of those resistors can be understood once we examine the charge circuit diagram in figure 4.2. Four lines were connected; (feedback, bias, source and

drain) inside the connection box, and a $40\text{ M}\Omega$ resistor was added inline with the source and drain. That is to have a $40\text{ M}\Omega$ resistance on each of the three branches.

Then, we connected the return lines of the channel, feedback, source, drain and bias all together to another $100\text{ M}\Omega$ resistor, to minimize any current that might be passing through the circuit and damaging the coupling capacitors. Then the output was connected to a BNC connector as shown in figure 4.2 [62]. The same configuration was applied to three charge channels; Q_p , Q_{inner} and Q_{outer} located on side 1 of the detector. The other side of the detector contained the four phonon channels and the charge channel Q_2 were grounded during the measurement.

During this measurement, we were able to record data out of two phonon channels rather than four. That is due to the failure of one of the Detector Control and Readout Cards (DCRC) which represents the set of electronics at room temperature used to control and readout phonon and charge channels of the SuperCDMS detector.

To calibrate the phonon signal, two ^{241}Am (gamma source) were used; one shining on side 2 close to phonon sensor (C) and the other is shining on side 1 at phonon channel (D). From previous runs using detector G16K, we can clearly see the 60 keV peak resulting from this source, so, by having a bias voltage across the detector, it is expected to be able to measure amplification as a result of bulk events from the gamma source.

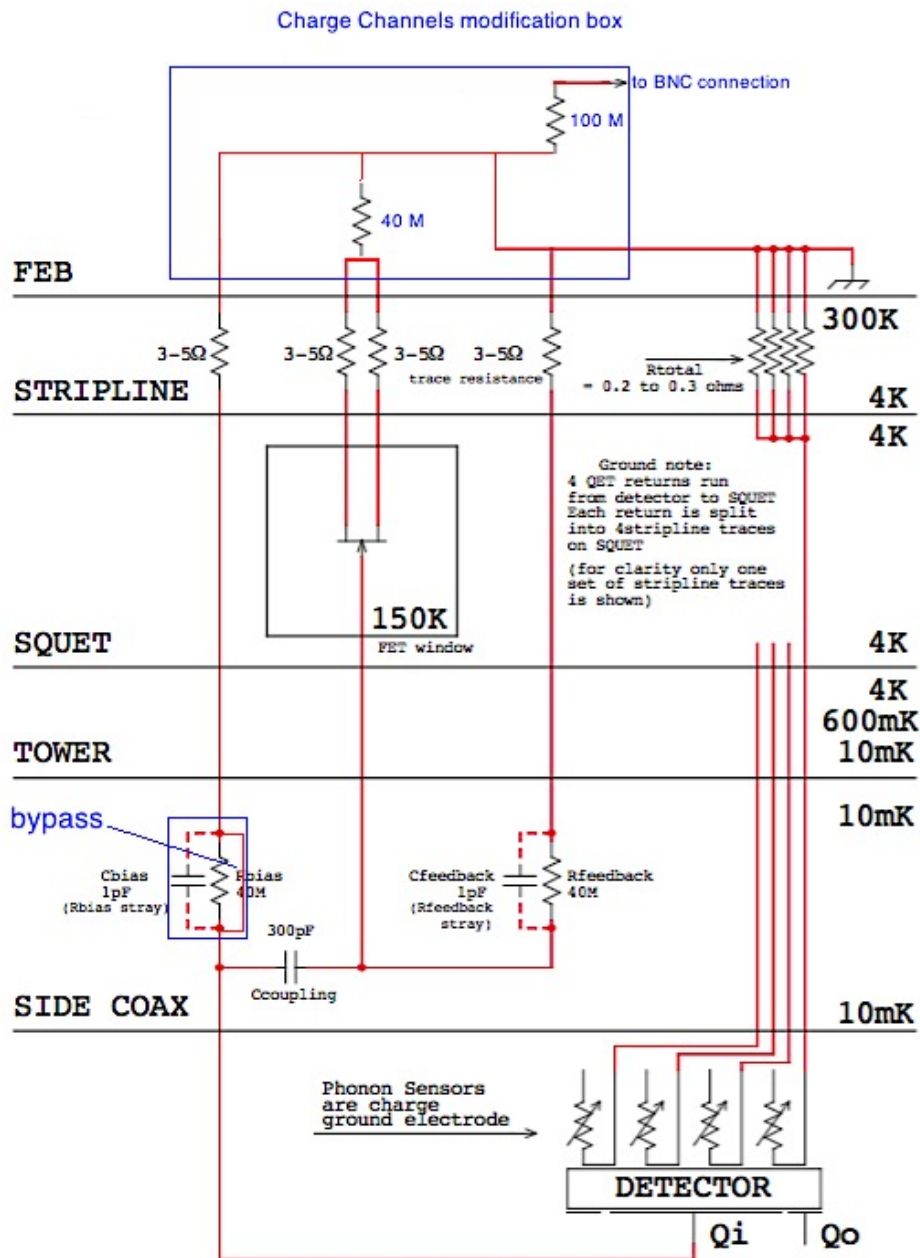


Figure 4.2: Circuit diagram of the charge readout channel, showing the modifications required for high voltage test (in blue). The bypass for the bias resistor was done for different purpose in older run and has nothing to do with the high voltage measurement. This would have been an issue if something went wrong during this test.

4.2 HV Technique and results

The measurement started without applying a bias voltage to calibrate the energy scale to the 60 keV peak from the ^{241}Am source. After calibrating the energy scale, we started by applying a bias voltage and looked for the amplified phonon signal, as shown in figure 4.3. At the end of each data set, the detector was flashed for ~ 15 seconds to free any trapped charges and reset the status of the detector. For flashing the detector, we used the internal LEDs mounted on each DIB. And for the bias voltage, it was applied on side 1 of the detector through the charge channels Q_p , Q_{inner} and Q_{outer} , while side 2 was always at ground (more details about the detector configuration are discussed in section 5.2.3).

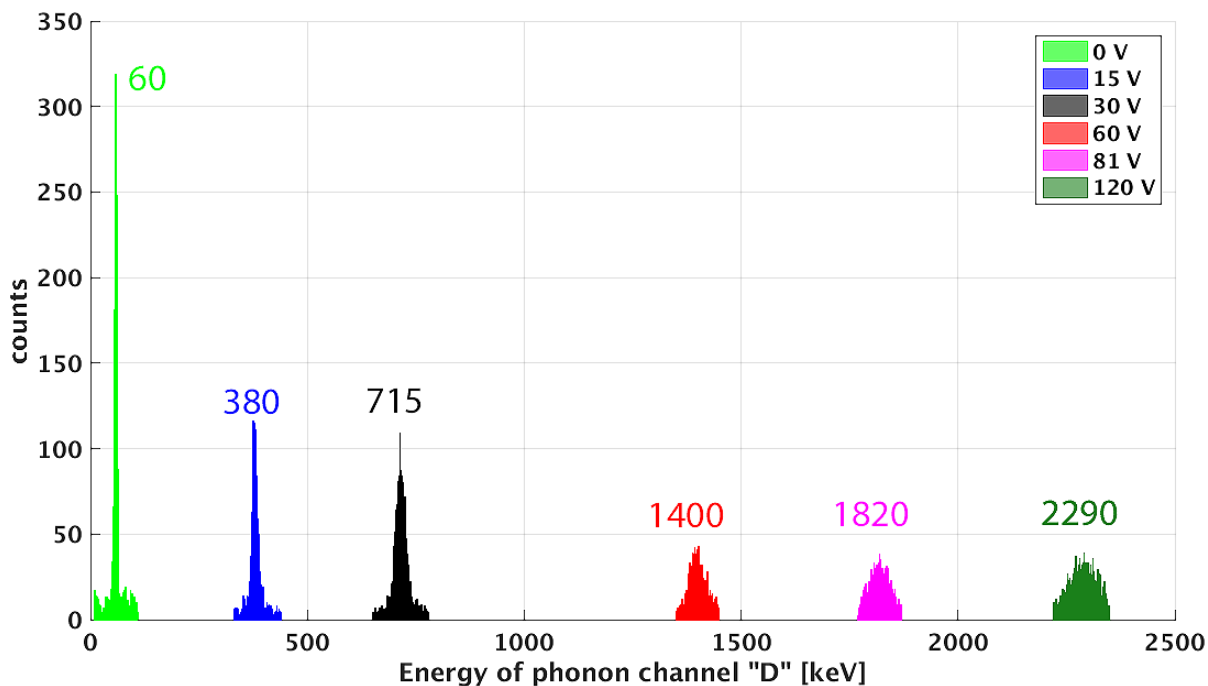


Figure 4.3: Energy of phonon channel D calibrated to ^{241}Am source at different positive bias voltages. The error in the above measured quantities is ± 5 keV.

The energy spectrum shown in figure 4.3 depicts the shift in the ^{241}Am peak when the voltage changes. Initially, at zero volt, it is expected to have a 60 keV photons emitted from ^{241}Am . At this point, all the energy used to produce e^-/h^+ pairs ($E_{production}$) will be recovered as heat into the phonon sensors (E_{total}) since the charge carriers recombine.

$$E_{total} = E(\text{of incident particle}) \quad (4.1)$$

Afterward, a static electric field is generated by applying a bias voltage across the crystal. So, e^-/h^+ pairs start to drift from the bulk of the crystal towards the electrodes. While drifting, they produce more phonons causing an increase in thermal signal collected at the phonon sensors – assuming no or limited e^-/h^+ pair recombination. The generated signal is directly proportional to the bias voltage V_{bias} , and N_i , the number of e^-/h^+ pairs from the primary interaction. The total phonon signal energy E_{total} , will be equivalent to the incident particle's energy after taking away the energy lost during the interaction, then, by adding the Neganov-Luke deposited energy E_{Luke} we should get:

$$E_{total} = E - E_{production} + E_{Luke} \quad (4.2)$$

The energy from Neganov-Luke phonons is $E_{Luke} = N_i e V_{bias}$, where e is the elementary charge, and V_b is the potential difference across the crystal and N_i is number of e^-/h^+ pairs.

Knowing that:

$$N_i = \frac{E}{\varepsilon} \quad (4.3)$$

where ε is the average energy per e^-/h^+ pair. Then, using equation 4.3, we can rewrite equation 4.2 as

$$E_{total} = E - N_i \delta + N_i \times e \times V_{bias}$$

$$E_{total} = E \left(1 - \frac{\delta}{\varepsilon} + \frac{eV_{bias}}{\varepsilon} \right) \quad (4.4)$$

which gives the total phonon energy as a function of the bandgap energy of germanium ($\delta \approx 0.74 \text{ eV}$) [63] and V_{bias} is the potential difference across the crystal. Eventually, all the energy used to produce e^- / h^+ pairs will also be dissipated into the crystal and will be collected through the phonon sensors [45]. So, we can simplify equation 4.4 to:

$$E_{total} = E \left(1 + \frac{eV_{bias}}{\varepsilon} \right) \quad (4.5)$$

Based on the equations above, we can calculate for a given gamma energy the total energy expected to be measured with the phonon sensors of the detector and then compare this to the measured values. Assuming that the temperature remains the same during the run, all variables remain constant except for the bias voltage.

The ^{241}Am source produces both, bulk and surface events. Events occurring within the surface field (less than 2 mm from surface) are called surface events, while deeper events are the bulk (will have full Luke amplification) and the expected amplification should be related to the total voltage difference across the detector, as depicted in figure 4.3.

Figure 4.4 depicts the expected amplified signal (black line) and the measured signal for both, positive (red points) and negative (blue points) polarities. The expected value for the line in red, is based on equation 4.4 taking into account that $E = 60 \text{ keV}$ at 0 V . For lower voltages, the expected signal from Luke amplification is very close to measured one. However, at high voltage it seems we have less phonon signal that what was expected. We can also note that the signal amplification is polarity independent.

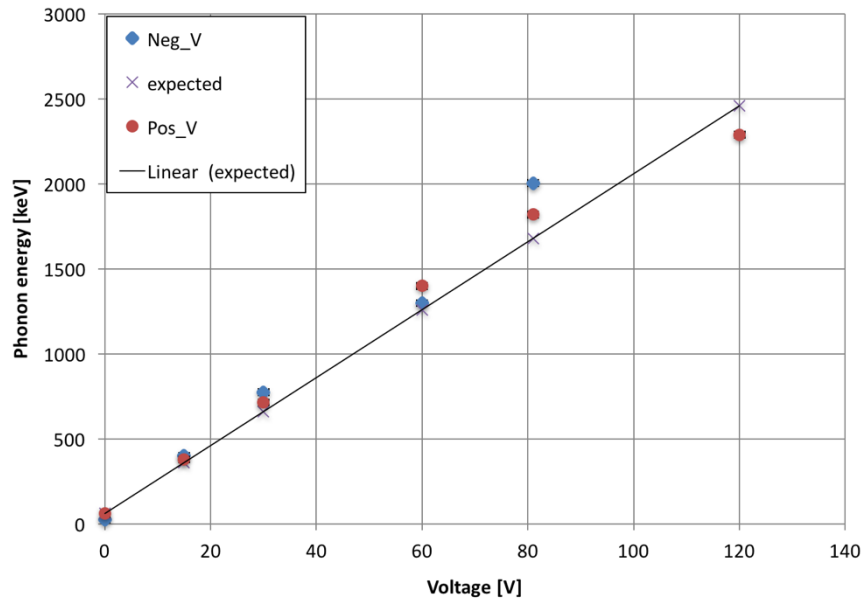


Figure 4.4: Total phonon energy versus bias voltage at positive (red) and negative (blue) polarities. Error bars are too small to be seen.

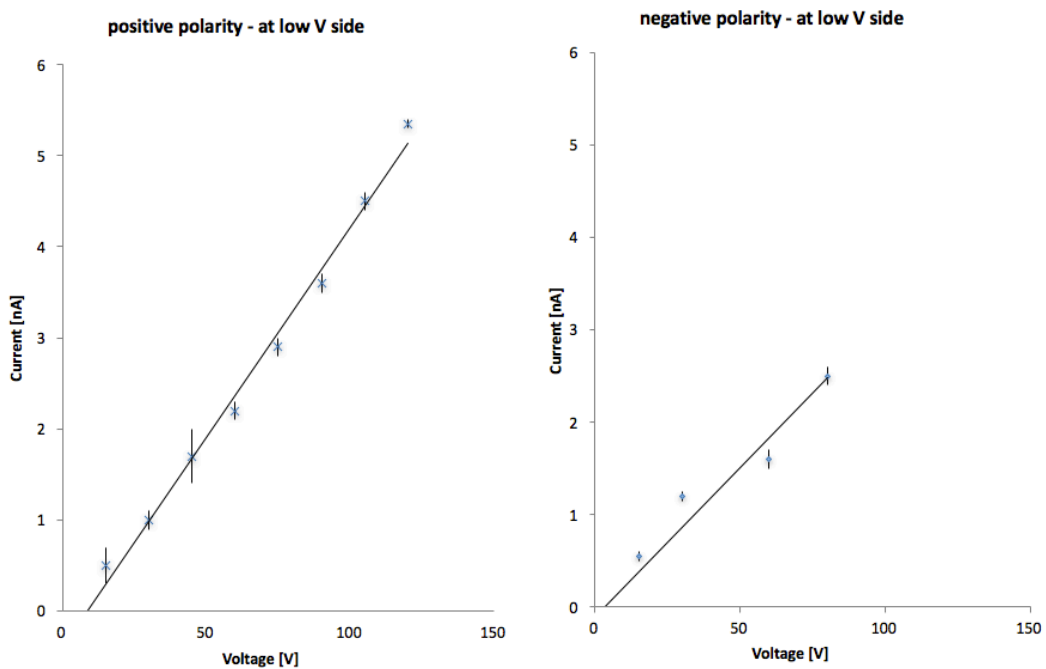


Figure 4.5: Leakage current during the measurement is extremely small, and could not have an effect on the applied voltage. Vertical error bars represent the standard error for the measurement.

The average power spectral density (PSD) for phonon channel (B) is plotted in the frequency domain, as shown in figure 4.6. The noise PSD is a tool used to monitor the data in terms of electrical and thermal noise. So, the rise of baseline is a direct a direct measure of the increase in noise at low frequencies which results in reducing the signal to noise ratio. According to the breakdown test for the G16K detector, phonon channels B and D we were able to tolerate approximately -84 V before a leak current managed to heat the detector a few hundred milli-Kelvin.

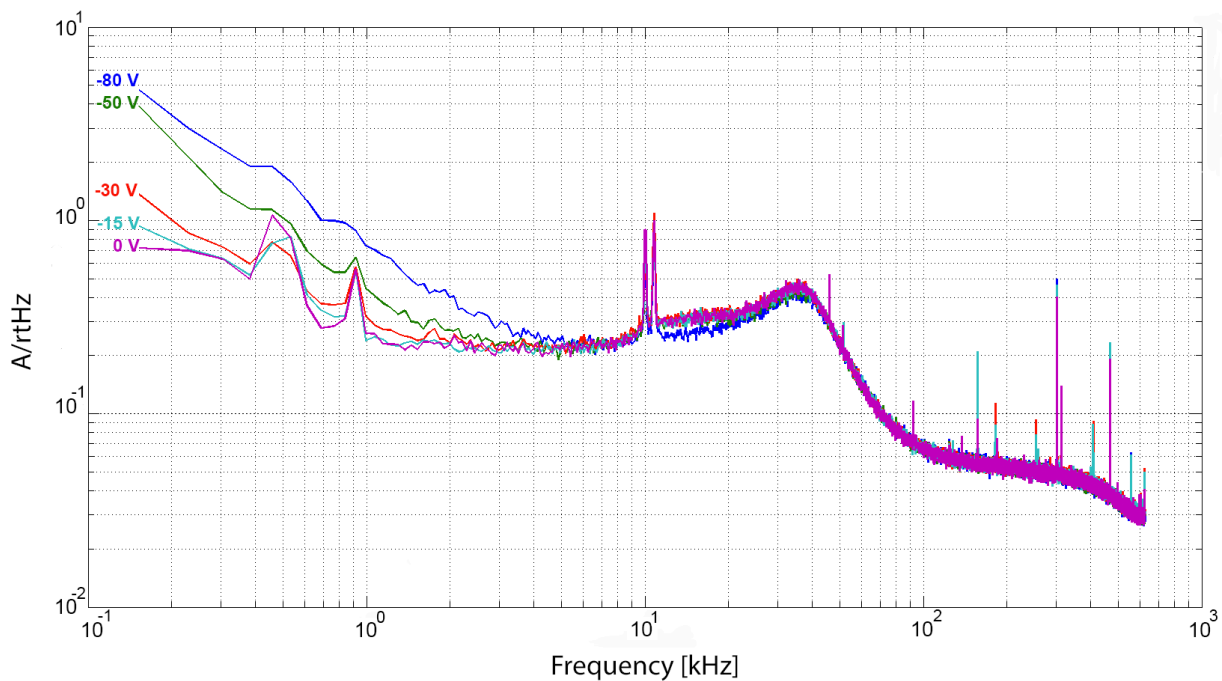


Figure 4.6: The noise power spectral density in phonon sensor B at negative bias voltages.

Figure 4.7 depicts the average PSD for phonon channel (B) at different positive bias voltages. The detector remarkably could stand a bias of 120 V , maximum voltage in this case was limited by the used power supply. In contrast to other detectors in different test facilities where the

breakdown happens much earlier in positive polarity. However, no breakdown was noticed up to + 120 V for two different detectors G16K and T2Z. And by comparing figures 4.6 and 4.7, we can notice that the noise is polarity independent, since it increases similarly in both polarities.

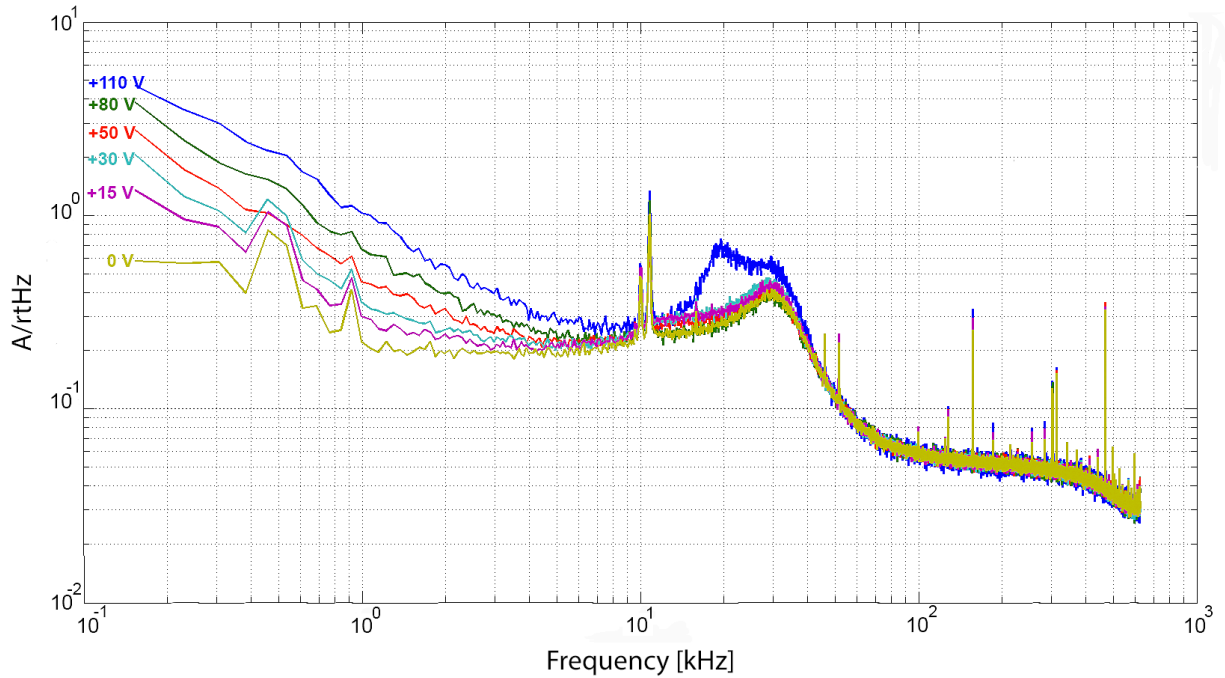


Figure 4.7: The noise power spectral density in phonon sensor B at positive bias voltages

Figure 4.8 depicts the increase in noise with voltage in both polarities. We can notice that the noise in positive polarity increases almost linear with voltage. But it is also very clear that the noise is polarity independent.

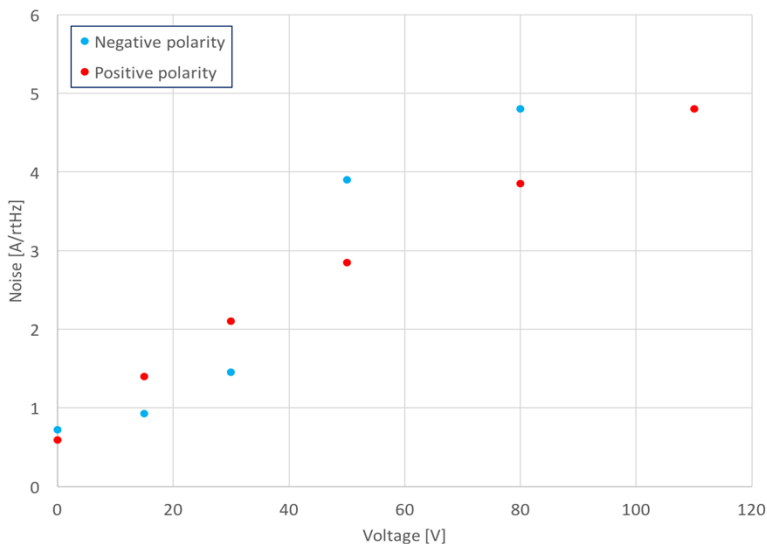


Figure 4.8: The noise in the phonon signal as a function of biasvoltage in positive and negative polarities.

4.3 Conclusion

We observed different breakdown voltages at different test facilities [64], and sometimes at the same facility at different times, similar to detector T2Z1 in SUL. On the other hand, the breakdown voltage measurements done at QTF showed some consistency and from the tests done on T2Z1, it showed clearly a higher breakdown voltage (at positive polarity) at QTF than other facilities.

At the end of the test using G16K detector, it was concluded that the breakdown voltage is not only detector-dependent but also a site-dependent. It is worth noting at this point, that the fridge at QTF is the only dry fridge, thus the only one that does not use exchange gas which might have an impact on the detector's behavior. Further tests are required to validate or reject this hypothesis (e.g. introducing small amounts of He gas into the dry fridge and study the detector response).

Chapter 5

IR Photon Calibration Measurement

5.1 Charge propagation

Once an interaction takes place in a detector's crystal, if enough energy is deposited, then e^-/h^+ will be created and start to drift to either side across the detector, then, eventually will be collected at the two-biased surface of the detector. During the drifting process, some charges might be trapped in the crystal impurities, while others might recombine. And of course, some will make it through the crystal to the charge electrodes at the surface. Consequently, there will be a discrepancy between the number of initially created charges and the number of charges collected at the electrodes.

In germanium detector, if the energy expended per e^-/h^+ pair is represented by ϵ , and the number of generated e^-/h^+ pairs is N_i , then the charge collected Q_c can be represented by:

$$Q_c = aeN_i = ae\frac{E}{\epsilon} \quad (5.1)$$

where E is the energy deposited by the interaction, a is the charge collection efficiency and e is the electron charge [45].

A study of the electron and hole propagation in germanium at the milli-Kelvin temperature and low electric field ($\approx 5 \text{ V/cm}$), showed an oblique electron propagation, as depicted in figure 5.1, compared to a straight propagation for holes, at the same conditions [65].

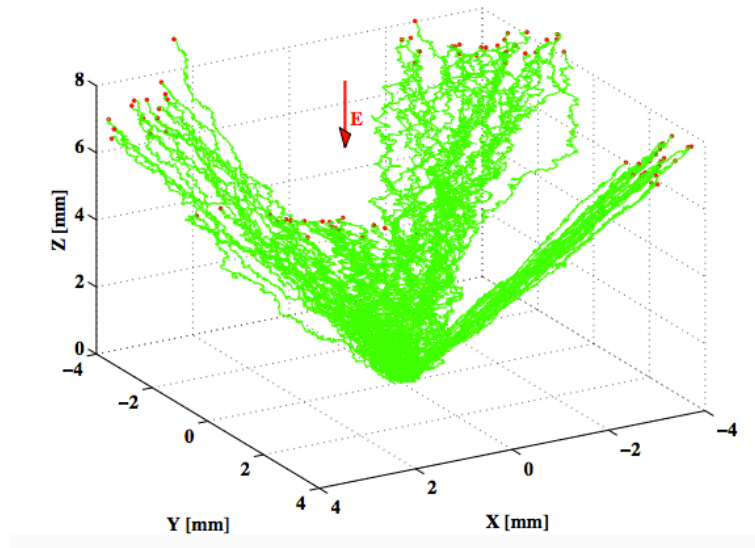
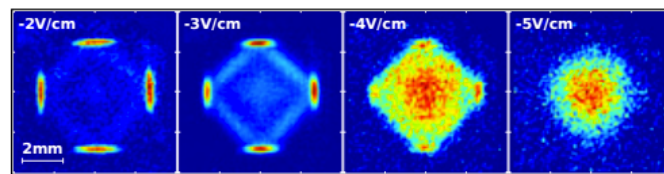
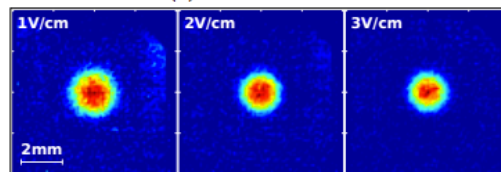


Figure 5.1: Oblique electron propagation in germanium crystal at the milli-Kelvin temperature, and low electric field. Image from [65].

The electron separation into four groups indicates the electron mass anisotropy in weak electric fields. Each one of the groups corresponds to a minimum in the conduction band for germanium. At higher electric fields, the inter-valley scattering increases, which makes the electrons effectively go more along the electric field lines, so, density pattern (representing the electron propagation) starts to behave as a Gaussian distribution – as shown in figure 5.2 [66].



(a) Electron Data



(b) Hole Data

Figure 5.2: Two-dimensional pattern of (a) electrons and (b) holes drifting to a non-illuminated face of the germanium sample. At low electric field (less than 5V/cm), the electrons propagate into four regions corresponding to four minima in the conduction band. Image from [66].

The data in figure 5.2 corresponds to a measurement done in a germanium sample of thickness 3.89 mm to image the oblique propagation of electrons at low electric field and low temperature (sub-Kelvin) [66]. The oblique propagation is prominent for electric fields up to about 4 V/cm which corresponds to a total bias voltage of ~ 13 V for the 25 mm thick detector used in the measurements of this chapter.

5.2 Experimental setup

The basic idea of the setup is to inject IR photons down to the milli-Kelvin stage onto the detector's surface out of LEDs at room temperature, using a multimode fiber optic cable. The LEDs were used at room temperature rather than at low temperature because it is difficult to control LEDs at low temperature at the level we anticipate. Moreover, we do not have to worry about direct heating effects from operating the LEDs.

The dry dilution refrigerator at QTF was not equipped with the required apparatus to conduct the IR calibration measurement. Hence, some of the experimental setup were purchased, while others were custom-made parts, designed and manufactured in the department's workshop.

5.2.1 Multimode fiber optic cable

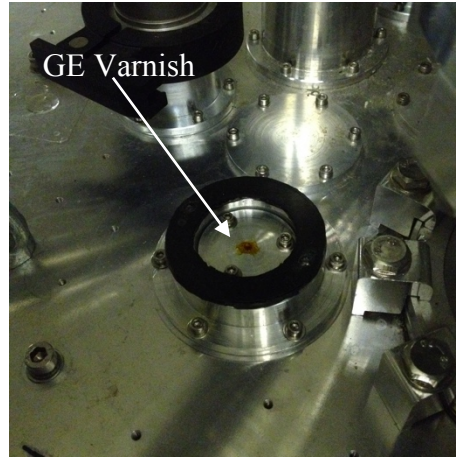
The fiber optic cable used in this measurement was provided from Looock Laser Laboratory in the department of Chemistry at Queen's University. The fiber has a pure silica core, $400\ \mu\text{m}$ in diameter, and more than 99% transmission per kilometer length at the selected LED wavelengths (890 nm and 1550 nm). This ensures that most of the photons emitted from LED and entering one end of the fiber, may reach the detector surface. Moreover, fiber optic cable has a high attenuation at longer wavelengths [67], which reduces the possible transmission of room temperature blackbody radiation into the fridge.

In order to avoid a substantial amount of room temperature blackbody radiation from being coupled into the fridge, two identical fiber optic cables were deployed. One end of the fiber optic cable was attached to the vacuum feedthrough at room temperature, while the other end was coupled to the still plate, separated by $\sim 0.5\ \text{mm}$ from the other identical multimode fiber cable,

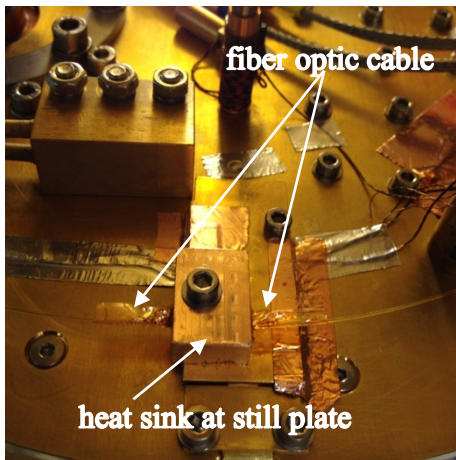
which is also coupled at the still plate and going down to the detector housing – as shown in figure 5.3. The use of two fiber pieces aimed also to decrease the transmission of the room temperature radiation through the fiber.



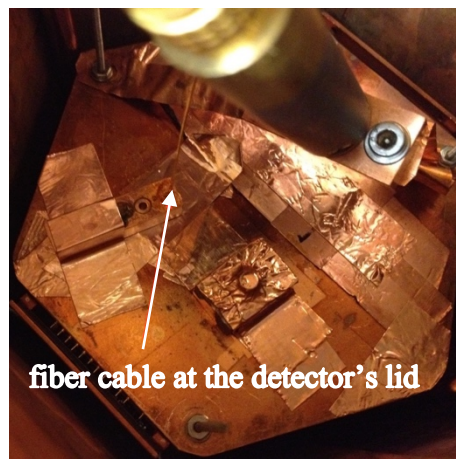
a. A custom-made vacuum feedthrough for the fiber optic cable, before assembly.



b. Glue was applied to seal the vacuum feedthrough and to firmly hold the fiber cable at the cryostat's top flange.



d. Heat sink attached to the still plate (~800 mK) to couple the optical fiber.



c. The fiber cable is attached to a copper holder and shining at phonon channels B & D.

Figure 5.3: The installation of fiber cable at QTF.

5.2.2 Light Emitting Diodes (LEDs)

The selection of each LED's wavelength is based on the germanium bandgaps. So, the plan is to have one LED emitting photons with energy above the direct bandgap (890 nm), while the other LED is emitting photons with energy in-between the direct and indirect bandgaps (1550 nm). The variation of the bandgap depends solely on the temperature. Experimental methods have determined the following equation

$$E_g(T) = E_g(0) - \frac{\alpha T^2}{(T + \beta)} \quad (5.2)$$

where $E_g(0) = 0.7437 \text{ eV}$ is the germanium indirect bandgap at 0 K , $\alpha = 4.77 \times 10^{-4} \text{ eV/K}$ and $\beta = 235 \text{ K}$, α and β are experimental fitting parameters. Figure 5.4 below, depicts the direct and indirect band gaps of germanium at room temperature, where the conduction band has a number of sub bands and the bottom of the conduction band is located along the $\langle 111 \rangle$ axis [68, 69].

Considering the operating temperature at QTF (45 mK), and using equation 5.2 we can calculate the band gap in germanium to be 0.743 eV . Then using $\lambda_{\text{indirect}} = \frac{hc}{E_{\text{indirect}}}$ we can calculate the

corresponding wavelength for the indirect band gap of germanium to be 1670 nm . Where h is Plank's constant, and c is the speed of light. Hence, the corresponding wavelength for the direct bandgap

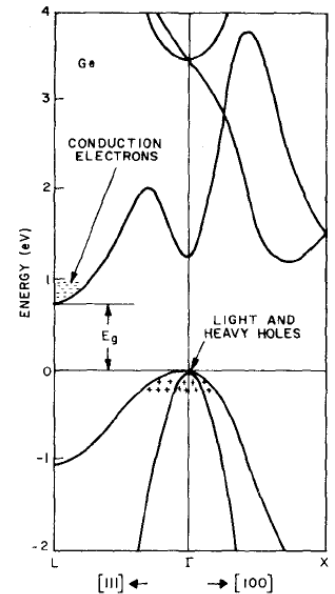


Figure 5.4: Energy band gap at room temperature for germanium. Image source [68].

is 1517 *nm*.

The Surface Mount Devices (SMD) used, consists of an InGaAsP LED mounted on ceramic and sealed with silicon. Both LEDs were soldered to an electronic chipboard [70]. The chipboard is glued to a custom-made aluminum cover for the fiber optic cable vacuum feedthrough, as shown in figure 5.5. In order to be able to emit a controlled number of photons (as few as possible), a special wiring was prepared to operate the LED from the DCRC boards using the LED driver. Hence, the intensity, frequency and flashing time were under control using the detector control.

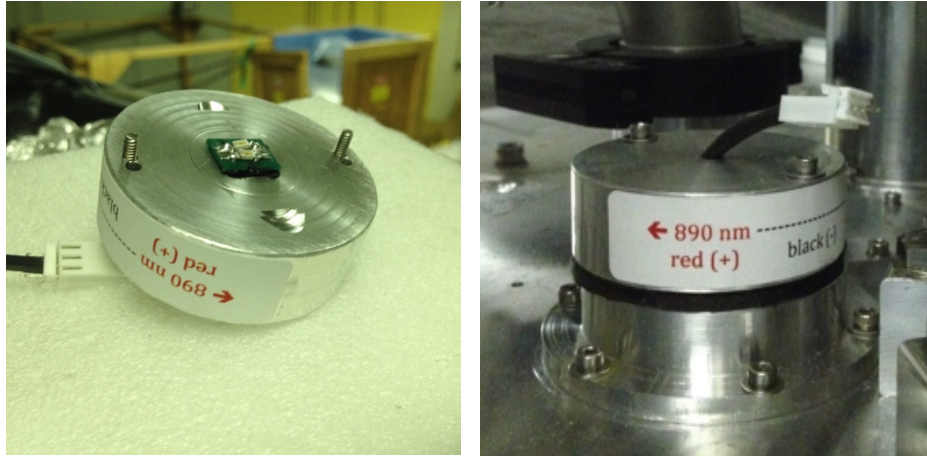


Figure 5.5: *Left panel:* Vacuum feedthrough cover to hold the external IR LEDs. *Right panel:* The cover while mounted at the top of a black rubber to block the ambient visible light radiation from reaching the fiber cable. The LEDs can be swapped mechanically by changing screw location of the top cover.

The average distance traveled by the IR photons through the germanium detector before being absorbed, is inversely proportional to the absorption coefficient (α). Since α depends on the wavelength as well as on temperature, no values were reported in literature to indicate the penetration depth in germanium at temperatures lower than 4.2 K, as depicted in figure 5.6 [71].

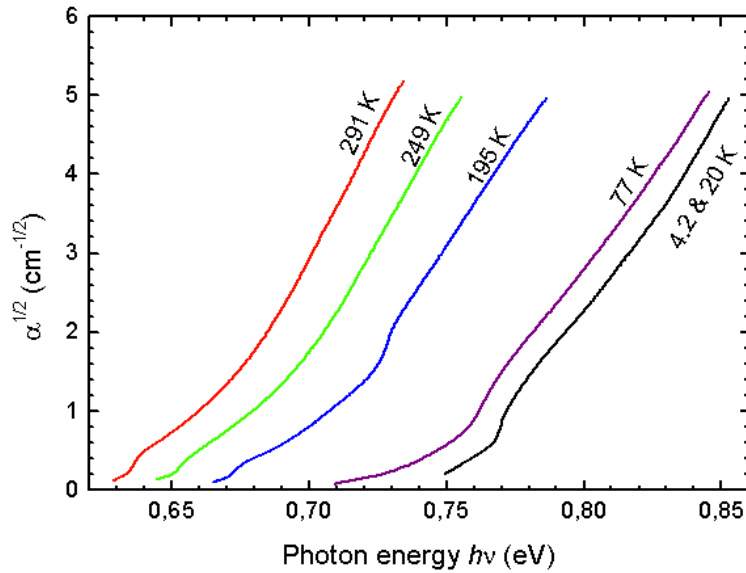


Figure 5.6: The absorption coefficient dependence on both, temperature and photon's wavelength. Image from [71].

5.2.3 G16K – hiZIP Detector configuration

The G16K detector used during the measurement is a hiZIP detector, which consists of four phonon channels on one side labeled as side 2. The two charge channels on side 2 (Q_{inner} and Q_{outer}) are connected together, called Q_2 and read through Q_{inner} on side 2. While the other four phonon channels on side 1 are, wire bonded together and used as a charge read out channel called Q_p read through Q_{outer} on side 1. Then, Q_{inner} on side 1 is kept without modification, while Q_{outer} on the same side is read through Q_{outer} on side 2, as shown in figure 5.7.

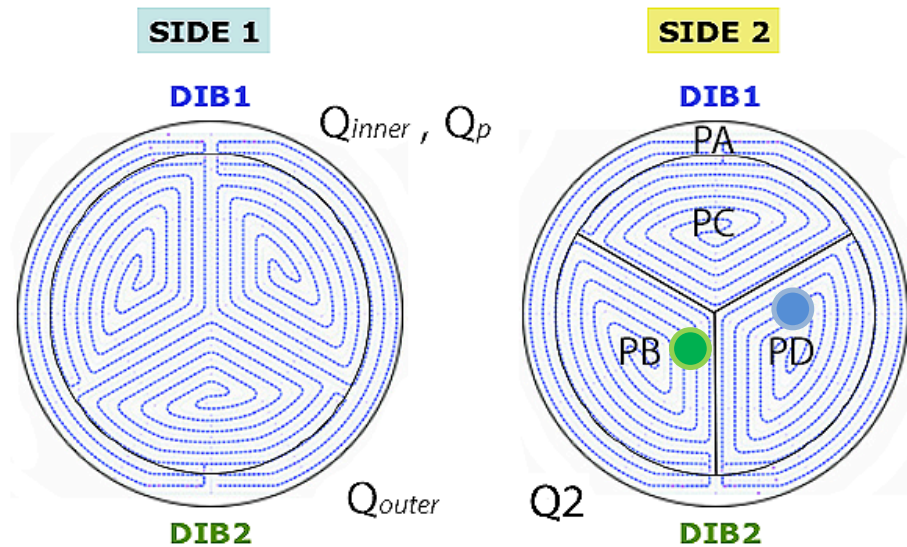


Figure 5.7: G16K – wiring diagram. The blue circle represents the position of the ^{241}Am source and the green circle represents the position of the fiber cable relative to the detector surface.

At the beginning of the run, it was noticed that the amplitude of Q_{inner} and Q_{outer} on side 1 is very low compared to the usual charge channel signal, and diagnosed to have a flaky connection – possibly between the charge channel and the DIB. So, the two channels were grounded.

In order to have an electric field as uniform as possible inside the crystal, the bias voltage was applied to Q_p on side 1 and Q_2 on side 2. While Q_{inner} and Q_{outer} on side 1 were grounded during all tests.

5.2 4 Detector's electric field configuration

In order to magnify the phonon signal resulting from both, bulk and surface interactions, we needed to bias the detector to a high voltage (up to 24 V across the detector which is equivalent to ~ 10 V/cm). Since the energy resolution of the G16K detector is about 1 keV, then the higher the bias voltage is, the lower interaction energy we can measure due to signal amplification. The data collected during the IR photon calibration measurement can be categorized into two groups based on the electric field configuration during the run. The first configuration uses the charge channels Q_2 (representing Q_{inner} plus Q_{outer} on side 2) and Q_p (representing all phonon channels on side 1), we called this configuration “iZIP field”, as shown in figure 5.8 [43] where the interleaved phonon and charge channels on the same side, which is similar to side 2 in the G16K detector at QTF. Different polarities and bias voltages were applied to each electrode during the test.

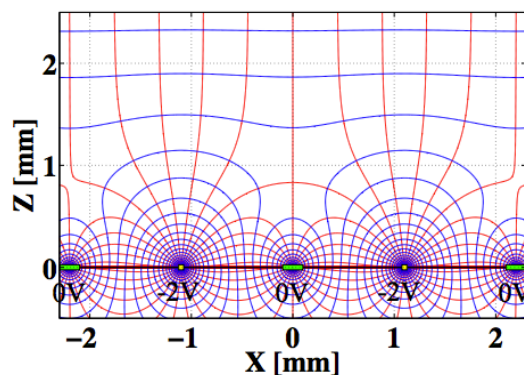


Figure 5.8: The e-field configuration for the iZIP detector. The grounded electrodes are the phonon channels, while the biased are the charge. Image from [43].

The second configuration, where side 2 was at ground (Q_2 in addition to the phonon sensors – of course), while bias voltage was applied to only Q_P (Q_{inner} , Q_{outer} were grounded on side 1), and we called this “flat field”.

5.2.4 Calibration source

In order to calibrate the energy of the emitted IR photons, a reference calibration source is needed. So, we installed $^{241}_{95}\text{Am}$ source inside the cryostat, at the detector housing. The Am source is considered to be a practical option because of the long half-life time ($\tau_{1/2} = 432.2 \text{ years}$) and it decays into Neptunium – 237 through which a low energy ($\sim 60 \text{ keV}$) gamma ray is radiated as a by-product. The decay equation can be represented by:



For the purpose of this experiment, we blocked α particles from reaching the detector. And the 60 keV - shown in figure 5.9, was used to calibrate the energy of IR photons at zero bias voltage.

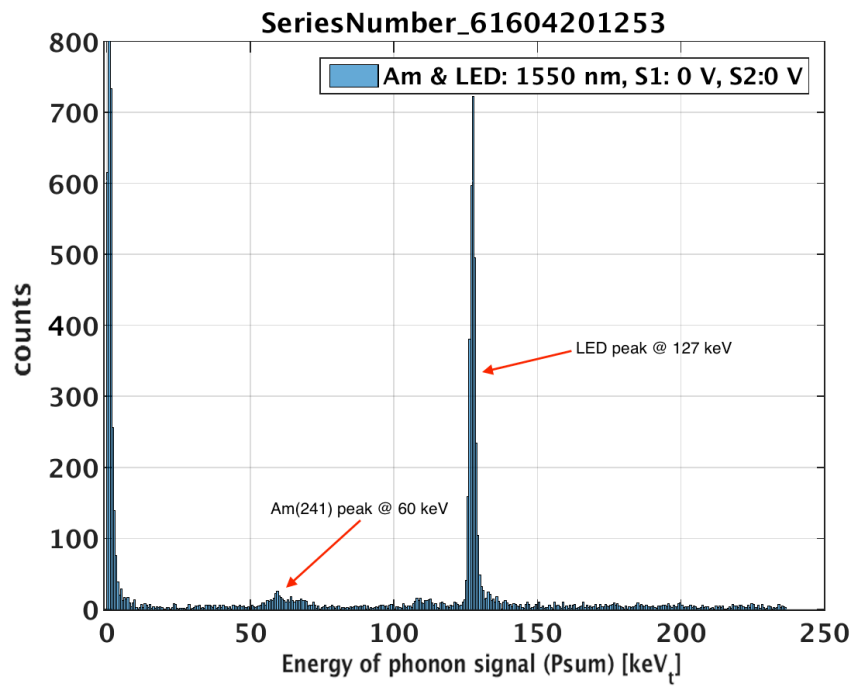


Figure 5.9: The use of Am-241 source to calibrate the energy scale of the 1550 nm LED at zero bias voltage. The x-axis represents the energy sum of the calibrated phonon channels.

5.3 Experimental Techniques

Since this is considered to be the first test to use IR LEDs at QTF, the ability to trigger on LED events was not confirmed. So, the procedure started by tuning the LED pulses on the detector control, then viewing those pulses at the detector readout. Once the LED pulses can be seen at the detector readout window, we started tuning the different LED parameters (current, pulse time and frequency) on the detector control. The aim at this stage is to minimize the LED current and the flashing time. Hence, minimizing the number of emitted photons.

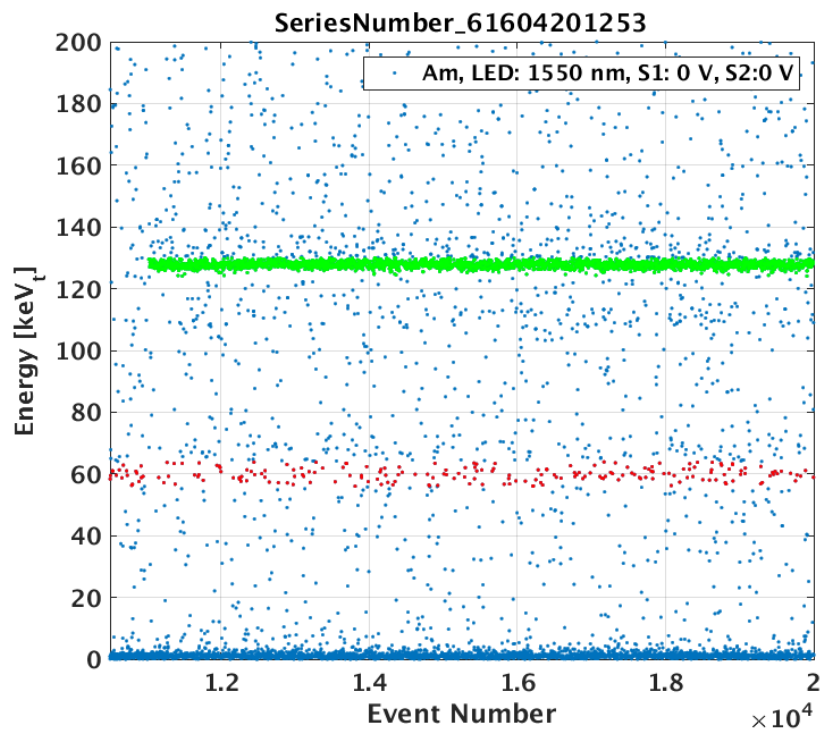


Figure 5.10: LED events can be identified (in green) after tuning the LED settings. In this plot, the 1550 nm LED was turned on after $\sim 1\text{k}$ events. The events in red are the 60 keV line from ^{241}Am source.

In order to have a rough idea about the spread of IR photons at the surface of the detector and to know the position where they will be striking the detector's surface, the x - y partition plot, shown in figure 5.11, represents one of the good tools we used for this purpose. The parameters used to calculate the x and y components are expressed in equations 5.7 and 5.8.

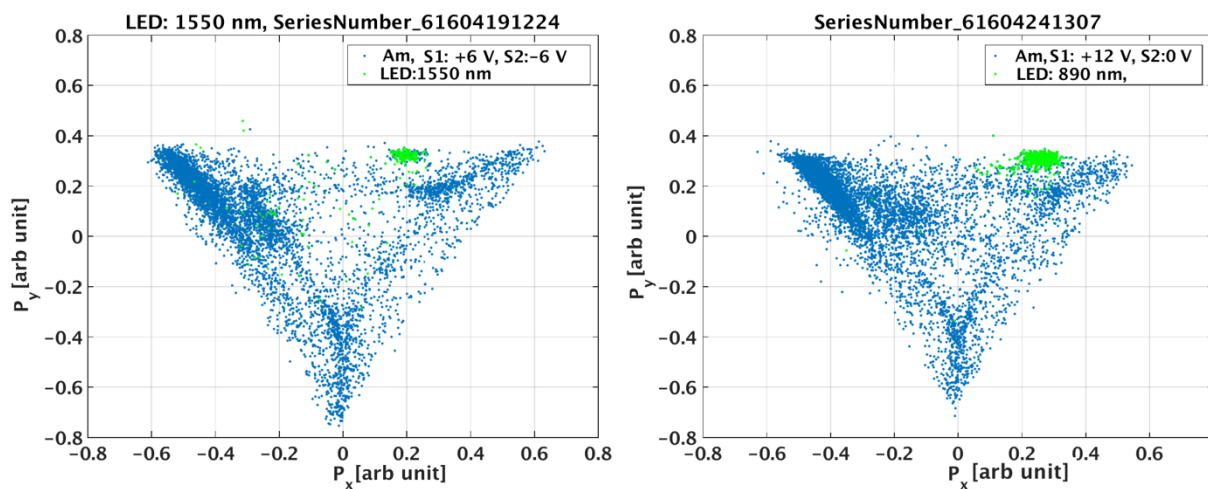


Figure 5.11: A plot showing the phonon partitioning parameter in the x - y plane as defined in equations 5.10 and 5.11. *Left panel:* The 1550 nm LED events are highlighted in green, and they appear to be focused on phonon sensors (B) and (D). *Right panel:* The 890 nm LED events are highlighted in green.

5.3.1 Stability of charge channels

The average time required to take a single data set, which includes 10 K events is between (5-10) minutes, ruled by the event rate of the data acquisition system at QTF. So, to confirm the stability of each charge channels during this time, we looked at the charge vs. event number as shown in figure 5.12. In these plots, we can clearly notice that the charge collected on both charge channels seems to be stable, and there was no degradation in the 60 keV line.

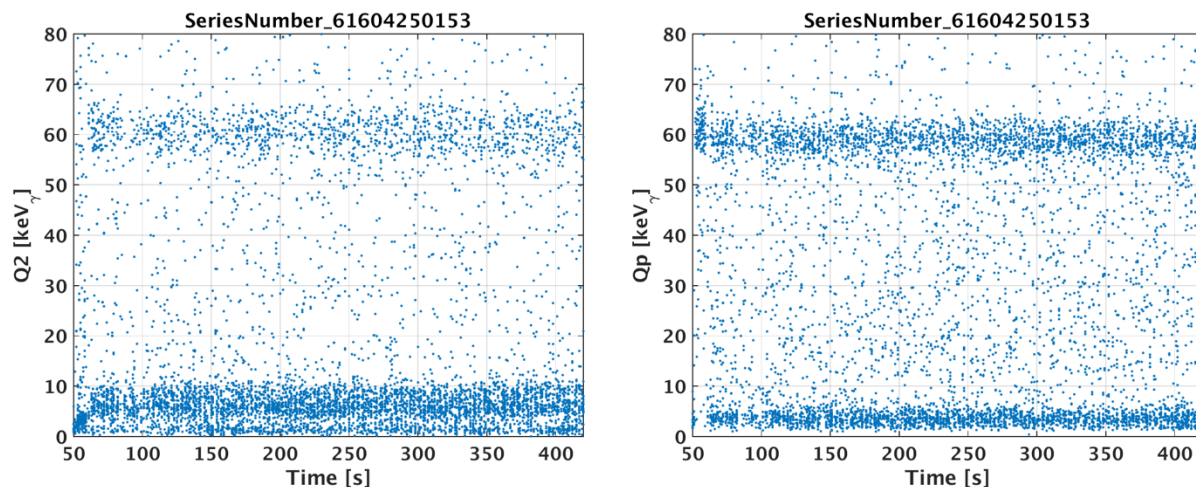


Figure 5.12: The plot shows the charge calibrated to a gamma source for the electrodes Q_2 and Q_p . Data was taken for ~ 7 min and bias voltage of 24 V. Electrons were collected at side 1 (Q_p) while holes were collected at side 2 (Q_2). No charge degradation was noticed for the gamma events, indicating a stable charge collection efficiency over the time.

5.3.2 Relative calibration of phonon channels

Relative calibration is a method used to calibrate the four phonon sensors relative to each other in order to estimate the recoil energy. This is done by considering the tail of each phonon pulse (since the tail does not depend on position), then matching all tails with each other. This method provides accurate relative calibration coefficients and sets the tails of all phonon sensors

at the top of each other. The information about the tail of the pulse can be extracted from the late integral quantities (derived quantities from the Reduced Quantities).

By evaluating at the late integral quantities, and plotting the desired channels, the slope of the linear fit (as shown in figure 5.13) for the data represents the calibration factor between the two corresponding channels.

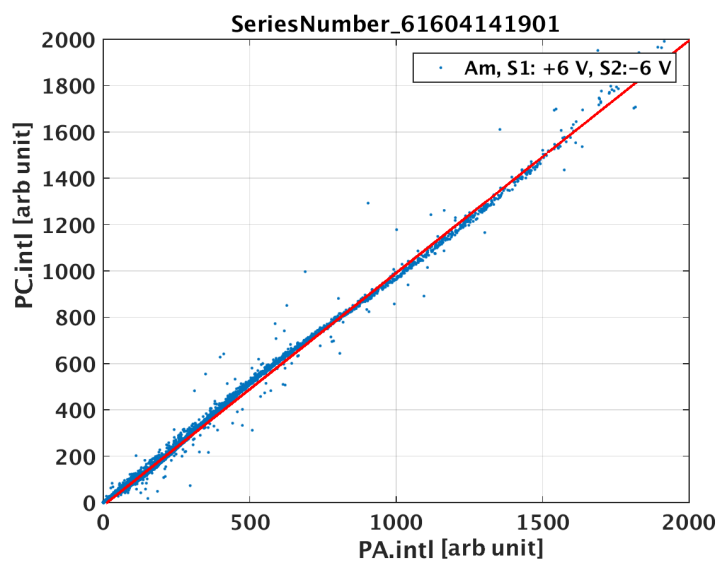


Figure 5.13: The late integral quantities of phonon channel C vs. phonon channel A.

Similar procedure should be repeated for all phonon channels. Once relative calibration is accomplished, the calibrated pulse tails can be checked whether they are aligned at the top of each or not as shown in figure 5.14.

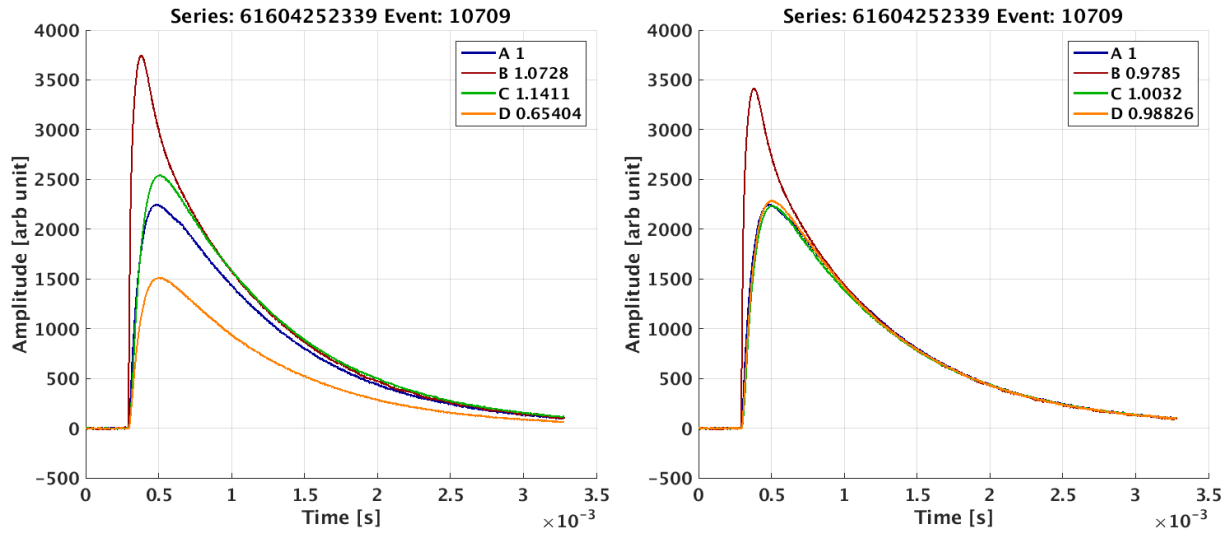


Figure 5.14: *Left panel*: Phonon pulses before applying relative calibration to the phonon channels. *Right panel*: Phonon pulses after evaluating the late integral quantities, and using the calibration factors to plot the pulses.

5.4 Processing method and data quality cuts

There are different processing algorithms within the SuperCDMS experiment, such as the optimal filter (OF), non-stationary optimal filter (NSOF) and the most updated version, the two-template optimal filter (2TOF). Each one of the processing algorithms can produce a number of physical parameters required to interpret the data. The optimal filter is considered the oldest among all and works best in the case of fixed pulse shape. The NSOF is able to give a better energy resolution, while the position resolution is worse. And the latest (2TOF) was developed after introducing the iZIP detector, where two templates are generated; a slow template which is generated from the average of pulses, while the second is a fast template and is generated from the average of the residuals. In processing the data of this chapter, only optimal filter algorithm was used.

Data quality cuts are used to eliminate unauthentic events that might happen while taking data. Some of the data quality cuts are generated within the SuperCDMS collaboration and can be used at different test facilities, while some other cuts are customized to work for a certain detector.

5.4.1 Optimal Filter

The optimal filter algorithm is used to reconstruct phonon pulses by fitting the individual phonon trace to a known pulse shape template. The template is generated by taking the average of a large number of good pulses. In the case of charge pulse reconstruction, the algorithm uses the fact that the shape of the charge pulse does not change, because the charge pulse shape

depends on the electronics, which are invariant for different data sets. In the time domain, the observed signal has the following form:

$$S(t) = a \cdot A(t) + n(t) \quad (5.4)$$

where a is the amplitude that will be estimated, $A(t)$ is the known template, $n(t)$ is the noise. The estimation of a can be directly found as the maximum value of the signal trace. However, this tends to be a poor estimation, as it ignores the pulse shape and noise contribution. So, another way to estimate a in the time-domain can be performed by χ^2 minimization. But it also turned out as improper maximum-likelihood estimator [72].

So, the best estimation for the amplitude was achieved in the frequency domain, using the Fast Fourier Transformation (FFT) for the trace, the noise, and template. The variation in noise with frequency can be dealt with in optimal filter algorithm by considering the noise spectrum as a set of error bars for the corresponding frequencies. This process will eventually result in having the signal to noise ratio governing the weight of the individual frequency components regardless of the noise peaks.

Once the raw data is processed using the optimal filter algorithm, a list of Reduced Quantities (RQs) is generated, then, those quantities are used in analyzing the data. Below, I am listing some derived quantities, that will show up in the analysis of this chapter.

- $P(X)$ represents the amplitude of the phonon pulse in phonon channel (X).
- Q_x is the charge calibrated optimal filter quantity with no crosstalk.
- P_{sum} is the sum of the calibrated phonon channels, which is equivalent to

$$P_{\text{sum}} = P_A \cdot \text{cf}(1) + P_B \cdot \text{cf}(2) + P_C \cdot \text{cf}(3) + P_D \cdot \text{cf}(4); \quad (5.5)$$

where cf is the relative calibration factor for each phonon channel.

- $P(X)_{\text{std}}$ is the standard deviation for phonon channel X .
- $P(X)_{\text{int}}$ is the late integral quantity of phonon channel X .
- P_x is the x-coordinate component for the phonon partitioning parameter at the detector's surface and defined as

$$P_x = \cos(2 \cdot \pi / 12) \cdot (P_B \cdot \text{cf}(2) - P_D \cdot \text{cf}(4)) / P_{\text{sum}}; \quad (5.6)$$

- P_y is the y-coordinate component for the phonon partitioning parameter at the detector's surface and defined as

$$P_y = (\sin(2 \cdot \pi / 12) \cdot (P_B \cdot \text{cf}(2) + P_D \cdot \text{cf}(4)) - P_C \cdot \text{cf}(3)) / P_{\text{sum}}; \quad (5.7)$$

5.4.2 The charge χ^2 cut

The charge χ^2 cut is considered a very useful tool at the early stages of data analysis due to its ability to reject events based on the pulse shape. The charge χ^2 cut excludes any event above a quadratic function of the uncalibrated charge energy, where lower energy events experience a stricter cut due to the poor energy estimation for lower energies, as shown in figure 5.15. Therefore, the manually adjusted curve can be calibrated by viewing the events in the energy - χ^2 parameter space, in order to tune the cut parameters.

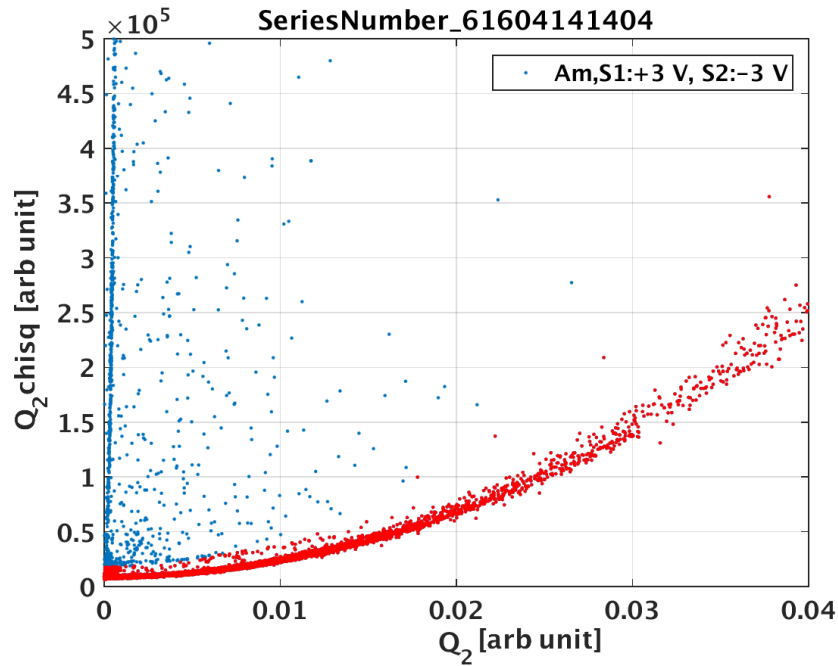


Figure 5.15: The optimal filter charge χ^2 for Q_2 versus Q_2 .

The figure above depicts events with abnormally high χ^2 value in blue, and located above the χ^2 curve. Those events were excluded from the analysis. The cut allows greater χ^2 value for greater energies because the energy estimation improves as the energy increases. An example of a charge pulse passing the charge χ^2 cut and another pulse failing the cut is shown in figure 5.16.

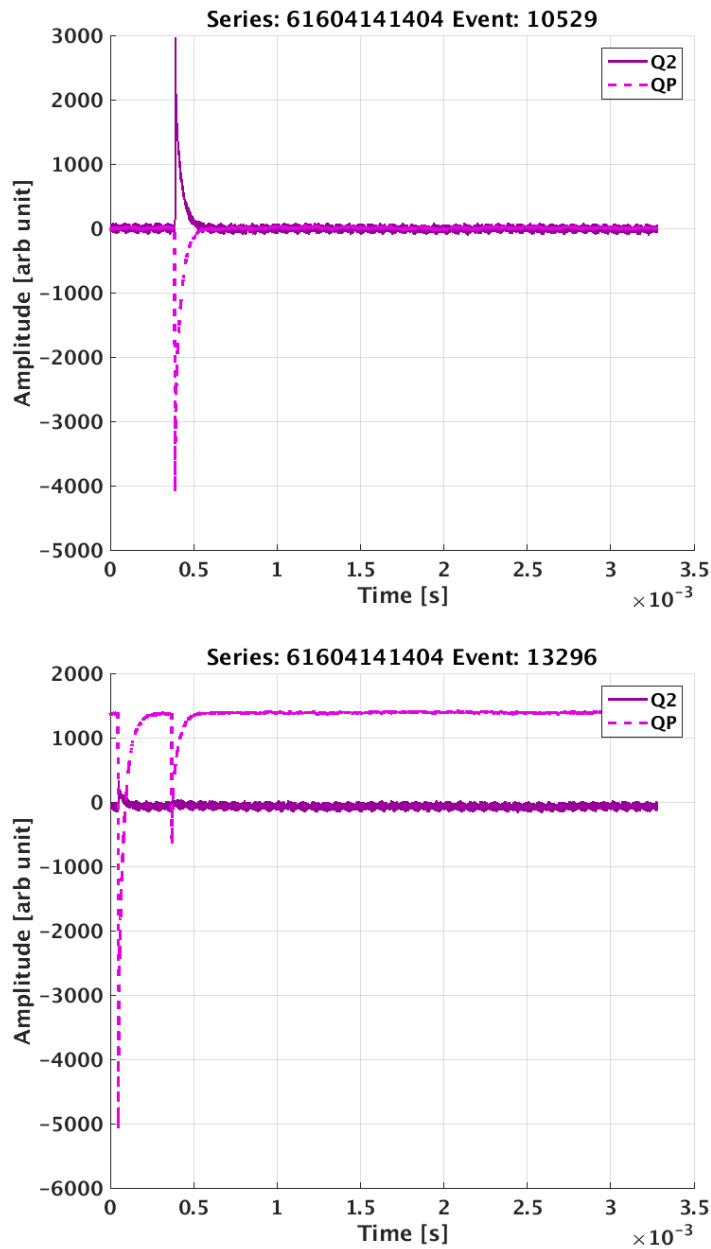


Figure 5.16: *Top panel:* An example for a good charge pulse, which survived after applying the charge χ_2 cut. *Bottom panel:* This plot shows an example for one of the excluded events by the charge χ_2 cut.

5.4.2 Phonon pile-up cut

A pile-up event is a description of an event or more not well separated in time. So, more than one event can be seen at the same trace window in the form of pulse overlapping. Those events have to be removed since the optimal filter pulse template cannot handle a mixture of two pulses.

Although the charge χ^2 cut removes $\sim 95\%$ of pile-up events, a more refined and tunable cut is required in order to improve the analysis output [73]. The pile-up cut works initially by taking the OF algorithm quantity for each phonon channel, then iterate that twice in order to seek for events crossing a threshold value. The threshold is a (user defined value) tunable parameter that needs to be re-adjusted if the calibration of the phonon channel changes. The second tunable parameter is the number of time bins needed to determine the maximum of the phonon trace.

This test is performed for each individual event, so an event passes the cut, only if the threshold was not crossed more than once in any of the four phonon channels. However, if the threshold has been crossed more than once, then a further checkpoint makes sure that the crossing occurred within a certain time binning in order to pass or fail a particular event.

An example of two pulses, one passing the pile-up and another one failing the cut is depicted in figure 5.17.

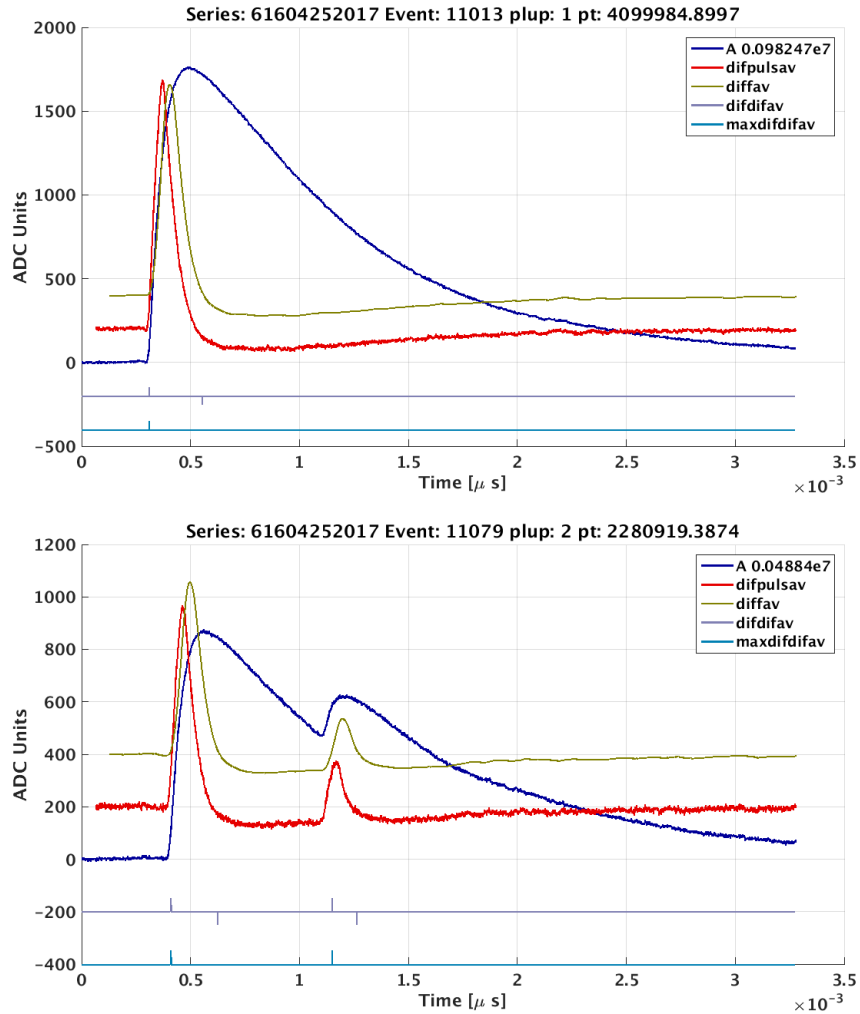


Figure 5.17: *Top panel:* This plot shows an event passing the pile-up cut, because the threshold was crossed only one time (“maxdifdifav” represents a counter for the number of times the threshold value is crossed). *Bottom panel:* This plot shows a rejected pile-up event, where the threshold value was crossed twice.

5.4.3 Phonon duplicates cut

The duplicates cut aims to eliminate any repeated event within a range of events. It compares the pulse maximum of each phonon trace for a particular event, with the maximum of the

following eight events. Once there is a match, within some uncertainty, then one of the two events will be removed.

5.4.4 Phonon pre-pulse cut

The phonon pre-pulse cut aims to eliminate the set of events having a phonon noise that is inconsistent with the series phonon noise. Once events having high noise been cut from the pre-pulse region, a better elimination of noise events can be achieved.

By considering only random events, the cut can be tuned by plotting the standard deviation phonon quantities. The standard deviation quantity will ideally have a Gaussian distribution, and good events are located close to its mean. However, the bad events are expected to be $\sim 3\sigma$ or further. Hence, a 3σ cut is expected to eliminate a good portion of bad events may be left over after applying the χ^2 cut.

5.5 Data analysis and results

During our measurement, a set of parameters were varied, such as the electric field configuration (iZIP / straight), the LED wavelength, the electrode bias voltage and the electrode polarity. On the other hand, the LED energy was invariant in any data set. Moreover, the flashing time (number of emitted photons), was also invariant. I have categorized the analysis of this section into four main segments and added one part to demonstrate the possibility of deploying the detector's internal LED (940 nm) in the IR calibration measurement.

However, the internal LED test was limited to the characterization of the charge pulse shape and the effect of bias voltage on phonon signal amplification. Knowing that the ^{241}Am was used as gamma calibration source during this measurement, then Table 4 can be constructed based on the bias voltages at each corresponding side (S1/ S2).

Table 4: The measured and expected values for the charge and total phonon energy using a calibration gamma source ^{241}Am . In the table, each of the measured value represents either the measured charge signal (Q) or the total phonon energy (Psum) based surface and bulk events. The error in the measured values is based on the deviation from the measured average value.

^{241}Am	Bias [V]	Measured				Expected {full Q}		Expected{meas.Q}	
		Q [± 0.2 keV _y]		Psum [± 5 keV _t]		Psum [± 5 keV _t]		Psum [± 5 keV _t]	
		Bulk	Surface	Bulk	Surface	Bulk	Surface	Bulk	Surface
Side	0	--	--	60		60		60	
S1	3	54.7	2.0	155	120	180	120	169	117
S2	-3	53.5	55.3						
S1	6	58.7	2.0	240	170	300	180	295	177
S2	-6	54.3	56.6						
S1	9	59.0	2.0	435	240	420	240	414	236
S2	-9	54.8	56.6						
S1	12	59.2	2.0	530	300	540	300	534	294
S2	-12	54.5	56.6						
S1	-6	57.5	2.4	320	230	300	180	290	182
S2	6	54.6	58.4						
S1	-12	60.0	2.4	550	330	540	300	540	310
S2	12	60.0	60.0						

And the details below illustrate the method used in calculating some of the data in the above table. In the second row, for bias voltage $+3 V$ on side 1 (Q_p) and $-3 V$ on side 2 (Q_2), for bulk events the bias voltage will be $6 V$, while for surface events the bias voltage is $3 V$. Recalling that the radiation spectrum of Am source has a peak at $60 keV$, and the energy required to create one e^- / h^+ in germanium crystal is $\epsilon_\gamma \approx 3 eV$, at our operating temperature.

If a bias voltage of $V_b = 6 V$ is applied across the detector, then the total energy of phonon signal indicated by {expected full Q} in the above table, will be equal to the energy of the primary recoil E_r added to the amplified Neganov-Luke phonons (assuming all charges drift all the way to the respective electrode): $E_t = E_r + eV_b N_Q$ [74], noting that electron recoil is calibrated with full charge collection gives $E_Q = E_r$ then,

$$\text{For **bulk** events: } E_t = E_r \times \left(1 + \frac{eV_b}{\epsilon_\gamma} \right)$$

$$E_t = E_r \times \left(1 + \frac{6eV}{3eV} \right)$$

$$E_t = 60 keV \times (3) = 180 keV_t$$

$$\text{For **surface** events: } E_t = E_r \times \left(1 + \frac{eV_b}{\epsilon_\gamma} \right)$$

$$E_t = E_r \times \left(1 + \frac{3eV}{3eV} \right)$$

$$E_t = 60 keV \times (2) = 120 keV_t$$

now for the expected {measured Q} in the last two columns, the calculation is based on the measured Q value, so the expected energy of phonon channels based on the measured charge is

as the following: *for bulk events:* $E_t = E_r + E_{luke} = E_r + E_Q \frac{eV}{\epsilon}$

$$= 60 + 54.7 \times 2 = 169.4 \text{ keV}_t$$

$$\text{and for surface events: } E_t = E_r + (E_{Q1} + E_{Q2}) \times \frac{eV}{\varepsilon}$$

$$= 60 + (2.0 + 55.3) \times \left(\frac{3eV}{3eV} \right) = 117.3 \text{ keV}_t$$

The same procedure can be applied to each bias voltage in Table 4.

5.5.1 1550 nm LED in iZIP e-field configuration

The 1550 nm LED (emitting photons with energy 0.8 eV, in-between the direct and indirect band gaps of germanium at 45 mK) was operated in continuous pulse mode, at constant current of 0.05 μ A, flashing time of 20 μ s and 16 Hz frequency. Those values remained invariant throughout the test. Using the ^{241}Am radioactive source, the energy scale was calibrated for both phonon sensors and charge electrodes. Knowing that the mean free path λ for gamma photons is long enough to reach the bulk of our germanium crystal (1-inch-thick) at our operating temperature, we were able to relatively compare the depth of IR photons inside the crystal.

What we will be looking to achieve at the end of this analysis, is to compare the amplification of the IR photons to that of gamma source, indicate the location where interactions took place in the crystal and finally compare that to the theoretically expected values.

The way the bias voltage was applied to the electrodes is similar to the iZIP configuration, for example: +24 V means that a bias voltage of +12 V and -12 V were applied to Q_p and Q_2 respectively. From figure 5.18, we can notice that the charge collected at Q_2 increases as the voltage increase. But there was no indication that we might reach up to 100 % collection

efficiency. Moreover, the charge collected at Q_2 is always greater than that collected at Q_p regardless of the collected charge type, electrons or holes.

A noticeable charge degradation occurs at both electrodes as shown in figure 5.18. In these data sets, the LED was turned on after several minutes from the start of the run, and there was no

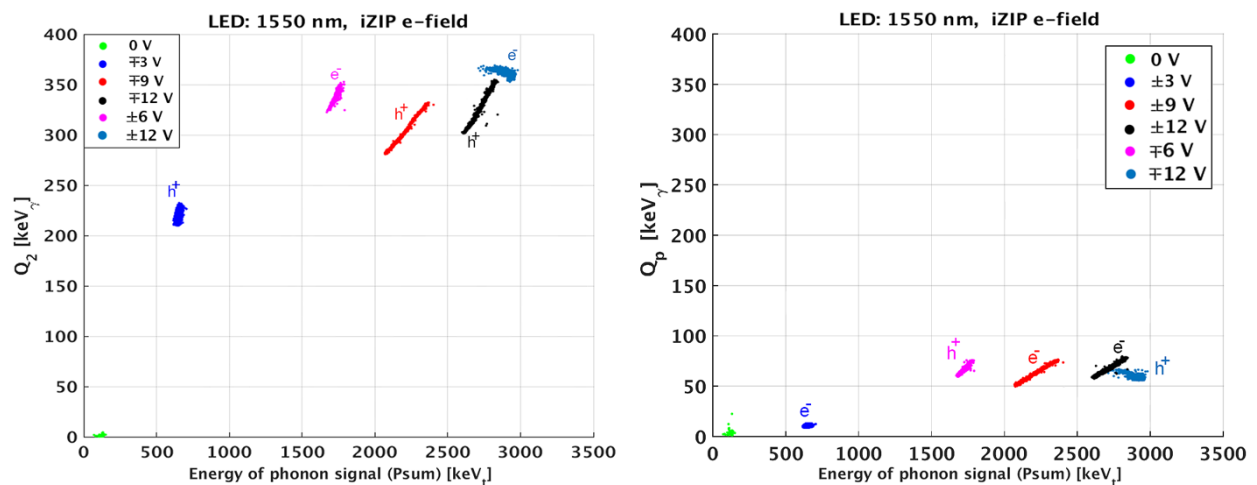


Figure 5.18: *Left panel*: Q_2 charge channel calibrated to gamma source vs. the sum of the calibrated phonon channels. *Right panel*: Q_p charge channel vs. the sum of calibrated phonon channels.

evidence that the LED parameters have changed during the test. So, the charge degradation might be related in this case to charge carriers being recombined or trapped in the crystal.

In figure 5.18, the label next to each colored group of events indicates whether electrons or holes are collected at the corresponding charge electrode. The reference in the polarity is always with respect to Q_p , so a +6 V would mean that Q_p is positively biased with respect to Q_2 by 6 V.

Now I will describe the basis on which the calculations are done for the 1550 nm LED in iZIP field. At zero bias voltage, the energy of phonon channels was calibrated to that from the

gamma source as shown earlier in figure 5.9. So, we concluded that the IR photons deposit 127 keV at zero voltage (which is indicated in the first row of the table).

Table 5: The measured and expected energy values for the 1550 nm LED in the iZIP electric field configuration. In the 7th column, B stands for bulk events and S for surface events. The ± 6 V data set is not available.

LED: 1550 nm	Bias [V]	Measured		Expected			
		Q [± 0.2 keV _y]	Psum [± 5 keV _t]	Q [± 5 keV _y]	Σ Q [± 5 keV _y]	Psum [± 5 keV _t]	
				0 V	meas.P	exp. Q	meas. Q
Side	0	--	127	--		127	
S1	3	10.5	635	476	508	B: 1080	365
S2	-3	227.0				S: 603	
S1	6	N.A	N.A		--	--	--
S2	-6	N.A			--	--	--
S1	9	73.0	2340		738	B:2985	1351
S2	-9	335.0				S: 1556	
S1	12	69.0	2830		676	B: 3937	1763
S2	-12	340.0				S: 2032	
S1	-6	67.0	1750		812	B: 2032	957
S2	6	348.0				S: 1080	
S1	-12	59.0	2900	693	B: 3937	1863	
S2	12	375.0			S: 2032		

Based on the energy from phonon channels, the expected measurement for the charge can be found as:

$$Q = \frac{127 \text{ keV}}{0.8 \text{ eV}} \times 3 = 476 \text{ keV}_y, \text{ calibrated to gamma source}$$

Once a bias voltage is applied, for example ± 3 V, then the expected charge measurement based on the measured phonon signal will be:

$$E_t(\text{at } \pm 3 \text{ V}) = E_r(\text{at } 0 \text{ V}) + E_Q \left(\frac{eV_b}{\varepsilon} \right)$$

$$635 = 127 + E_Q \left(\frac{3}{3} \right)$$

$$E_Q = 508 \text{ keV}_\gamma \text{ (assuming all events are surface events)}$$

Now if we double the bias voltage $\mp 6 \text{ V}$, we expect the amplification to increase as well, so:

$$E_t(\text{at } \pm 6 \text{ V}) = E_r(\text{at } 0 \text{ V}) + \sum Q \left(\frac{6}{3} \right)$$

$$\sum Q = \left(\frac{1750 - 127}{2} \right) = 812 \text{ keV}_\gamma$$

The last column in the table, gives the expected total energy based on the measured Q value, this would be equal to:

$$E_t = E_r(\text{at } 0 \text{ V}) + \sum Q \left(\frac{eV_b}{\varepsilon} \right)$$

$$E_t = 127 + (E_{Q1} + E_{Q2}) \left(\frac{3}{3} \right)$$

$$E_t = 127 + (227 + 10.5) = 365 \text{ keV}_t$$

Once again, if we double the voltage, we expect the amplification to be doubled. So, for the case of bias voltage 6 V :

$$E_t = 127 + (348 + 67) \times \frac{6}{3} = 957 \text{ keV}_t$$

For the bulk and surface events value, they were calculated as the following:

$$\text{for } \mathbf{bulk} \text{ events } E_t = 127 \times \left(1 + \frac{eV_b}{0.8} \right) = 127(8.5) = 1080 \text{ keV}_t$$

$$\text{for } \mathbf{surface} \text{ events } E_t = 127 \times \left(1 + \frac{eV_b}{0.8} \right) = 127(8.5) = 603 \text{ keV}_t$$

5.5.2 1550 nm LED in flat e-field configuration

The LED settings used in this part are identical to the LED settings in iZIP e-field configuration. This time the charge channel Q_2 was grounded, and the bias voltage was only at Q_p . So, depending on what polarity Q_p has, either electrons or holes will be collected at side 1 of the detector. We can notice that on average, the charge collected at Q_p is greater than that collected at Q_2 . Similar to the iZIP e-field scenario, the charge degradation is present in both bias polarities. From figure 5.19, we can notice that the data labeled -3 V at Q_p seems to have different LED settings, because the phonon signal appears high compared to the other data sets ($+3\text{ V}$, $+6\text{ V}$ and -6 V).

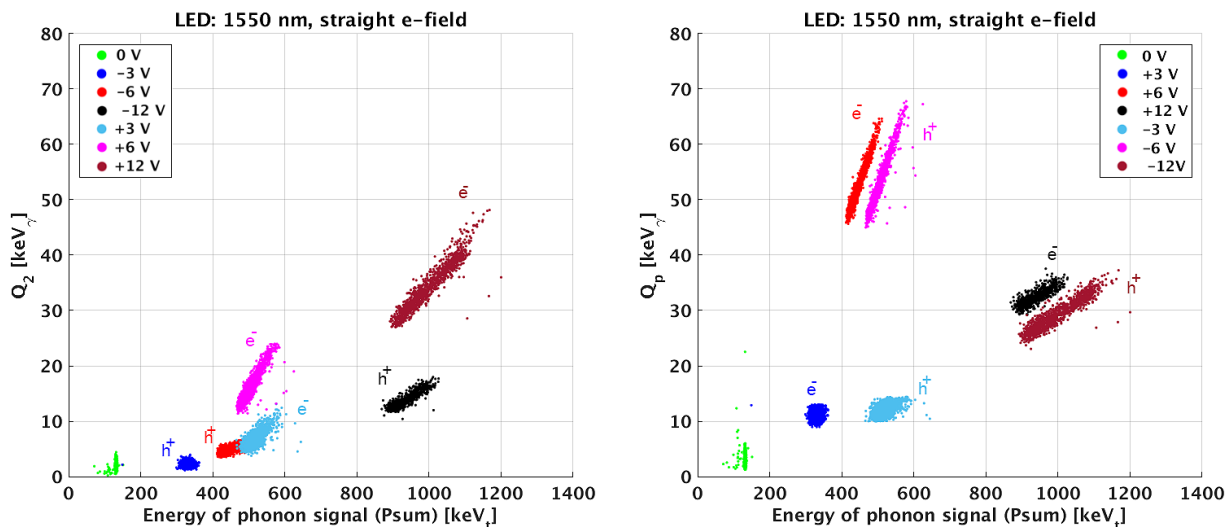


Figure 5.19: *Left panel*: Charge channel Q_2 calibrated to a gamma source vs. the sum of calibrated phonon channels. *Right panel*: Charge channel Q_p calibrated to a gamma source vs. the the sum of calibrated phonon channels.

Table 6: The measured and expected energy values for the 1550 nm LED in a straight electric field configuration.

LED: 1550 nm	Bias [V]	Measured		Expected			
		Q [± 0.2 keV _{γ}]	Psum [± 5 keV _t]	Q [± 5 keV _{γ}]	Σ Q [± 5 keV _{γ}]	Psum [± 5 keV _t]	
				0 V	meas.P	exp. Q	meas. Q
Side	0	--	127	--		127	
S1	3	12	330	476	203	603	143
S2	0	4.1					
S1	6	62	490		182	1080	261
S2	0	5					
S1	12	34	950		206	2032	327
S2	0	16					
S1	-3	12.1	500		373	603	149
S2	0	9.5					
S1	-6	64	580		227	1080	301
S2	0	23					
S1	-12	33	1070		236	2032	346
S2	0	40					

The details of the calculations done to conclude the expected values in Table 6 are in Appendix 1.A. In this test, side 2 was grounded and the bias voltage was on Q_p located on side 1 of the detector.

5.5.3 890 nm LED in iZIP e-field configuration

The 890 nm LED (emitting photons with energy ~ 1.4 eV, greater than the direct band gap of germanium at 45 mK) was operated in continuous pulse mode, at constant current of 0.05 μ A, flashing time 20 μ s and 14.3 Hz frequency. The penetration depth of the 890 nm photons is less than the surface field region (which is of order of couple millimeters – as shown in figure 5.8). The induced charge on Q_2 has a clear trend of increasing Luke amplification with voltage. Although the trend is not linear, it is monotonous. Moreover, very few charges were able to drift to the charge electrodes before they recombine or get trapped in the crystal. This

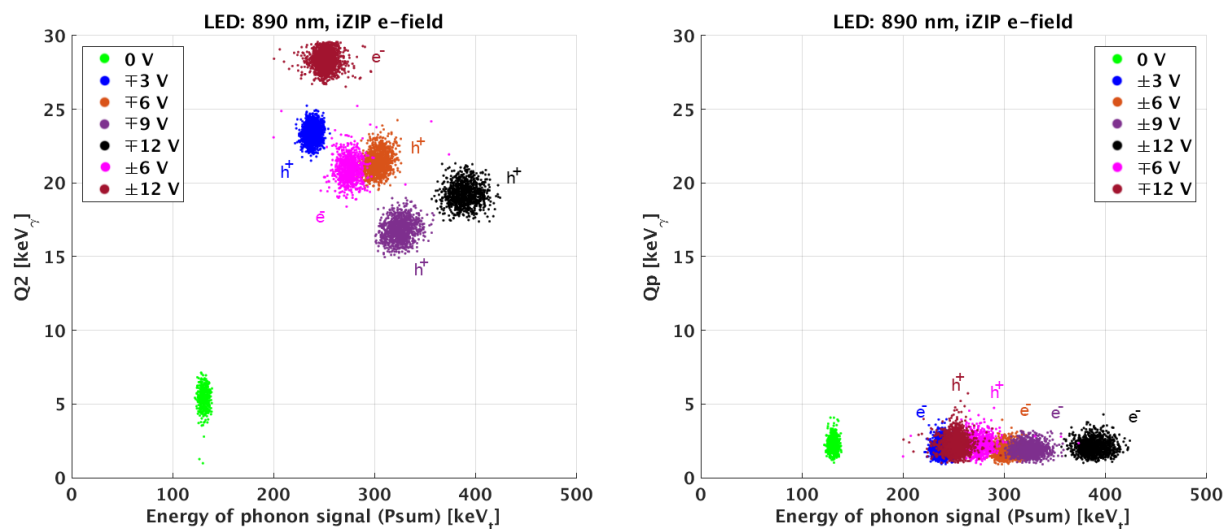


Figure 5.20: *Left panel*: Charge channel Q_2 calibrated to a gamma source vs. the sum of calibrated phonon channels. *Right panel*: Charge channel Q_p calibrated to a gamma source vs. the sum of calibrated phonon channels.

measurement was restricted to measure the number of charges, the phonons energy, and to collect more observations to set a reference point for future study of IR photons at milli-Kelvin temperature in germanium crystal.

In positive bias voltage tests, it was noticed that the phonon amplification increases as the voltage increase, ideally, if we have a 100% charge collection efficiency, then the charge signal should not change as the voltage does. However, since that is not the case, it was expected that the charge collection efficiency improves at higher bias voltages. The expectations were valid for positive polarity, and the contrary occurs in the case of negative polarity (where electrons are collected on Q₂) shown in the left panel of figure 5.19.

A summary of the measurements done for the 890 nm LED is listed in Table 7. The calculations are similar to that for the 1550 nm, except that the LED energy value in this case is 1.4 eV.

Table 7: The measured and the expected values for the 890 nm LED in the iZIP electric field configuration. In the 7th column, B stands for bulk events, and S stands for surface events.

LED: 890 nm	Bias [V]	Measured		Expected			
		Q [± 0.2 keV _y]	Psum [± 5 keV _t]	Q [± 5 keV _y]	Σ Q [± 5 keV _y]	Psum [± 5 keV _t]	
				0 V	meas.P	exp. Q	meas. Q
Side	0	--	125	--		125	
S1	3	1.8	230	268	105	B: 661	151
S2	-3	24.0				S:393	
S1	6	1.8	295		85	B: 1196	173
S2	-6	22.0				S: 661	
S1	9	1.9	315		63	B: 1732	182
S2	-9	17.0				S: 929	
S1	12	2.0	375		63	B: 2268	211
S2	-12	19.5				S: 1196	
S1	-6	2.1	270		73	B: 1196	172
S2	6	21.5				S: 661	
S1	-12	2.2	235	28	B: 2268	251	
S2	12	29.3			S: 1196		

5.5.4 890 nm LED in flat e-field configuration

In the case of flat electric field, the LED settings were similar to that for iZIP field. First of all, the zero-voltage data set indicated that we have more energy deposited in the phonon channels, compared to some of the biased data sets (as shown in figure 5.21). Moreover, the negative bias voltage gives higher phonon signal than positive voltage; electrons drifting through the crystal to the other electrode (Q_p) are more likely to be trapped, so produce less Luke phonons, which is consistent with the natural charge carrier behavior in germanium, at the milli-Kelvin temperature range [75].

If the photon beam is relatively concentrated and hits close to a phonon channel, most charges go to the phonon channel on side 2 of the detector Q_2 . While on the far side, Q_p , they have spread out, either by diffusion or due to the oblique propagation, which might explain the

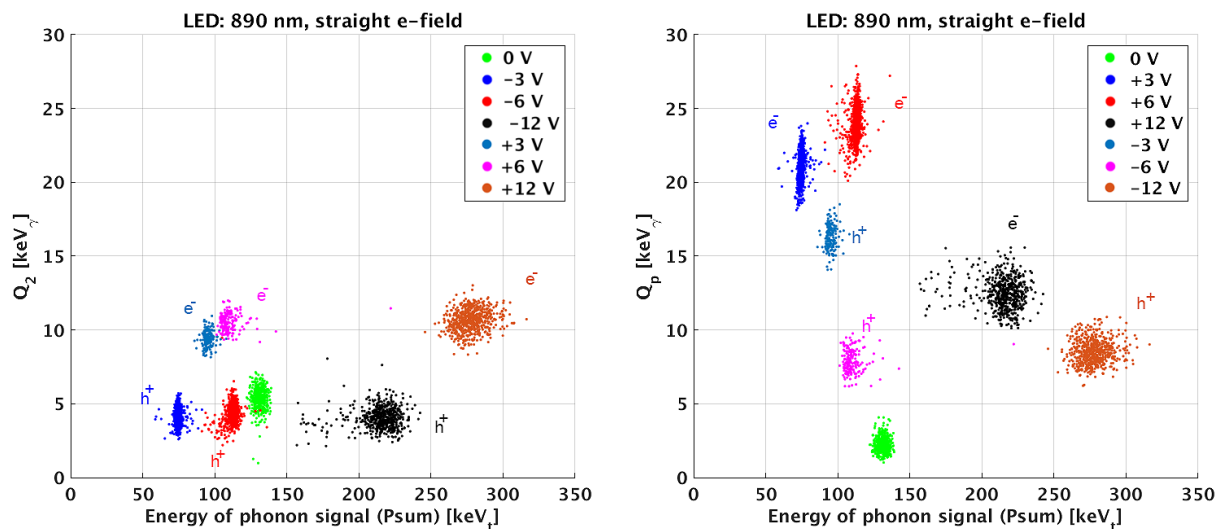


Figure 5.21: *Left panel*: Charge channel Q_2 calibrated to a gamma source vs. the sum of calibrated phonon channels. *Right panel*: Charge channel Q_p calibrated to a gamma source vs. the sum of calibrated phonon channels.

higher signal on side Q_p compared to that on side Q_2 .

If we compare the number of collected charge carriers on Q_p , as shown in figure 5.21, to that from figure 5.19, we may conclude that the number of charges able to drift to Q_p (on the other side of the detector) in the case of iZIP configuration is very small. That is because the generated e^-/h^+ pairs are collected or recombined at the surface (side 2 of the detector). On the other hand, for the flat field configuration, while Q_2 is grounded, charges collected on side 2 have no contribution to the measured charge signal. Then e^-/h^+ are forced to drift across the crystal and reach Q_p , as shown in figure 5.21.

The spread in signal for the electrons on Q_p side seems to come from a time-dependence, but rather than decreasing, the signal increases at the very beginning over short period – as shown in figure 5.22. This is very likely because charges accumulate and Q_{inner} , Q_{outer} electrodes saturate quickly due to the small capacitance, so the signal moves over to Q_p which has a larger capacitance.

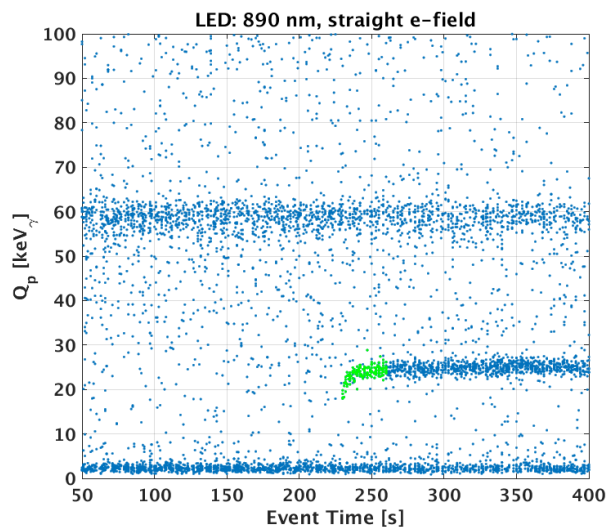


Figure 5.22: The increase in charge signal indicates the quick saturation of Q_{inner} and Q_{outer} on side 1.

5.5.5 940 nm detector's internal LED

This test was performed using the detector's internal LED, in order to see if it is conceivable to get similar results and to have an amplified phonon signal without placing any heat load to the fridge. If this works, it will also give a chance for the internal LED to be used in future SuperCDMS detectors instead of installing external LEDs for testing and calibration purposes.

The wavelength of the LED used is 940 nm (1.32 eV), and it was operated at 0.16 μA , flashing time 20 μs and 14.3 Hz frequency. In this test, we were able to identify the LED pulses, and to confirm that we can have a phonon amplification when the detector is biased as shown in figure 5.23.

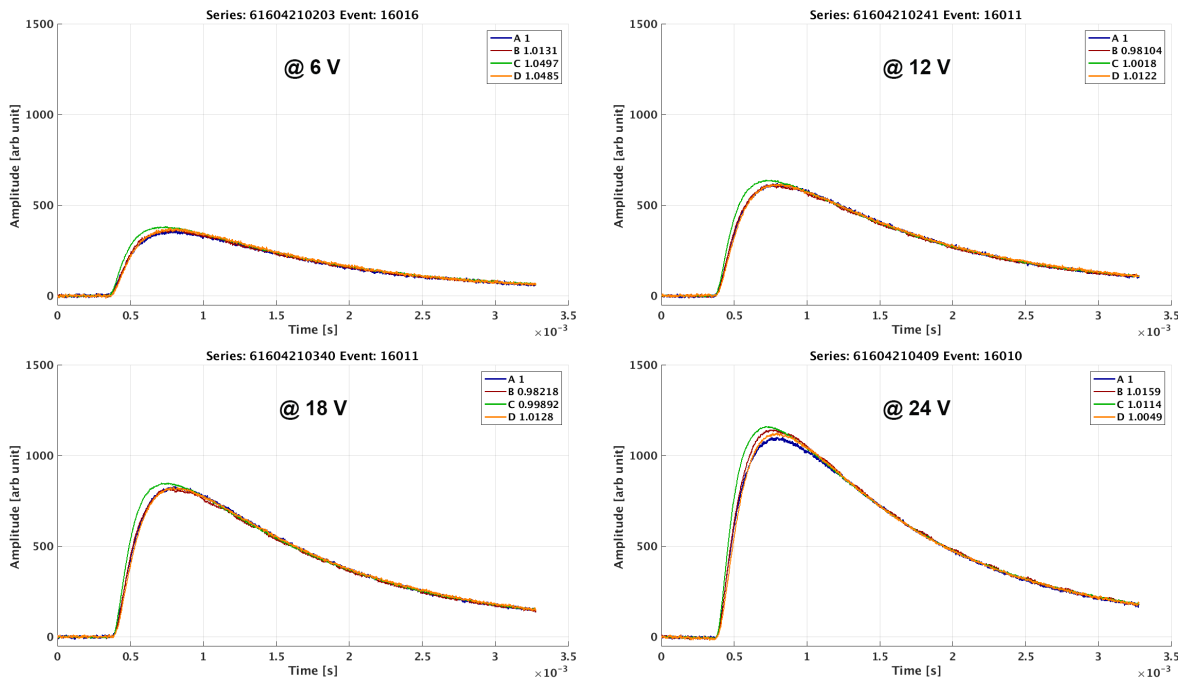


Figure 5.23: Calibrated phonon pulses, from the detector's internal LED. The amplification in the phonon channels occurs as the voltage increase, which confirms the formation or Neganov-Luke phonons.

From figure 5.23 we can conclude that the pulse shape is similar to that from a gamma source (figure 5.14). Hence, the optimal filter fitting algorithm can be used to study the LED pulses. More importantly, it is confirmed that it is possible to produce IR photons from the internal LED

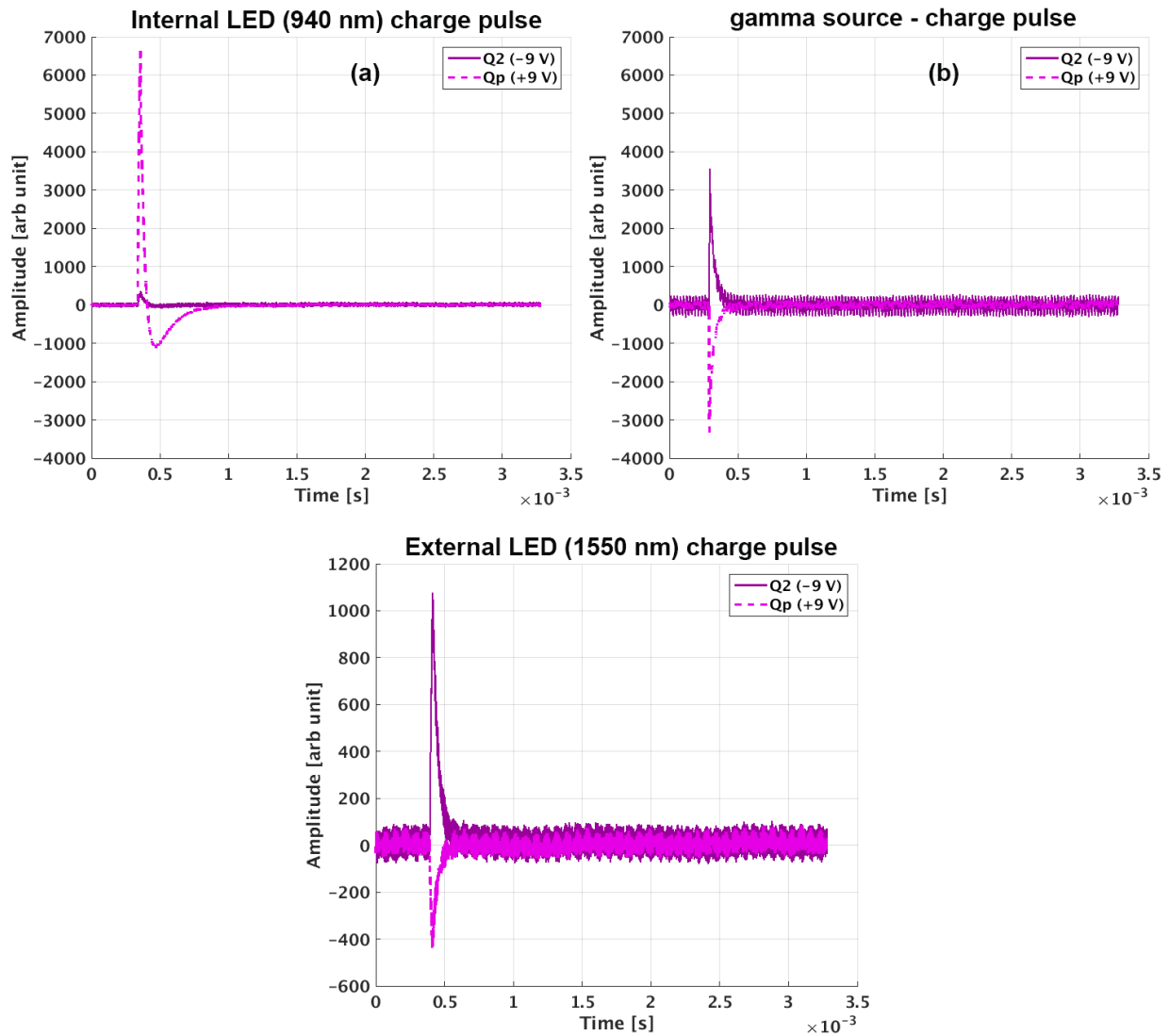


Figure 5.24: Charge pulses for different events. Unusual behavior for the charge channels in figure (a) while operating the detector’s internal LED, compared to regular pulse shape from the gamma source in figure (b) and an external LED in figure (c).

without heating the detector, so that the internal LEDs may be used for further study. On the other hand, the shape of the charge pulse for the internal LED was different than that resulting from gammas or pulses from the external LEDs, as depicted in figure 5.24. Ideally, the charge signal should be invariant, because it depends only on the charge readout electronics.

The different shape of charge pulses indicates that the signal observed from the internal LEDs is not exclusively from the photon interaction in the detector but impacted by electronic interference. The reason for that is most likely a connection between LED circuit and charge amplifier circuit in the readout electronics, which was acceptable in the original design since the LEDs were not meant to be operated while taking data. Further studies are required to determine the possibility of using the LEDs of new detectors for calibrating their energy scale [76].

5.6 Summary of findings

Based on the measurement settings for the LEDs, the behavior of IR photons differs than gamma photons in germanium crystal at the temperature range of this study (~ 45 mK). Once we examine the charge collection over time, we can confirm the charge degradation over time occurs only for the IR photons. As a result of the drop in charge signal, the phonon signal drops as well.

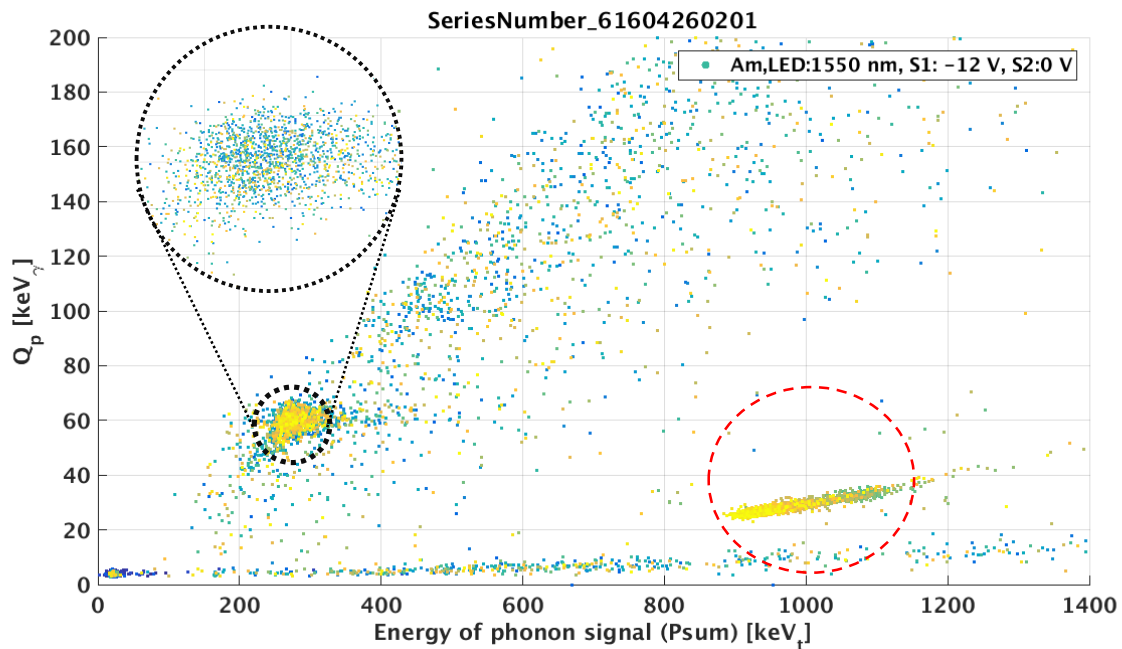


Figure 5.25: The events circled in red are the 1550 nm LED events. A clear charge degradation accompanied with a drop in the phonon signal was recorded at different voltages and polarities. While the ^{241}Am events, zoomed area and circled in black, show homogenous distribution in time and no evidence of charge/ phonon degradation.

Since this behavior can be reversed, and the full charge/ phonon gain can be retrieved once the detector is flashed, it is highly possible that the charge degradation is due to charge trapping within the detector or charge recombination. From figure 5.26, we can notice that the signal resulting from drifting electrons across the detector seems to be increasing with voltage, which also indicates for less electron trapping at higher voltages.

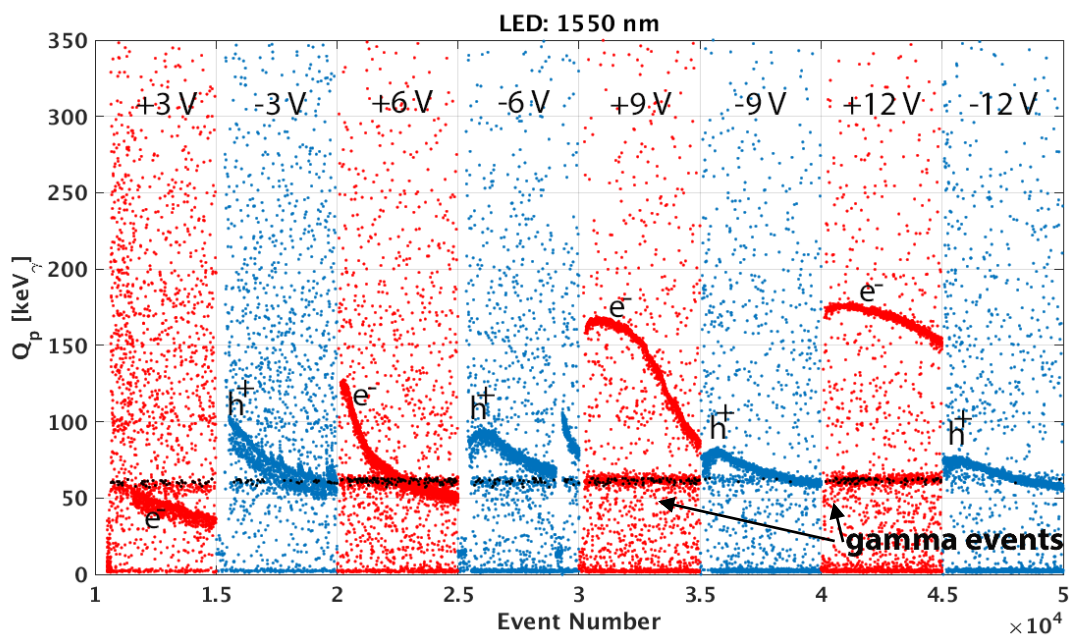


Figure 5.26: The detector is biased at different voltages and different polarities as indicated in the plot. Each colored slice contains a stable gamma event line at 60 keV and a dropping signal from the IR photons. The initial state of the detector can be retrieved by flipping the polarity, which confirms that the drop in the charge/ phonon signal can be referred to the detector rather than the LED itself.

Figure 5.27 depicts the change in energy in the phonon signal at different bias voltages and electric field configurations. If we assume that the amplification of IR photons will be linear with voltage, similar to that for gamma photons.

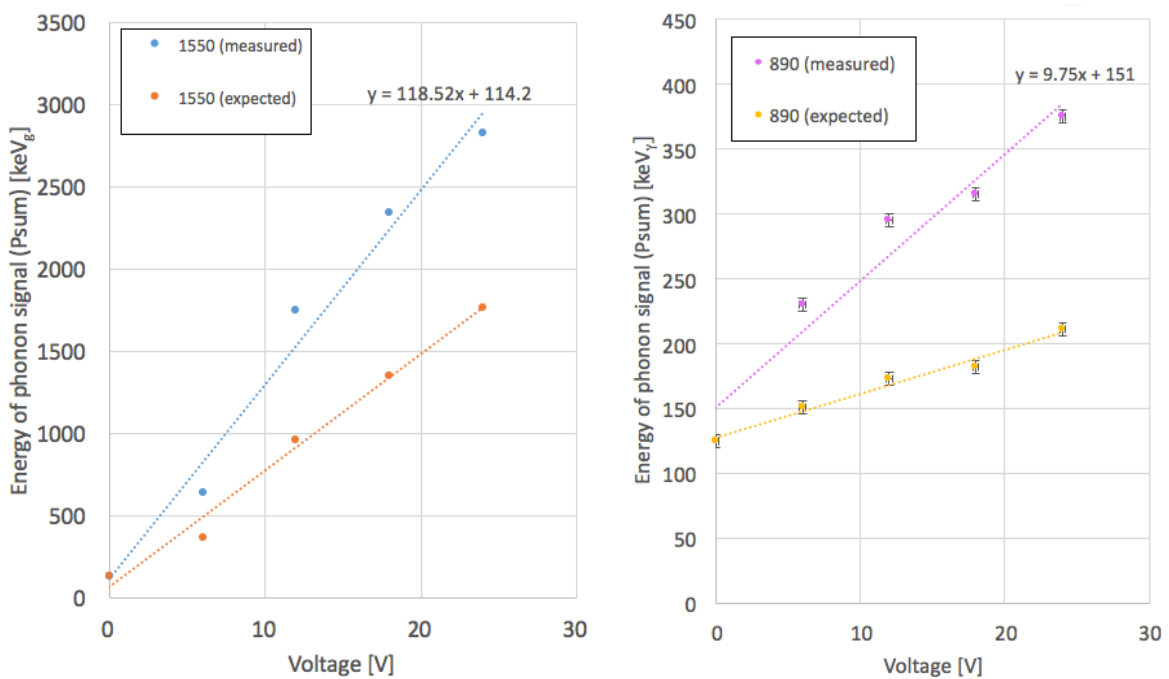


Figure 5.27: The energy of the phonon signal at different bias voltages for the 1550 nm (890 nm) LED, in iZIP electric field configuration. The green (yellow) line is the expected phonon signal for the IR photons based on measured charge, while the blue (purple) line is the measured phonon signal. Error bars are too small to be seen.

The data in green shows the expected energy for the phonon signal based on the measured charge from both charge electrodes. In regards of IR photons, the measured Luke amplification exceeds the expected phonon signal based on the collected charges. Since the optical fiber is

shining on the phonon channels side of the detector, this might be an indication that the IR photons might be absorbed by the aluminum fins at the surface, which may result in increasing the phonon signal [77].

Now we show that the total collected charges at both charge electrodes are less than what one might be expecting, based on the measured energy from the phonon signal.

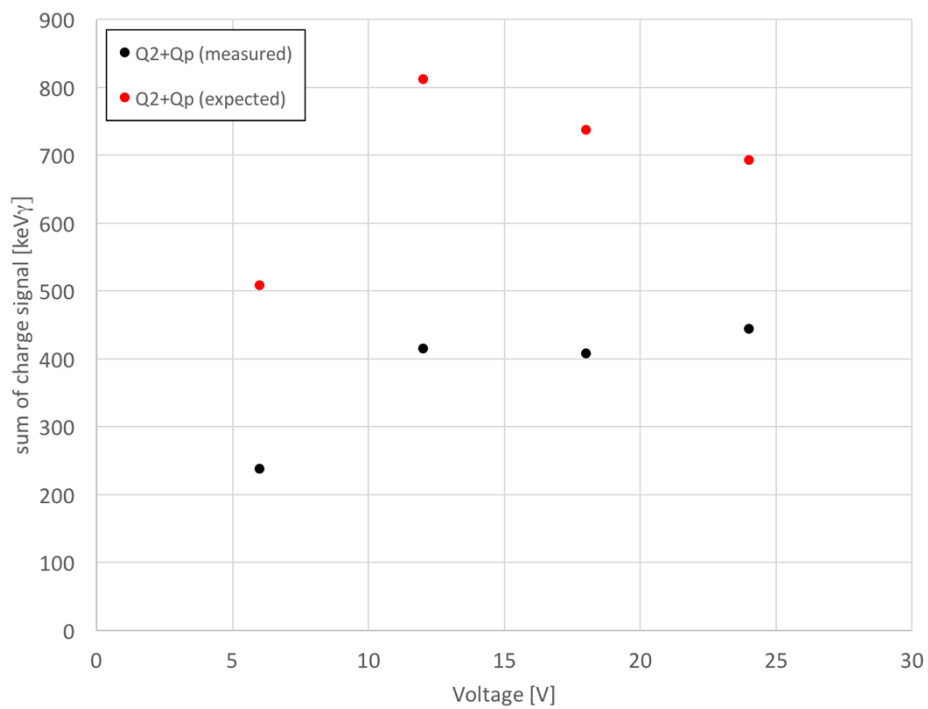


Figure 5.28: Charge collection efficiency variation with bias voltage. The measured (in black) and expected (in red) charge signal, in iZIP electric field configuration for the 1550 nm LED at different voltages. The expected charge signal in this case is based on the measured phonon signal from IR events.

From Table 5, we can use the value for photons' energy at 0 V is $E_0 = 127 \text{ keV}$ to estimate the number of photons striking the surface of the detector LED in iZIP field configuration.

$$n_p = \frac{E_0}{E_{\text{photon}}} \quad (5.8)$$

where n_p is the number of photons, E_{photon} is photon energy for the corresponding LED and equals to 0.8 eV in this case. So, the expected number of photons is

$$n_p = \frac{127 \text{ keV}}{0.8 \text{ eV}} \approx 159 \times 10^3 \text{ photon}$$

Then, the number of electron-hole pairs (n_c) can be expressed as

$$n_c = \frac{\Delta E}{e\Delta V} \quad (5.9)$$

using the slope (118.5×10^3) of the measured signal from figure 5.27, we can estimate the number of created e^-/h^+ pairs:

$$n_c = \frac{\Delta E}{e\Delta V} = 118.5 \times 10^3 \text{ } e^-/h^+ \text{ pairs}$$

so, the ionization efficiency (ξ) can be expressed as

$$\xi \equiv \frac{n_c}{n_p} \quad (5.10)$$

which is equal to

$$\xi = \frac{118.5 \times 10^3}{159 \times 10^3} = 74.5\%$$

Since the Al fins cover about 4% of the detector's surface [78], then it was expected to have relatively high ionization efficiently. Even though, having $\sim 75\%$ as a rough estimation, we can conclude that about the majority of the photons can penetrate the surface and create e^-/h^+ pairs in the case of the 1550 nm photons.

On the other hand, for the 890 nm we have the slope $\Delta E/eV = 9.75 \times 10^3$, and from Table 7, we can find $E_0 = 125 \text{ keV}$ can be found from figure 5.27. Knowing that the $E_{\text{photon}} = 1.4 \text{ eV}$, we get

$$\xi = \frac{9.75 \times 10^3}{125 \times 10^3} = 7.8\%$$

indicating that very few photons are able to penetrate the surface of the crystal and create e^-/h^+ pairs in the case of 890 nm photons.

Chapter 6

Conclusion and outlook

The SuperCDMS experiment has concluded its last run towards the end of the year 2015, and CDMSlite run II has reported official results during the first quarter of 2016 setting a new exclusion limit in the search for low-mass WIMPs, for a total exposure of 70 kg day [53]. Figure 2.10 reflected the published results from CDMSlite run II in addition to other WIMP-search experiments. It also depicted the SuperCDMS SNOLAB projected sensitivity for germanium and silicon detectors in both normal, and high voltage modes. The new experiment at SNOLAB is expected to have improved sensitivity to low-mass WIMPs by at least one order of magnitude ($0.3 - 10 \text{ GeV}/c^2$).

In order to be able to detect low-mass WIMPs, an improvement is required to the detector's threshold energy and more studies for detectors at high bias voltage are necessary to increase the gain in signal-to-noise ratio. The high voltage studies at QTF have introduced the possibility of fridge environment as a parameter to affect the high voltage limit. That is supported by the G16K detector, which was rejected for SUL due to low breakdown voltage. However, we were able to apply $+120 \text{ V}$ and -84 V before the detector breaks down and that is much higher than the high voltage mode operated at SUL.

Understanding the physics behind the charge collection, and charge trapping in cryogenic detectors is crucial to explain the different charge behavior trends at different bias voltages and polarities. During the last several years, the University of California, Berkeley made a significant progress in this regard and they have simulated and demonstrated the difference between electron and hole propagation in germanium crystals at the low temperature and low electric field.

The infrared photons calibration measurement at QTF involves a considerable understanding of the charge propagation in germanium crystals at such low temperatures. In terms of the 1550 nm photons, we noticed about 20% of the photons make it through the surface layer and we have estimated the ionization efficiency to $\sim 75\%$. Knowing that bulk events start to occur after 2 mm from the surface (figure 5.6), we can estimate the penetration depth of the photons to be between (2-5) mm. If we compare this value to the penetration depth from literature as in [79], we find our rough estimation is highly reasonable. We noticed also that the 1550 nm photon signal decreases as a result of detector effects rather than the LED itself which keeps the door open for further calibration using external LEDs.

In regards to the 890 nm photons, further studies are necessary to better understand the behavior of these photons in germanium crystal at low temperatures.

Bibliography

- [1] M. S. Turner, “Dark Matter, Dark Energy and Fundamental Physics,” p. 15, Dec. 1999.
- [2] F. Zwicky, “Republication of: The redshift of extragalactic nebulae,” *Gen. Relativ. Gravit.*, vol. 41, no. 1, pp. 207–224, 2009.
- [3] B. Sadoulet, “Deciphering the nature of dark matter,” *Rev. Mod. Phys.*, vol. 71, no. 2, pp. S197–S204, Mar. 1999.
- [4] “The MOSFIRE Deep Evolution Field Survey.” [Online]. Available: <http://mosdef.astro.berkeley.edu/for-the-public/public/galaxy-masses/>. [Accessed: 01-Oct-2016].
- [5] K. Freese, “Review of Observational Evidence for Dark Matter in the Universe and in upcoming searches for Dark Stars,” *EAS Publ. Ser.*, vol. 36, pp. 113–126, May 2009.
- [6] R. H. Sanders, *The Dark Matter Problem*. 2010.
- [7] P. Simon and P. Schneider, “Weak-lensing shear estimates with general adaptive moments, and studies of bias by pixellation, PSF distortions, and noise,” p. 20, Sep. 2016.
- [8] J. Renn, T. Sauer, and J. Stachel, “The Origin of Gravitational Lensing: A Postscript to Einstein’s 1936 Science Paper,” vol. 275, no. 5297, p. 184 LP-186, Jan. 1997.
- [9] J.-P. Kneib and P. Natarajan, “Cluster lenses,” *Astron. Astrophys. Rev.*, vol. 19, no. 1, p. 47, 2011.
- [10] D. Clowe *et al.*, “A Direct Empirical Proof of the Existence of Dark Matter,” *Astrophys. J.*, vol. 648, no. 2, pp. L109–L113, Sep. 2006.
- [11] D. Clowe, S. W. Randall, and M. Markevitch, “Catching a bullet: direct evidence for the existence of dark matter,” *Nucl. Phys. B - Proc. Suppl.*, vol. 173, pp. 28–31, Nov. 2007.
- [12] T. Sepp *et al.*, “Simulations of Galaxy Cluster Collisions with a Dark Plasma Component,” p. 12, Mar. 2016.
- [13] D. Clowe, A. Gonzalez, and M. Markevitch, “Weak-Lensing Mass Reconstruction of the Interacting Cluster 1E 0657–558: Direct Evidence for the Existence of Dark Matter,” *Astrophys. J.*, vol. 604, no. 2, pp. 596–603, Apr. 2004.

- [14] CDMS Collaboration *et al.*, “Search for annual modulation in low-energy CDMS-II data,” p. 5, Mar. 2012.
- [15] Z. Ahmed *et al.*, “Combined limits on WIMPs from the CDMS and EDELWEISS experiments,” *Phys. Rev. D*, vol. 84, no. 1, p. 11102, Jul. 2011.
- [16] A. Bottino, F. Donato, N. Fornengo, and S. Scopel, “Supersymmetric dark matter,” *Nucl. Phys. B - Proc. Suppl.*, vol. 113, no. 1–3, pp. 50–59, Dec. 2002.
- [17] L. J. Rosenberg, “Dark-matter QCD-axion searches,” *Proc. Natl. Acad. Sci.*, vol. 112, no. 40, pp. 12278–12281, Oct. 2015.
- [18] R. D. Peccei and H. R. Quinn, “CP Conservation in the Presence of Pseudoparticles,” *Phys. Rev. Lett.*, vol. 38, no. 25, pp. 1440–1443, Jun. 1977.
- [19] J. E. Kim, “Light pseudoscalars, particle physics and cosmology,” *Phys. Rep.*, vol. 150, no. 1–2, pp. 1–177, 1987.
- [20] I. P. Stern, “Axion dark matter searches,” 2014, pp. 456–461.
- [21] J. E. Kim, “Weak-Interaction Singlet and Strong CP Invariance,” *Phys. Rev. Lett.*, vol. 43, no. 2, pp. 103–107, Jul. 1979.
- [22] M. Dine, W. Fischler, and M. Srednicki, “A simple solution to the strong CP problem with a harmless axion,” *Phys. Lett. B*, vol. 104, no. 3, pp. 199–202, 1981.
- [23] C. Redino, “Modified Supersymmetric Dark Sectors,” p. 96, Jun. 2015.
- [24] S. Y. Hoh, J. R. Komaragiri, and W. A. T. Wan Abdullah, “Dark matter searches at the large hadron collider,” 2016, p. 20005.
- [25] W. Rau, “Dark matter search experiments,” *Phys. Part. Nucl.*, vol. 42, no. 4, pp. 650–660, Jul. 2011.
- [26] G. Jungman, M. Kamionkowski, and K. Griest, “Supersymmetric dark matter,” *Phys. Rep.*, vol. 267, no. 5–6, pp. 195–373, 1996.
- [27] L. Wang and D.-M. Mei, “A Comprehensive Study of Low-Energy Response for Xenon-Based Dark Matter Experiments,” p. 33, Apr. 2016.
- [28] A. M. Galper *et al.*, “Design and performance of the GAMMA-400 gamma-ray telescope for dark matter searches,” 2013, pp. 288–292.
- [29] A. M. Galper *et al.*, “Status of the GAMMA-400 project,” *Adv. Sp. Res.*, vol. 51, no. 2, pp. 297–300, Jan. 2013.
- [30] D. S. Akerib *et al.*, “Preliminary limits on the WIMP-nucleon cross section from the

- cryogenic dark matter search (CDMS),” *Nucl. Phys. B - Proc. Suppl.*, vol. 70, no. 1–3, pp. 64–68, Jan. 1999.
- [31] D. Abrams *et al.*, “Exclusion limits on the WIMP-nucleon cross section from the Cryogenic Dark Matter Search,” *Phys. Rev. D*, vol. 66, no. 12, p. 122003, Dec. 2002.
- [32] R. Abusaidi *et al.*, “Exclusion Limits on the WIMP-Nucleon Cross Section from the Cryogenic Dark Matter Search,” *Phys. Rev. Lett.*, vol. 84, no. 25, pp. 5699–5703, Jun. 2000.
- [33] The CDMS Collaboration and Z. Ahmed, “Dark Matter Search Results from the CDMS II Experiment,” *Science (80-.)*, vol. 327, no. 5973, pp. 1619–1621, Feb. 2010.
- [34] P. Cushman, “The SuperCDMS Collaboration Meeting at the University of Minnesota,” 2016. .
- [35] W. Rau, “Queen’s Internal Web Page,” 2014. [Online]. Available: http://cdms.phy.queensu.ca/cdms_restricted/Cryostat/Tech/Fridge_Geometry/Fridge_Geometry.html.
- [36] “CRYOMECH.” [Online]. Available: http://www.cryomech.com/specificationsheet/PT407_CP2800RM_ss.pdf.
- [37] F. Pobell, *Matter and methods at low temperatures*, 3rd, . Berlin ; New York : Springer, c2007., 1937.
- [38] J. Pradhan, N. K. Das, and A. Chakraborty, “Thermo-dynamical process simulation of dilution refrigerator,” *Cryogenics (Guildf)*, vol. 57, pp. 158–165, 2013.
- [39] M. C. Fritts, “Background Characterization and Discrimination in the Final Analysis of the CDMS II Phase of the Cryogenic Dark Matter Search,” University of Minnesota, 2011.
- [40] “CDMS Cold Hardware,” 2002. [Online]. Available: http://cdms.berkeley.edu/cdms_restricted/coldhardware/html/coldhardware.html.
- [41] S. Al Kenany *et al.*, “SuperCDMS Cold Hardware Design,” *J. Low Temp. Phys.*, vol. 167, no. 5, pp. 1167–1172, 2012.
- [42] B. Serfass, “CDMS wiki,” 2008. [Online]. Available: http://cdms.berkeley.edu/wiki/doku.php?id=detectors:led_info.
- [43] R. Agnese *et al.*, “Demonstration of surface electron rejection with interleaved germanium detectors for dark matter searches,” *Appl. Phys. Lett.*, vol. 103, no. 16, p. 164105, May 2013.

- [44] A. Anderson, "Phonon-Based Position Determination in SuperCDMS iZIP Detectors," *J. Low Temp. Phys.*, vol. 176, no. 5–6, pp. 959–965, Jan. 2014.
- [45] L. Hsu, "Low Energy Nuclear Recoil Ionization Yield and SuperCDMS Dark Sectors Workshop 2016 SuperCDMS SNOLAB Projects," 2016. [Online]. Available: https://indico.cern.ch/event/507783/contributions/2151856/attachments/1266351/1874762/darksectors_calibration.pdf.
- [46] W.-Z. Wei, L. Wang, and D.-M. Mei, "Temperature Dependence of the Average Energy Expended Per e-h Pair for Germanium-Based Dark Matter Experiments," p. 6, Feb. 2016.
- [47] C. Kittel, *Introduction to Solid State Physics*, 8th Editio. 2004.
- [48] R. Bunker, "Low-threshold Results from the Cryogenic Dark Matter Search Experiment," 2011.
- [49] B. S. Group, "Super Cryogenic Dark Matter Search." [Online]. Available: <http://cdms.berkeley.edu/experiment.html>.
- [50] S. W. Nam and B. Cabrera, "Transition-edge sensor with enhanced electrothermal feedback for cryogenic particle detection." Google Patents, 2001.
- [51] D. S. Akerib *et al.*, "Design and performance of a modular low-radioactivity readout system for cryogenic detectors in the CDMS experiment," *Nucl. Instruments Methods Phys. Res. Sect. A Accel. Spectrometers, Detect. Assoc. Equip.*, vol. 591, no. 3, pp. 476–489, 2008.
- [52] D. Hooper and L. Goodenough, "Dark matter annihilation in the Galactic Center as seen by the Fermi Gamma Ray Space Telescope," *Phys. Lett. Sect. B Nucl. Elem. Part. High-Energy Phys.*, vol. 697, no. 5, pp. 412–428, 2011.
- [53] R. Agnese *et al.*, "New Results from the Search for Low-Mass Weakly Interacting Massive Particles with the CDMS Low Ionization Threshold Experiment," *Phys. Rev. Lett.*, vol. 116, no. 7, p. 71301, Feb. 2016.
- [54] R. Agnese *et al.*, "Projected Sensitivity of the SuperCDMS SNOLAB experiment," Sep. 2016.
- [55] M. GmbH, "Magnicon - Physical research and instrumentation," 2016. [Online]. Available: <http://www.magnicon.com/squid-systems/noise-thermometer/>.
- [56] S. H. Lee and S.-G. Lee, "Study on the fabrication of low-pass metal powder filters for use at cryogenic temperatures," *J. Korean Phys. Soc.*, vol. 69, no. 3, pp. 272–276, Aug. 2016.
- [57] "API technologies corp." [Online]. Available: <http://www.mouser.com/ds/2/382/series->

- 700-high-performance-connectors-372078.pdf. [Accessed: 01-Jan-2016].
- [58] M. Fritts, “Recent Results in Detector Testing,” 2016.
- [59] B. Young, T. Saab, B. Cabrera, J. J. Cross, and R. A. Abusaidi, “Tc Tuning of Tungsten Transition Edge Sensors Using Iron Implantation.”
- [60] K. Page, “A modified detector concept for SuperCDMS: The HiZIP and its charge performance,” Queen’s University, 2013.
- [61] W. Rau, K. Page, Carlos, and Chase, “G16K hiZIP measurements,” 2012. [Online]. Available: http://cdms.phy.queensu.ca/cdms_restricted/Cryostat/Runs/Run_034/Run_034.html.
- [62] “G16K - detector break down Voltage,” 2015. [Online]. Available: http://cdms.phy.queensu.ca/cdms_restricted/Cryostat/Runs/Run_059/Run_059.html.
- [63] Y. Hochberg, T. Lin, and K. M. Zurek, “Absorption of light dark matter in semiconductors,” p. 6, Aug. 2016.
- [64] M. Pyle, N. Zobrist, and B. Page, “G23R HV Performance,” 2016.
- [65] B. Cabrera, M. Pyle, R. Moffatt, K. Sundqvist, and B. Sadoulet, “Oblique propagation of electrons in crystals of germanium and silicon at sub-Kelvin temperature in low electric fields,” p. 3, Apr. 2010.
- [66] R. A. Moffatt *et al.*, “Imaging the oblique propagation of electrons in germanium crystals at low temperature and low electric field,” *Appl. Phys. Lett.*, vol. 108, no. 2, p. 22104, Jan. 2016.
- [67] “Ceramoptec,” 2016. [Online]. Available: <http://www.ceramoptec.de/products/fibers/optran-uv-wf.html>.
- [68] S. M. Sze, *Physics of Semiconductor Devices*, 2nd ed. John Wiley & Sons, 1998.
- [69] M. A. Precker, Jürgen W. and da Silva, “Experimental estimation of the band gap in silicon and germanium from the temperature–voltage curve of diode thermometers,” *Am. J. Phys.*, vol. 70, pp. 1150–1153, 2002.
- [70] “Marubeni,” 2016. [Online]. Available: <http://www.tech-led.com/product/smc/>.
- [71] Macfarlane, “Low-level absorption spectrum of high purity Ge at various temperatures.” [Online]. Available: <http://www.ioffe.ru/SVA/NSM/Semicond/Ge/optic.html>.
- [72] J. P. Filippini, “A Search for WIMP Dark Matter Using the First Five-Tower Run of the Cryogenic Dark Matter Search,” University of California, Berkeley, 2002.

- [73] B. Serfass, J. Yen, and M. Pyle, “Charge Pile-up Study on G48 UCB Run 400,” 2011. [Online]. Available: http://titus.stanford.edu/cdms_restricted/detector_physics/iZIP/ebook/101118/Qpileup.html.
- [74] D. S. Akerib *et al.*, “Exclusion limits on the WIMP-nucleon cross section from the first run of the Cryogenic Dark Matter Search in the Soudan Underground Laboratory,” *Phys. Rev. D*, vol. 72, no. 5, p. 52009, Sep. 2005.
- [75] A. T. J. Phipps, “Ionization Collection in Detectors of the Cryogenic Dark Matter Search,” University of California, Berkeley, 2016.
- [76] “LED Info,” 2009. [Online]. Available: http://cdms.berkeley.edu/wiki/doku.php?id=detectors:led_info&s%255B%255D=led&s%255B%255D=chassis.
- [77] N. J. Lambert *et al.*, “Splitting a single Cooper-pair with microwave light,” Apr. 2013.
- [78] N. Kurinsky, P. Brink, R. Partridge, B. Cabrera, and M. Pyle, “SuperCDMS SNOLAB Low-Mass Detectors: Ultra-Sensitive Phonon Calorimeters for a Sub-GeV Dark Matter Search,” p. 4, Nov. 2016.
- [79] J. Domange, A. Broniatowski, E. Olivieri, M. Chapellier, and L. Dumoulin, “Quantum Efficiency for Electron-Hole Pair Generation by Infrared Irradiation in Germanium Cryogenic Detectors,” *AIP Conf. Proc.*, vol. 1185, no. 1, 2009.

Appendices

Appendix A

A.1 Calculations of Neganov-Luke Amplification for 1550 nm, in straight field

The calculations of this section explain the method followed to find some of the numbers in Table 6. Moreover, the Am-241 was used to calibrate the IR photons at 0 V, and it was found the IR photons deposits a total phonon energy equivalent to 127 keV_t . Based on the total phonon energy for the IR photons at 0 V, we start by calculating the expected number of e^- / h^+ pairs created with respect to the calibration of gamma source (column #5):

$$Q = \frac{127 \text{ keV}}{0.8 \text{ eV}} \times 3 = 476 \text{ keV}_\gamma$$

where the IR photons energy $E = \frac{hc}{\lambda} = 0.8 \text{ eV}$, and $\varepsilon_\gamma = 3 \text{ eV}$ for each e^- / h^+ pair.

If there is no charge trapping or recombination, then we should be able to measure 476 keV_γ on each one of the charge channels. However, this is not the case.

Now, to calculate the expected charge signal, based on the measured total phonon energy (column #6):

$$E_t(\text{at } 3 \text{ V}) = E_r(\text{at } 0 \text{ V}) + \sum Q \left(\frac{eV_b}{\varepsilon} \right)$$

$$330 \text{ keV}_t = 127 \text{ keV}_t + \sum Q \left(\frac{3}{3} \right)$$

$$\sum Q = 203 \text{ keV}_\gamma$$

Now, if we apply the same procedure we can also confirm the expected value for (6 V).

$$E_t(\text{at } 6 V) = E_r(\text{at } 0 V) + \sum Q \left(\frac{eV_b}{\varepsilon} \right)$$

$$490 \text{ keV}_t = 127 \text{ keV}_t + \sum Q \left(\frac{6}{3} \right)$$

$$\sum Q = 182 \text{ keV}_t$$

Recalling that this electric field configuration involves one biased surface while the other surface of the detector is grounded. So, we will only be having bulk Neganov-Luke phonon amplification (no surface event amplification).

Next, we will be calculating the expected total phonon energy based on the expected charge signal. That is the value in column # 7:

$$E_t = E(0 V) + E \left(\frac{eV_b}{\varepsilon} \right)$$

$$E_t = 127 \text{ keV}_t + 127 \text{ keV}_t \left(\frac{3}{0.8} \right)$$

$$E_t = 603 \text{ keV}_t$$

and if we double the voltage, then we expect to measure 1080 keV_t . Now, for the last value in column # 8, which represents the expected total phonon energy based on the measured charge value:

$$E_t(\text{at } 3 V) = E_r(\text{at } 0 V) + \sum Q \left(\frac{eV_b}{\varepsilon} \right)$$

$$E_t = 127 \text{ keV}_t + (12 + 4.1) \left(\frac{3}{3} \right)$$

$$E_t = 143 \text{ keV}_t$$